

High-areal-capacity Na-ion battery electrode with uncompromised energy and power densities by simultaneous electrospinning-spraying fabrication

Dr Mengzheng Ouyang ^{1, 11, 12, *}, Dr Zhenyu Guo ^{2, 11}, Dr Luis E Salinas-Farran ¹, Dr Yan Zhao ³, Dr Siyu Zhao ^{4, 5}, Kaitian Zheng ^{2, 6}, Dr Hao Zhang ^{5, 7}, Dr Mengnan Wang ², Dr Guangdong Li ^{1, 8}, Feiran Li ¹, Prof. Xinhua Liu ⁹, Prof. Shichun Yang ⁹, Prof. Fei Xie ¹⁰, Prof. Paul R. Shearing ⁵, Prof. Maria-Magdalena Titirici ², Prof. Nigel P. Brandon ¹

1. Department of Earth Science and Engineering, Imperial College London, London, UK
2. Department of Chemical Engineering, Imperial College London, London, UK
3. Department of School of Energy and Engineering, Jiangsu University, Zhenjiang, China
4. Department of Chemical Engineering, University College London, London, UK
5. Department of Engineering Science, University of Oxford, Oxford, UK
6. School of Chemical Engineering and Technology, Tianjin University, Tianjin, China
7. Department of Chemical Engineering, Massachusetts Institute of Technology, Cambridge, MA, USA
8. School of Chemistry and Chemical Engineering, Beijing Institute of Technology, Beijing, China
9. School of Transportation Science and Engineering, Beihang University, Beijing, China
10. Institute of Physics, Chinese Academy of Science, Beijing, China

¹¹ These authors contributed equally

¹² Lead contact

* Correspondence: mo113@ic.ac.uk M.O.

Summary

Sodium-ion batteries (SIBs) are cost-effective alternatives to lithium-ion batteries (LIBs), but their low energy density remains a challenge. Current electrode designs fail to simultaneously achieve high areal loading, high active content, and superior performance. In response, this work introduces an ideal electrode structure, featuring a continuous conductive network with active particles securely trapped in the absence of binder, fabricated using a universal technique that combines electrospinning and electro-spraying (co-ESP). We found that the particle size must be larger than the network's pores for optimised performance, an aspect overlooked in previous research. The free-standing co-ESP Na₂V₃(PO₄)₃ (NVP) cathodes demonstrated state-of-the-art 296 mg cm⁻² areal loading with 97.5 wt.% active content, as well

as remarkable rate-performance and cycling stability. Co-ESP full cells showed uncompromised energy and power densities ($231.6 \text{ Wh kg}^{-1}/7152.6 \text{ W kg}^{-1}$), leading among reported SIBs with industry-relevant areal loadings. The structural merit is analysed using multi-scale X-ray computed tomography, providing valuable design insights. Finally, the superior performance is validated in the pouch cells, highlighting the electrode's scalability and potential for commercial application.

Keywords

Sodium-ion batteries, cathode, electrode design, electrospinning, electrospraying, pouch cell, high areal loading, high rate performance, X-ray computed tomography.

Introduction

Sodium-ion batteries (SIBs) have emerged as a cost-efficient and sustainable alternative of lithium-ion batteries (LIBs)¹. However, their application is significantly hindered by the lower energy density of existing cathode materials². $\text{Na}_2\text{V}_3(\text{PO}_4)_3$ (NVP) is recognised as one of the most promising cathode candidates due to its high working voltage, high Na^+ conductivity and superior cycling stability³. Yet, it suffers from low electron conductivity and a limited theoretical capacity of 117 mAh g^{-1} . Additionally, most reported SIBs have areal loadings far below industrial demands, with high-areal-loading SIB electrodes typically around 10 mg cm^{-2} ⁴⁻⁶ and a maximum of 60 mg cm^{-2} ⁷, compared to up to 170 mg cm^{-2} for LIBs^{8,9}. This discrepancy is due to the underdeveloped state of cathode materials and structures, further widening the energy density gap between SIBs and LIBs.

There are three effective strategies to enhance an electrode's energy density^{10,11}: (i) applying high active materials areal loading, (ii) eliminating the current collector, and (iii) increasing the active materials content (weight ratio of active materials in the whole electrode). All these strategies require carefully designed electrode microstructures. Conventional structures, with randomly-aligned polymeric binders of reasonable weight content, are not strong enough to support such electrodes^{9,12-14}. Their highly tortuous electron and ion transportation pathways significantly lower the electrochemical performances¹⁵.

No reports to date have detailed a high-performance electrode design successfully implementing all three strategies^{10,16} (free-standing electrode with $>50 \text{ mg cm}^{-2}$ areal loading and $> 95 \text{ wt.}\%$ active content). Those implement one or two of these strategies often sacrifice power densities and stabilities to achieve high energy densities.^{9,17}

The challenges stem from the inherent trade-offs in existing electrode structures:

- An electrode with high active content struggles to achieve high areal loading/free-standing structure^{9,10,16}, or to achieve good performance, due to the insufficient structure support and electron conductivity. Vice versa, free-standing and high-areal-loading electrodes usually have active contents below 80 wt.%¹⁸⁻²⁰.
- Achieving high electron and ion conductivity simultaneously is challenging^{21,22}. A high content of carbon black/binders will inevitably reduce the porosity and increase pore tortuosity.

Clearly, it is difficult to further enhance cell performances based on the existing electrode structures. Any novel structures need to meet the following prerequisites: a highly conductive network with both horizontal and vertical robustness, a low-tortuosity pore network that can access all the particle surface, and active particles that are evenly distributed and firmly attached to the conductive network.

While electrospinning is an ideal and scalable method to fabricate such networks^{23,24}, an optimal approach for introducing active particles has not been identified. Particles introduced within the electrospun fibres²⁵ would leave unnecessarily high porosity (>90%) and thus low energy density^{23,26}. Introducing the particles into the electrospun network²⁷ would exclude the use of commercially-available large particles, and would require additional binder/conductive additives, leading to inferior performance^{28,29}. Both routes have resulted in electrodes with lower active contents than the conventional electrodes, with no obvious improvement in energy/power density.

In this study, we synthesised an ideal Na-ion battery electrode structure by introducing the active particles through electrospraying simultaneously with electrospinning, a method termed co-electrospinning-electrospraying, or co-ESP. Both methods are highly scalable techniques³⁰.

While previous efforts of combining electrospinning and spraying did not fabricate electrodes with state-of-art performance^{31,32}, this work shows that the overlooked particle size effect and the absence of binder/conductive additives are keys to achieving good performance. When the electrosprayed particles are significantly larger than the pores of the electrospun fibre network, they are strongly bound through spatial constrictions without binders, promoting the interphase contact while exposing the particle surfaces to electrolyte. This allows a carbon nanotube-embedded carbon nanofibre (CNTF) network to function as the conductive additive, binder and current-collector with only 2.5 wt.% content.

The synthesised high-active-content, free-standing and binder-free electrodes for Na-ion batteries met all the prerequisites and showed one of the best performances at high-areal loading among all reported Li-ion and Na-ion battery electrodes. With 97.5 wt.% carbon-coated $\text{Na}_2\text{V}_3(\text{PO}_4)_3$ (NVPC) content, the electrodes demonstrated record-high stable areal loading

(up to 296 mg cm⁻² for NVPC, 120 mg cm⁻² for hard carbon) and rate performance (200 C at 4 mg cm⁻² and 5 C at 296 mg cm⁻²). The electrodes exhibited low polarisation, high capacity retention and cycling stability, and state-of-art energy density/power densities across all areal loadings, in both half-cells and full cells. With the assist of multiscale synchrotron-based X-ray computed tomography, we found that the superior performance was linked with the ideal pore structures, high electron accessibility, and hierarchically porous particles. Finally, pouch cells with capacities up to 200 mAh were assembled using co-ESP electrodes, demonstrating their scaling-up potential.

Results and discussion

The co-ESP fabrication of electrodes

Figure 1a illustrates the schematics of the co-electrospinning-spraying (co-ESP) set-up. The electrospinning slurries were mixtures of polyacrylonitrile (PAN), and carbon nanotube (CNT) in a dimethylformamide (DMF) solvent, where PAN served as the electrospinning carrier and carbon precursor. The electrospaying slurries were mixtures of polyethylene oxide (PEO) and commercial NVPC particles in DMF, with PEO functioning as both the electrospaying carriers and dispersant.

The areal loadings (thicknesses) of the electrodes were controlled by the total volume of slurries, and the active contents were controlled by the volume ratios of electrospinning/spraying slurries. The detailed fabrication process is summarised in the Method section and illustrated in **Figure S1**, with an accompanying video provided in **Video S1**.

In contrast to conventional electrospayed battery electrodes, which use metal salt solutions³³, we employed a highly concentrated suspension. This accelerated the electrospaying of NVPC by over tenfold³⁴, aligning its rate with the electrospinning to achieve the desired active content. This change also ensured a comparable fabrication time with the conventional slurry-casting and drying process.

Following co-ESP, the mats were calcined to remove the PEO and pyrolyse the PAN. The resulting electrodes, shown in **Figure 1b**, exhibited remarkable flexibility and a fabric-like texture. Notably, our lab-scale process is capable of fabricating electrodes with up to 600 cm² per batch (**Figure 1b**), enough for 300 CR2032 coin cells, highlighting co-ESP's strong potential for scaling up.

Regarding morphology, **Figure 1c** shows that the co-ESP electrode consisted of a percolating, inter-supported network of CNT-embedded CNF (CNTF), which homogeneously

encapsulated the NVPC cathode particles. The morphologies of NVPC particles and co-ESP NVPC electrodes, both as-fabricated and post-pyrolysis, are detailed in **Figure S2**. The fibres, with diameters of approximately 150 nm and lengths of up to 1 cm (**Figure S3**)³⁵, are two orders of magnitudes longer than the CNTs typically used in battery electrodes^{9,36}. Such a high length-to-diameter ratio is beneficial to the formation of robust supporting backbones at low mass contents^{37,38}, while leaving sufficient porosity. CNT was embedded into the PAN-derived CNF, with a weight content of 40 wt.%^{39,40} (**Figure S4, S5**), enhancing the network's conductivity by an order of magnitude (**Figure S6**). The Raman spectrum of co-ESP NVPC and hard carbon electrodes indicated a higher degree of graphitisation than typical PAN-derived carbon pyrolysed at the same temperature (**Figure S7**).

The size effect of co-ESP electrodes

Notably, the co-ESP method allowed for the introduction of particles larger than the pores of the fibre network (**Figure 1e**). This enabled strong particle binding through the spatial constraints of the network, thus eliminating the need for binders and conductive additives. The average NVPC particles size was 20 μm , significantly larger than the average pore size of the CNTF network (2 μm) (**Figure S8, S9**). Consequently, this network fulfils the roles of conductive additive, binder, and current collector, while also providing adequate porosity for electrolyte immersion. In contrast, when particles smaller than the pore sizes were introduced, as shown in **Figure 1d**, they were poorly bound to the network, while resulting in insufficient electrical contact (**Figure 1f**).

To confirm the importance of particle sizes, small NVPC particles were produced by mildly ball-milling the pristine NVPC particles (**Figure 1d**). The average diameter of ball-milled particles (300 nm) was well below the average pore size of electrospun fibre network (2 μm) (**Figure S9**). The ball-milling did not induce any crystal structure changes or impurities (**Figure S10**), which can occur under harsher milling condition⁴¹. The crystalline sizes remained unchanged, confirming that the ball-milling only broke down the secondary particles⁴². Na-ion half-cells were assembled with pristine and ball-milled co-ESP NVPC cathodes of 18 mg cm⁻², 97.5 wt.% active loading (1.5 wt.% CNF/1 wt.% CNT) (**Figure 2a**).

Both electrodes showed near theoretical initial discharge capacities (~110 vs 117 mAh g⁻¹) under 0.1C. However, the ball-milled electrode showed a lower initial coulombic efficiency (ICE) of 93.8% compared to 97.7% of the pristine electrode (**Figure S11**) likely due to more sodium being consumed in the formation of the cathode-electrolyte interface (CEI) on the ball-milled particles⁴³. Additionally, ball-milled electrode demonstrated poorer rate performance (**Figure 2b**). The pristine co-ESP NVPC electrode retained 72.1% and 36.8% of its theoretical capacity at 5C and 20C, respectively, while the ball-milled electrode retained 47.8% and 0%,

respectively. The conductivities of the electrodes before and after ball-milling were similar (**Figure S12**), indicating the particle sizes did not affect the percolation of CNTF network. The conventional electrode with ball-milled NVPC showed similar voltage profile with pristine particles (**Figure S13**), suggesting the electrochemical properties did not deteriorate with ball-milling.

After 100 cycles at 0.2C, the ball-milled electrode showed 77.4 % capacity retention, notably lower than the 99.6 % retention of the pristine electrode (**Figure 2c**). Post-cycling, the ball-milled electrode was partly disintegrated, with small NVPC particles detaching the CNTF network, whereas the pristine electrode's morphology remained intact (**Figure S14**). The robustness of the co-ESP electrodes were also demonstrated through sonication (**Video S2, S3**). Powders detached from the ball-milled electrode from the start, while the pristine electrode remained intact throughout the sonication process. Nevertheless, both electrodes exhibited significantly better rate performance than the conventional slurry-casted electrode (**Figure 2g**).

The poorer rate performance and cycling stability of the ball-milled electrodes are attributed to the weaker binding of smaller particles.

Unlike the pristine particles (**Figure 2d**), the ball-milled particles were much smaller than the pore of the CNTF network and were not bound by spatial constrictions (**Figure S8, S9**). These particles were only loosely attached to the CNTF network, resulting in high contact resistance. Additionally, not all particles were directly in contact with the conductive network, requiring electrons to traverse multiple particle-particle interfaces to reach these particles, further increasing resistance^{44,45} (**Figure 2e**). Since the ion diffusion and insertion/extraction should be quicker as particles became smaller⁴⁴, the poor rate performance of the ball-milled electrode was likely because of the poor electronic conduction.

Therefore, CNTF network is especially ideal for encapsulating commercial electrode materials of Li and Na-ion batteries, most of which have secondary particle sizes of 5-50 μm ⁴⁶. To demonstrate this, we have fabricated co-ESP LiFePO₄-C LIB cathode, SiO_x-C and graphite LIB anodes, as shown in **Figure S15**. The voltage profiles of these electrodes are shown in **Figure S16**. All electrodes showed high areal capacities, high specific capacities, and small overpotential.

Previous attempts to fabricate battery electrodes using combinations of electrospin and spray have not demonstrated competitive areal loading, active content, rate performance, or cycling stability compared to other state-of-the-art techniques^{31,32}. This is likely because nano-sized particles were used. Additional binder/conductive additives were added to stabilise the particles, which further deteriorated the performance and significantly reduced the active

content. There was also no in-depth analysis of the merit of the co-ESP method and the resulting structures in previous works, which we are aiming to do here.

Given the significantly superior performance, we will only use pristine micron-sized NVPC in the co-ESP NVPC electrodes for the remainder of this work.

Performance of co-ESP electrodes with different CNTF content

Given the critical role of the CNTF network, it is important to investigate its minimum content required to provide sufficient electron conductivity and structural support, thereby achieving the highest energy density.

We synthesised electrodes with active contents of 90 wt.%, 97.5 wt.%, and 99 wt.% (**Table S1**), all with areal loadings of ca. 18 mg cm⁻². Electrodes with active content above 99% were too fragile for use in cells.

As shown in **Figure S17**, increasing the active content resulted in sparser fibres. In the 99 wt.% electrode not all particles were in direct contact with the CNTF network.

At 0.1 C, 97.5 wt.% and 90 wt.% electrodes showed similar discharge capacity and polarisation, while the 99 wt.% electrode had lower discharge capacity and discharge plateau (**Figure 2f**). The capacity difference became more pronounced with increasing C-rate. At 10C, the 99 wt.% electrode showed no discharge capacity (**Figure 2g**). In contrast, both the 97.5 wt.% and 90 wt.% electrodes maintained decent capacities even at 20C. All electrodes demonstrated superior rate performance compared to conventional electrodes.

Apart from lower rate performance, 99 wt.% electrode also showed lower cycling stability than its lower active content counterparts (**Figure 2h**). These results suggest that 1 wt.% CNTF neither provided sufficient electron accessibility for high-rate cycling nor supported the electrode structure adequately. The through plane conductivity of 99 wt.% electrode (1.5 S m⁻¹) was lower than 90 wt.% (18.5 S m⁻¹) and 97.5 wt.% (4.2 S m⁻¹), but was still sufficient according to previous work²¹. However, macroscopic conductivity does not reflect the electron accessibility of individual particles. As shown in **Figure S17**, NVPC particles not in direct contact with the CNTF network could not contribute their capacities at high rates. In contrast, active particles in 97.5 wt.% and 90 wt.% electrodes were all connected to the CNTF network, (**Figure 2i**) and had sufficient electron accessibility, shifting the rate-limiting process to ion transportation²¹. This explains why further reducing the active content beyond 97.5 wt.% showed only marginal improvement.

Thus, 97.5 wt.% is the optimal active content for the co-ESP NVPC electrode, balancing performance, electrode robustness, and active content. We will use this composition throughout the rest of this work. This active content brings 24.4% higher energy/power density

than a commercial 25 mg cm⁻² electrode (90 wt.% NVPC, 5 wt.% PVDF, 5 wt.% carbon black, 15 µm aluminium foil, **Figure 2j**) even without considering the performance benefit of co-ESP electrodes.

Previous efforts to achieve high areal loading and superior rate performance often gave up controls over the active content^{10,18}, resulting in overall loss in the energy/power density. The co-ESP electrode, however, has demonstrated an uncompromised solution, maintaining high active content alongside excellent performance, while having an active content significantly higher than other high-loading electrodes^{9,47}.

Morphology benefit of co-ESP NVPC electrodes

Co-ESP NVPC electrodes have demonstrated remarkable rate performance and stability with high active contents. To further understand the morphology benefits, synchrotron-based micro- and nano-computed tomography (micro- and nano-CT) were employed to characterise multiscale features of the electrodes (**Figure 3a-f**). Micro-CT was used to resolve the morphology of particles and external pores (**Figure 3a, b**), with the electrodes characterised in a compressed state to mimic their condition in cells. The nano-CT was used to resolve the particles internal pores (**Figure 3c**), though it could not resolve all the CNTFs due to their small diameter relative to the resolution (150 nm vs 47 nm) and the low visibility of carbon materials in the presence of NVPC⁴⁸.

From **Figure 3a**, it is evident that the co-ESP NVPC electrode comprises well-distributed large NVPC particles and interconnected pores. A single NVPC particle resolved by the nano-CT (**Figure 3c**) revealed an internal porosity of 39.4% with an average pore size of 582 nm, based on an average of 20 particles. All internal pores were percolated and accessible from the particle surface.

Upon compression at 4 MPa, the thickness of the electrodes reduced significantly, as did the volume of external pores (**Figure 3b**). The thickness of the co-ESP electrodes was extracted from their compression curve (**Figure S18**). Uncompressed, these electrodes were more than four times thicker than conventional slurry-casted cathodes (NVPC: PVDF: CB = 90:5:5) of the same loading (**Figure 3d**), resulting in only 25% of the electrode active density (weight of active materials per volume). After assembly in cells, their thickness reduced by 70%, reaching 91% active density of conventional electrodes.

This high compressibility is an essential feature of the co-ESP NVPC electrode. As shown in the cross-section images (**Figure S3**), the CNTFs tend to align in-plane due to the layered deposition of electrospun fibres. The intrinsic flexibility of CNTFs granted the co-ESP electrode the ability to maintain structural integrity even after 70% strain (**Figure 3b, d**), enhancing the contact between the electrode and cases/metal tabs without a current collector. For half cells

with the areal loadings higher than 150 mg cm^{-2} , sufficient electric connection between the electrode and the coin cell case can be achieved without the springs and spacers.

The volume compositions of different electrode components after compression are summarised in **Figure 3e**. Note that the external porosity only considered the pores outside the NVPC particles, while total porosity included pores both outside and inside the NVPC particles, acquired from micro-CT and nano-CT respectively.

After compression, the electrode had 55.8% total porosity, with external porosity at 27.1%. The porosity was uniform across the cell thickness (**Figure S19**). The total porosity is higher than most reported electrodes, although previous works rarely considered pores inside particles^{26,49}. Therefore, external porosity is a better parameter for comparison. Active particles comprised 94.1 vol.% of the solid phase, indicating efficient utilisation of the electrode volume.

Other microstructural parameters after compression are summarized in **Figure 3f**, with detailed summaries available in **Table S2**. When uncompressed, the external pore tortuosity of the co-ESP NVPC electrode was ca. 1.1, identical across the x, y, and z directions, indicating a homogeneous pore structure. After compression along the z direction, the z-tortuosity increased to 2.0. Conventional electrodes typically have pore tortuosities of 5-8 due to the presence of carbon binder domain (CBD), which refers to the composite cluster of binder and conductive additive^{49,50}. Although CNTFs could not be resolved, they are not expected to significantly increase tortuosity because of their low volume content (<3 vol.%) and small diameters relative to external pores (150nm vs 10 μm , **Figure S3**). The low z-tortuosity ensures smooth through-plane transportation of Na-ions.

In the conventional electrodes the presence of highly tortuous CBD has been proven to be the main reason of sluggish ion transportation in the pore^{28,29,51} (**Figure 3g**). Even without binder, the nano-sized conductive additives would also significantly increase the pore tortuosity^{52,53}. CBD is also the reason that the ion transportation and electron conduction cannot be simultaneously increased in conventional electrodes^{50,54}.

The absence of CBD or any nanosized conductive additives in our co-ESP NVPC electrodes significantly accelerated ion transportation, which is the rate-limiting process when electron conduction is sufficient²¹. Additionally, the surface of NVPC particles were fully accessible to sodium ions, maximizing the Na-ion intercalation/insertion interface (**Figure 3h**)⁵⁵.

The ion transportation was further enhanced by hierarchical internal pores in the NVPC particles (**Figure 3c**), which shortened the diffusion pathway of Na-ions in the NVPC solid by approximately 20-fold. This leveraged the fact that sodium diffusion in the electrolyte is at least five orders of magnitude faster than in the solid NVPC phase^{56,57}.

For electron conduction, the percolating CNTF network ensures electronic access to all NVPC particles, while the coated carbon on the NVPC guarantees uniform electron accessibility across the particles. Conventional electrodes require at least 5 wt.% CBD to ensure carbon black percolation⁵⁸. In contrast, due to the intrinsic interconnecting nature of the CNTF network, there is no theoretical percolation threshold. Good macroscopic electronic conductivity was achieved with even less than 1 wt.% CNTF loading, despite the insufficient electron accessibility of individual particles.

The CNTF network also binds the particles through spatial constriction, providing a much stronger binding force than the van der Waals bond of conventional binders⁹. On the other hand, larger particles applied stress to the fibres caging them, securing their electrical contact. Thus, in the co-ESP electrode, high conductivity, fast ion transportation, and robust structure are achieved simultaneously (**Figure 3d, e** and **Figure 2i, j**) with only 2.5 wt.% inactive content. Especially, both electron conduction and ion conduction pathways are minimised, creating an ideal electrode structure as predicted by previous work⁴⁴. Since ion diffusion and electron conductivity have been found to co-limit the performance²¹, this results in the outstanding rate performance and stability of the co-ESP NVPC electrodes.

High areal loading, high-performance half-cells enabled by CNTF network

The co-ESP NVPC electrodes exhibited an intrinsic ability to support high-areal-loading active materials thanks to the inter-supportive nature of the CNTF network. Unlike conventional electrodes, there is no fundamental limitation to the thickness and the areal loadings of co-ESP electrodes. The thickness and areal loading were controlled by adjusting the total amount of raw materials in the co-ESP fabrication process, as detailed in **Table S3**.

Half-cells were assembled with co-ESP NVPC cathodes of up to 49.6 mg cm⁻² areal loading (**Figure 2a**). Cross-sectional images of co-ESP NVPC electrodes with different areal loadings are shown in **Figure S20**. When the areal loading exceeded 50 mg cm⁻², the half-cells began to exhibit serious over-charging after 15-20 cycles (**Figure S21**), preventing further increases in areal loading in half-cells. This was previously attributed to the degradation of metallic anode^{9,59}, which is confirmed by the intact structure of the co-ESP NVPC cathodes (**Figure S14**), and the severe degradation of Na metal anodes (**Figure S22**) after cycling. The addition of fluoroethylene carbonate (FEC) to the electrolyte slowed the degradation but could not eliminate it (**Figure S23**)^{60,61}. Thus, the co-ESP electrodes' ability to hold higher areal loading will be demonstrated in full cells.

All co-ESP NVPC electrodes showed state-of-the-art rate performance and cycling stability for their respective areal loadings. At the lowest areal loading of 4.3 mg cm⁻², co-ESP NVPC

electrodes showed decent capacity even at 200C, while the 49.6 mg cm⁻² electrodes were usable at 10C (**Figure 4a-d**). The 4.3 mg cm⁻² cell was cycled at 50C for 5000 cycles with 84.8% capacity retention, and the 49.6 mg cm⁻² cell was cycled at 0.2C for 200 cycles with 97.5% capacity retention (**Figure 4e**).

High areal loading co-ESP NVPC electrodes did not exhibit significantly higher degradation rate than their low loading counterparts, a common issue in other high-areal-loading cathodes^{9,62}. This can be attributed to the following factors:

1. The CNTF network physically bound the NVPC particles and absorbed their volume changes during charge/discharge cycles, avoiding the loss of electron accessibility;
2. The absence of CBD prevented pore clogging by the formation of CEI, preserving fast ion transportation;
3. The combination of the above factors prevented the NVPC particles disintegration caused by the inhomogeneous sodiation.

Thus, the co-ESP electrodes overcame the three main causes of the accelerated degradation in high-areal-loading electrodes²⁸.

The detailed electrochemical test result across all areal loadings (**Figure S24**) were summarised into **Figure 4f** and **g**, demonstrate how specific capacities and areal capacities changed with C-rate and areal loading. When cycled at 0.1C, the specific capacities remained almost invariant until the areal loading reached 23.9 mg cm⁻². Increasing the loading further to 49.6 mg cm⁻² reduced the capacity to 89.2% of the theoretical capacity. In comparison, other Na-ion cathode works did not report more than 80% capacity retention for areal loadings above 10 mg cm⁻²^{7,63}. The average discharge voltage is summarised in **Figure S25**.

On the other hand, the 4.3 mg cm⁻² co-ESP NVPC's retained 71.8% of the theoretical capacity at 100C, and 36.4% at 200C. Increasing the areal loading caused the specific capacities to reduce more pronouncedly with increasing C-rate, as expected for all high-areal-loading electrodes^{9,18}. However, the 11.3 mg cm⁻² electrode still retained 25.6% of the theoretical capacity at 50 C, while the 49.6 mg cm⁻² electrode retained 33% at 10C, demonstrating one of the best rate performances at this level of areal loading among all Na and Li-ion batteries^{16,64-66} (detailed comparisons in **Table S4, 5**).

Figure 4g shows that 49.6 mg cm⁻² electrode retained 3.9 and 1.9 mAh cm⁻² areal capacity at 2C and 10C, respectively, demonstrating that high areal capacity and high charge/discharge current were achieved simultaneously. These state-of-art rate performances and stabilities confirmed the structural merit of co-ESP electrodes.

Electrochemical impedance spectroscopy (EIS) of the electrodes showed low Ohmic resistances across all samples (**Figure S26**). While Ohmic resistance increased with areal

loading, the polarization resistance decreased, consistent with previous report⁶⁷. This reduction is mainly due to the reduced charge-transfer resistance for Na intercalation/extraction, facilitated by the higher number of active sites.

The data in **Figure S24** were summarised in two Ragone plots (**Figure 4h, i**). Previously reported Na-ion battery half-cell data from the literatures were included in the same figures^{4-7,63,68-71}. Note that most literature did not disclose sufficient information to calculate the energy/power densities of the whole cells, such as electrode porosities and the weight of electrolytes and separators. For a better comparison, the half-cell energy/power densities in this work considered only the weight of cathodes, including the current collector. Literatures values were recalculated under the same standard, as presented in **Supplementary Appendix 3**. The combination of energy/power densities of co-ESP electrodes leads by a noticeable margin among reported Na-ion battery electrodes, attributing to a combination of high capacity retention, high active content, and superior rate performance.

Previously, the highest reported areal loading of Na-ion batteries' cathodes was 60 mg cm⁻², where no cycling or rate data were presented⁷. The second highest was 48.9 mg cm⁻², which showed much inferior rate performance and cycling stability than the 49.6 mg cm⁻² co-ESP NVPC electrode⁶³.

The half-cells data were also compared with high-areal-loading lithium-ion half-cells (**Table S5**). Although the NVPC co-ESP electrodes' energy densities do not match those of lithium cobalt oxides (LCO) and lithium nickel manganese cobalt oxides (NMC) cathodes, they are comparable to lithium iron phosphate (LFP) cathodes, the second most widely used cathode material in electric vehicles.

Ultra-high loading full cells and pouch cells

Na-ion full cells (coin cells) were assembled using co-ESP NVPC cathodes and co-ESP hard carbon (HC) anodes (**Figure 5a**). The high-performance glucose-derived hard carbon (HC) was synthesised through a facile method as detailed in the previous literature⁷². The voltage-capacity profile and the cycling stability of the co-ESP HC half-cell is demonstrated in **Figure S27**. The composition of fabrication raw materials is presented in **Table S6**. The PAN-derived CNF, embedded CNT and HC were all active sodium storage materials⁷³⁻⁷⁵, in which the HC contributed >97% of the total capacity.

The morphology of the co-ESP HC anode is shown in **Figure S28**, where nano-sized HC particles are agglomerated into secondary particles of average size of 9.9 μm, bound by the CNTF networks through spatial constriction, similar to NVPC particles.

By maintaining the cathode/anode mass ratios at 2.5:1, we assembled full cells with cathode areal loading ranging from 25.4 mg cm⁻², an industry-relevant areal loading, to a record high of 296 mg cm⁻². The maximum areal loading of full cells significantly exceeded the half-cells due to the absence of the problematic Na metallic anode. A 296 mg cm⁻² loading was realised by layering two 148 mg cm⁻² co-ESP NVPC cathodes. In comparison, the conventional electrodes would crack and delaminate from the current collector at areal loadings over 50 mg cm⁻² (**Figure S29**). Detailed full cell compositions are shown in **Table S7, 8**, with a typical conventional cell composition provided in **Table S9**. This represents the highest areal loading to date that can cycle stably among reported Na-ion batteries (**Table S10**) and Li-ion batteries full cells (**Table S11**).

The ICE of the 25.4 mg cm⁻² full cell was 88.9% (**Figure S30**). Due to the high ICE of the co-ESP NVPC half-cell, the lower ICE was mainly attributed to the irreversible sodium intercalation to the HC anode and the formation of solid-electrolyte interphase (SEI)⁷⁶, which can be enhanced through electrolyte optimisations⁷⁷. The ICE decreased with increasing areal loading, reaching 77% at 296 mg cm⁻², likely due to the increased irreversible sodium plating, a common issue for thick anodes⁷⁸.

The co-ESP full cells exhibited superior rate performance (**Figure 5b, c**). Detailed electrochemical testing results are available in **Figure S31**. The average discharge voltage is shown in **Figure S32**. The 25.4 mg cm⁻² full cells delivered 58% of theoretical capacity at 10C, and 17% capacity at 50C. The full cell with 298 mg cm⁻² cathode loading exhibited 76.5% of theoretical capacity at 0.1 C. Even at 2 C it still delivered 10 mAh cm⁻², much higher than a typical conventional electrode (<3 mAh cm⁻²).

The full cells also exhibited great stability. The 298 mg cm⁻² loading cell exhibited 73.4% capacity retention after 200 cycles at 0.2 C (**Figure 5d, Figure S31**). A 60.7 mg cm⁻² full cell had 92.1 % capacity retention after 200 cycles at 0.2 C and 79.6 % after 1000 cycles at 1 C.

The EIS of full cells (**Figure S33**) followed similar trend as half-cells (**Figure S26**): Ohmic resistance increased with areal loading, while polarization resistance drastically decreased.

The energy/power densities of co-ESP full cells were summarised in Ragone plots (**Figure 5e, f**), compared with previously reported Na-ion full cells^{5,7,63,68,69,71}. The co-ESP full cell exhibited maximum gravimetric energy and power densities of 231.6 Wh kg⁻¹ and 7152.6 W kg⁻¹, respectively. While the maximum areal energy and power densities were 77.7 mWh cm⁻² and 248.4 mW cm⁻², respectively. These performance metrics lead among all reported SIB electrode designs works by significant margin. Thus, uncompromised power and energy were achieved for the co-ESP full cells. Detailed comparisons are provided in **Table S9**.

Similar with half-cells, the gravimetric energy/power densities of all full cells in **Figure 5e** were calculated as in **Supplementary Appendix 3**. The gravimetric energy/power densities of the co-ESP full cells, considering the electrolyte and separator, are also presented in **Figure S34** to better compare with the industry standard. The results were also compared with Li-ion battery full cells in **Table. S11**. The energy densities of co-ESP SIB full cells are on par with reported LIBs, while the power densities are notably higher.

To demonstrate the scale-up potential of co-ESP electrodes, we have assembled pouch cells with ~70 and 200 mAh capacities, which also showed great rate performances and stabilities (**Figure 5g**). Both cells were composed of 100 mg cm⁻² co-ESP NVPC cathodes and 40 mg cm⁻² co-ESP HC anodes.

The 70 mAh pouch cell delivered 24.3 mAh at 1C and 11.8 at 2C charge/discharge rate, showing 33.9% and 16.5% capacity retention, respectively (**Figure 5h**). This remarks the best capacity retention among previous reports of pouch cells with similar areal loading¹³. Cycling stability testing were performed on the 200 mAh cell, exhibiting 80.8% capacity retention after cycling at 0.2C for 300 cycles (**Figure 5i**). The detailed voltage profiles and rate performance of the pouch cells are shown in **Figure S35**. Considering the mass and volume of the whole cell, co-ESP pouch cell delivered an unprecedented gravimetric energy density of 147 Wh kg⁻¹, and a volumetric energy density of 307 Wh L⁻¹, one of the highest among all reported SIB pouch cells. The calculation method is detailed in **Supplementary Appendix 3**.

Future remarks

We have shown that co-ESP SIB full cells can deliver comparable energy densities and much superior power densities compared to existing LFP-based LIBs while using commercial particles. We have also shown the scaling-up potential of co-ESP method, by producing 600 cm² of co-ESP NVPC mat in one batch on a lab-scale electrospinning-electrospraying machine (**Figure 1b**). An industry-scale electrospinning/spraying machine has a production capability of over 20,000,000 m² per year⁷⁹, equivalent to 12 GWh capacity, assuming a mid-of-range areal loading 60 mg cm⁻². These suggest the co-ESP SIBs could be rational alternatives for cheaper and quicker electric vehicles in the future.

However, the current need for a calcination step in fabricating co-ESP electrodes, which is not part of the standard process for conventional electrodes, presents a major barrier to wider application. Integrating the calcination step into battery manufacturing will be costly and energy-intensive. While there have been effort to directly electrospin conductive fibres⁸⁰, their conductivities are far from enough for battery electrodes. Therefore, it is necessary to explore novel techniques to electrospin conductive fibres, which will be the focus of our next stage of research.

Conclusion

In this study, we developed an electrode fabrication technique by concurrently electrospinning CNTF conductive backbones and electro spraying carbon-coated $\text{Na}_3\text{V}_2(\text{PO}_4)_3$ (co-ESP NVPC) onto identical substrates.

Our in-depth 2D and 3D morphology characterisations revealed that the NVPC particles are bound to the CNTF network by spatial constriction, ensuring all pores remain fully accessible for unhindered Na-ion transport. The electrospun CNTF network, while constituting merely 2.5 wt.% of the content, adeptly serves as a binder, conductive additive, and current collector, ensuring electronic connectivity to all NVPC particles.

Due to the fast species transportation and robust structure, the co-ESP NVPC electrodes exhibited superior rate-performance and stability. Notably, particles larger than the pore of CNTF network proved to have better performance than their smaller counterparts as the electro sprayed species. The sturdy CNTF networks facilitated the production of extremely high-areal-loading electrodes with up to 296 mg cm^{-2} areal loading.

Both coin cells and pouch cells, with co-ESP electrodes showed state-of-art and uncompromised energy and power densities, even comparable to lithium-ion batteries, demonstrating the merit of co-ESP method.

Finally the co-ESP is a promising fabrication method to greatly enhance the energy/power density of battery electrode. It is applicable to a variety of commercial cathode and anode materials of Na-ion batteries and Li-ion batteries and is scalable, demonstrating its commercialisation potential.

Experimental procedures

Preparation of electrode active materials

The carbon-coated $\text{Na}_3\text{V}_2(\text{PO}_4)_3$ (NVPC) was purchased from Guangdong Canrd New Energy Technology Co.,Ltd. The NVPC particles are coated with ~1 wt.% carbon on their surface. Hard carbons powder was synthesised by the facile and scalable method reported by literature⁷². The method is that firstly hydrothermal carbonization of 30g D-glucose (d-(+)-glucose, $\geq 99.5\%$, Sigma-Aldrich) with 270 ml deionized water in an autoclave reactor (50% fill volume) and heated to $230 \text{ }^\circ\text{C}$ for 12 h; and then the resulting powder was heated at $80 \text{ }^\circ\text{C}$ under vacuum till fully dried, and finally pyrolysis at $1500 \text{ }^\circ\text{C}$ (ramping rate $5 \text{ }^\circ\text{C}/\text{min}$ from room temperature) for 2h under a continues $500 \text{ ml}/\text{min}$ N_2 gas flow.

Electrodes fabrication by co-electrospinning-spraying

The co-ESP electrodes were fabricated through a simultaneous electrospinning-electrospraying method followed by calcination, or called co-ESP method. The fabrication set-up is modified from Bioinicia LE-50 electrospinning machine. The schematic of the set-up is shown in **Figure 1a**, which consists of two sets of syringes, syringe pumps, and high voltage power supplies for electrospinning and electrospraying respectively. The electrospinning syringe is horizontally placed, and the electrospraying syringe is vertically placed, with a grounded aluminium roller collector placed in the centre. Two high voltage power supplies apply adjustable high voltage to two syringes respectively. During fabrication, the rotation speed of the cylindrical collector was set to 50 rpm to avoid any fibre orientation. Both syringes were moving side to side parallel with the collector to ensure uniform thickness.

The fabrication of NVPC/carbon nanotube-carbon nanofibre cathode (NVPC/CNTF) involved simultaneously electrospinning polyacrylonitrile (PAN)/carbon nanotube (CNT) DMF slurry, and electrospraying polyethylene oxide/NVPC DMF slurry. Composition of electrospinning slurry: 5 w/v% polyacrylonitrile (PAN, Goodfellow), 1 w/v% carbon nanotube (MTI) are dissolved/dispersed in dimethylformamide (DMF, Sigma-Aldrich) solvent. Composition of electrospraying slurry: 2 w/v% PEO (Sigma-Aldrich) and 100 w/v% NVPC are dissolved/dispersed in DMF. The total volume and volume ratio of these two slurries were adjusted to fabricate electrodes with different areal loading and active contents. During the fabrication, the distance of electrospinning syringe to roller collector was fixed at 15 cm, distance of electrospraying syringe to the roller 10 cm. The feeding rate of electrospinning slurry is set to 2 mL h⁻¹, feeding rate of electrospraying slurry changes according to the volume ratio of two slurries in order to synchronise the two processes. The voltage applied to electrospinning syringe was adjusted between 10 to 15 kV to ensure a continuous and drop-free spinning process. Similarly, electrospraying voltage was adjusted between 15 to 20 kV.

The produced NVPC-PEO/CNT-PAN composite mats were peeled off from the roller collector and calcined in 1 % H₂/N₂ atmosphere at 850 °C for 5 h, to eliminate PEO and carbonise PAN fibre to carbon fibre (CNF). Finally, co-ESP NVPC cathodes were acquired.

The sub-micron sized NVPC particles were made through ball-milling. 10 g NVPC and 10 mL tert-butanol were put in a ball-milling jar. Zirconia balls were used as the milling ball with ball-to-powder ratio of 10:1, which were mixed with 1:1:1 weight ratio of 1-mm, 5-mm and 10-mm zirconia balls. The ball-mill was performed at 100 rpm for 6 hours before freeze drying and collecting the powder. Co-ESP ball-milled NVPC electrodes were made using the ball-milled powder through the same co-ESP process, aiming to acquire the same active content.

To fabricate hard carbon (HC) /CNTF anode, same co-electrospinning-spraying method as above was used. The only difference was that the electrospaying slurry is changed to 2 wt.% PEO-50 wt.% HC-DMF. The as-prepared HC/PEO/CNF/PAN composite mats were calcined at 1100 °C for 5 h to acquire HC/CNT-CNF anodes.

The co-ESP LiFePO₄/C (MTI), SiO_x/C (MTI), and graphite (MTI) electrodes were fabricated using the same co-ESP method as above. The active contents of these electrodes were controlled to be 95 wt%.

Electrodes fabrication by conventional slurry casting

Regarding the hard carbon slurry, 90 wt. % hard carbon and 10 wt. % pre-prepared sodium carboxymethyl cellulose (CMC, Mw ~ 250 000, Sigma) binder solution (5 wt.%) in water were well mixed. Electrodes were coated from slurries onto battery-grade Al foil (17 μm in thickness, MTI) followed by drying at room temperature and ambient environment for 6 hours followed by drying in a vacuum oven for 18 hours. Regarding the NVP slurry, 90 wt. % NVP powder, 4 wt. % Super P carbon additive (Sigma) and 6 wt. % pre-prepared poly(vinylidene fluoride) binder (Mw ~ 534,000, Sigma) solution (5 wt.% in N-Methyl-2-pyrrolidone, Sigma) were well mixed. Electrodes were coated from slurries onto battery-grade Al foil (17 μm in thickness, MTI) followed by drying at 80 °C 6 hours followed by drying in a vacuum oven at 80 °C for 18 hours. The mass loading of the resulting electrodes is between ~4 mg cm⁻² for anode, and ~16 mg cm⁻² for cathode.

Materials characterisation

The morphologies of the electrodes were examined by field emission SEM (Zeiss LEO Gemini 1525 FEGSEM), with an acceleration voltage of 5 kV. The particle and pore size distributions were acquired through image analysis in ImageJ.

The TEM images were acquired by JEOL STEM 2100Plus, with an acceleration voltage of 200 kV.

The phase of the electrodes and raw materials were characterized by X-ray powder diffraction (XRD, X'Pert³ Powder, Malvern Panalytical). The Raman spectrum was performed on a Renishaw inVia confocal Raman microscope, using 532 nm laser.

Thermogravimetric analysis (TGA) was performed on a Netzsch STA449C. TGA experiments were performed in air and nitrogen atmosphere, under 5 °C min⁻¹ ramping rating.

Microscope assisted nano-scale x-ray tomography (nano-CT) was performed in Diamond Synchrotron I-13-2 beamline. The energy of X-ray was 8eV and 1950 images were acquired by continuously rotating the sample 180 degrees using an integration time of 1.8s

per radiograph. The spatial resolution was 47 nm and field of view was 150*150*150 μm . Image reconstruction was carried out using a bespoke routine implemented by the I-13-2 beamline scientists.

Micron-scale X-ray tomography (micron-CT) was performed at the European Synchrotron Radiation Facility (ESRF) beamline ID19. The energy of X-ray was 16 keV and 1800 images were acquired by continuously rotating the sample 180 degrees using an integration time of 1s per radiograph. The linear resolution was of 350 nm, with a large field of view of 1*1*1 mm. Image reconstruction was carried out using a bespoke routine implemented by the ID19 beamline scientists.

The reconstructed images from CTs were analysed in the Avizo software, from which the microstructural parameters including volume contents, porosity, pore tortuosity and porosity distribution were extracted^{81,82}.

The in-plane conductivities were measured on a Ossila four-point conductivity tester. The through-plane conductivities were measure by a potentiostat (Metrohm Autolab PGSTAT302N).

The strain-stress curve of co-ESP NVPC electrodes were acquired from the compressive mechanical testings, which was performed on a ZwickRoell ZwickiLine universal testing machine. Sample sizes was 2*2 cm^2 .

Electrochemical characterisation

The electrochemical properties of the electrodes were examined in CR2032 coin cells, assembled in an argon-filled glove box with water and oxygen content both lower than 1 ppm. For high-areal loading co-ESP NVP electrodes, no spacer or spring is needed when assembling the cells. All cells were tested on a Biologic Ultra-precision battery cycler at 25 °C. When assembling half-cells, electrodes (co-ESP electrodes and conventional electrodes) were used directly as cathodes. Sodium metal was rolled and punched into 12 mm-diameter round chips and used as anodes. Celgard 2400 polypropylene membranes were used as separators. 1 M NaPF_6 (Canrd) in ethylene carbonate (EC)/ diethyl carbonate (DEC) (EC/DEC = 1:1, v%, Sigma-Aldrich) with 10% fluoroethylene carbonate (FEC) (Sigma-Aldrich) was used as the electrolyte. The amount of electrolyte is controlled to 3:1 mass ratio relative to the electrode.

The NVPC half-cells were cycled in a voltage range of 2.0-3.8 V. The HC half-cells were cycled in a voltage range of 0.005-2.5 V.

The full cells were assembled using NVPC electrodes (co-ESP electrodes and conventional electrodes) as the cathodes, and HC electrodes (co-ESP electrodes and conventional

electrodes) as the anodes. Celgard 2400 polypropylene membranes were used as separators. 1 M NaPF₆ in ethylene carbonate (EC)/dimethyl carbonate (DEC) (EC/DEC = 1:1, v%) was used as the electrolyte. The full cells were cycled in a voltage range of 0.5-3.8 V. In the cycling of NVPC half-cells and full cells, the charging processes were done in a constant current-constant voltage (CC-CV) mode. In the CC stage, cells were charged to 3.8 V under constant current. Then in the CV stage, the cells were charged with 3.8 V voltage until the current reach 0.05C.

The impedance measurements of all cells were performed on the Biologic Ultra-precision battery cycler with a frequency range of 0.1 to 10 kHz, an amplitude of 10mV was used. All measurements were conducted in a fully discharged state.

The Na-ion monolayer pouch cell was constructed using 40 mg cm⁻² co-ESP hard carbon as the anodes and 100 mg cm⁻² co-ESP NVPC as the cathodes. Both electrodes were pressed under 30 MPa to flatten the electrodes, ensuring their good contact with the separator. The electrolyte consisted of 1M NaPF₆ in a solvent mixture of EC and DEC, mixed in a 1:1 volume ratio. A Celgard 2400 separator was positioned between the anode and cathode and soaked in the electrolyte solution to ensure sufficient ionic transport during cell operation. The thickness of aluminium plastic film is 90 μm, weight 14 mg cm⁻².

The assembly of the pouch cell was performed layer-by-layer in an ambient environment because both hard carbon and NVP are resistant to humidity. The separator was sandwiched between the anode and cathode, and three ends of the layered assembly were sealed first, before being placed in an antechamber of a glovebox for drying at 80°C for 18 hours. After drying, the pouch cell was transferred to the glovebox where oxygen and moisture levels were maintained below 5 ppm, and allowed to cool to room temperature. Then, an electrolyte of 1M NaPF₆ in EC/DEC was injected into the pouch cell, followed by vacuum sealing the final end. The edges of the pouch were heat-sealed at 180°C for 4 seconds to securely encapsulate the electrodes and electrolyte. The sealed cell rested at room temperature for 12 hours before any electrochemical testing to ensure good wettability of both electrodes and the separator.

For pre-sodiation, the pouch cell was constructed with a piece of Na metal positioned against the co-ESP hard carbon electrode, separated by a piece of Celgard 2400. A three-electrodes set-up as described in a previous work was applied to monitor the voltages of cathode and anode individually⁷². The assembly was completed inside a glovebox (O₂ and H₂O levels less than 0.5 ppm). The assembled pouch cell rested for 18 hours before undergoing formation cycles (constant current mode at 30 mA g⁻¹, voltage window from 10 mV to 2.0 V). After pre-sodiation, the pouch cell was opened inside a glovebox to prevent exposure to oxygen and humidity. The pre-sodiated co-ESP hard carbon electrode was then transferred from one

pouch cell to another. It is important to note that during this transfer, a negligible amount of carbon content was lost due to mechanical forces, which could not be measured.

The three-electrode pouch cells were tested on Biologic channels, while or the three-electrode pouch cells were tested on Land CT3002A channels.

Acknowledgement

M.O. would like to thank the funding support from EPSRC (EP/W032589/1). Z.G. and M.T. would like to thank the grants from Faraday institute (NEXGENNA, reference number: FIRG064).

S.Z. acknowledges funding from the Faraday Institution (EP/S003053/1) under the Degradation project (FIRG060).

The authors would like to acknowledge Diamond Light Source for time on Beamline I13-2 under Proposal MG-34782, especially we would like to thank Dr Leonard Turpin for his assistance in finishing the session.

The authors would like to acknowledge the European Synchrotron Radiation Facility (ESRF) for provision of synchrotron radiation facilities under proposal MA-5933 and we would like to thank Dr. Benoit Cordonnier for assistance and support in using beamline ID19.

Author Contributions

M. Ouyang and Z. Guo contributed equally to this work. M. Ouyang conceived the project, designed the experiments, developed the novel fabrication methods and supervised the project. M. Ouyang, G. Li, F. Li fabricated the novel electrodes. M. Ouyang, Z. Guo and K. Zheng assembled the coin cells and conducted electrochemical tests. Z. Guo and K. Zheng assembled the pouch cells and conducted electrochemical tests. M. Ouyang, L.E.S Farran and S. Zhao performed the CT characterisation. L.E.S Farran performed image processing and analysis. M. Ouyang, H. Zhang, Z. Guo, M. Wang and F. Li performed the physical characterisations. Y. Zhao contributed to the experimental design and the development of electrode fabrication. X. Liu, S. Yang, M. Titirici and N. Brandon contributed to the experimental design and the manuscript modification. M. Ouyang and Z. Guo wrote the original manuscript. All authors analysed the data and proof-read the manuscript.

Declaration of interests

The authors declare no competing interests.

References

- 1 Tarascon, J.-M. Na-ion versus Li-ion Batteries: Complementarity Rather than Competitiveness. *Joule* **4**, 1616-1620 (2020). <https://doi.org/10.1016/j.joule.2020.06.003>
- 2 Nayak, P. K., Yang, L., Brehm, W. & Adelhelm, P. From lithium-ion to sodium-ion batteries: advantages, challenges, and surprises. *Angewandte Chemie International Edition* **57**, 102-120 (2018).
- 3 Xiang, X., Zhang, K. & Chen, J. Recent Advances and Prospects of Cathode Materials for Sodium-Ion Batteries. *Adv. Mater.* **27**, 5343-5364 (2015). <https://doi.org/10.1002/adma.201501527>
- 4 Yang, J. *et al.* Constructing micro-nano Na₃V₂(PO₄)₃/C architecture for practical high-loading electrode fabrication as superior-rate and ultralong-life sodium ion battery cathode. *Energy Storage Materials* **24**, 694-699 (2020). <https://doi.org/10.1016/j.ensm.2019.07.002>
- 5 Wei, Q. *et al.* An Ultrahigh-Power Mesocarbon Microbeads|Na⁺-Diglyme|Na₃V₂(PO₄)₃ Sodium-Ion Battery. *Adv. Mater.* **34**, 2108304 (2022). <https://doi.org/10.1002/adma.202108304>
- 6 Gao, L., Chen, S., Zhang, L. & Yang, X. High Areal Capacity Na_{0.67}CoO₂ Bundle Array Cathode Tailored for High-Performance Sodium-Ion Batteries. *ChemElectroChem* **6**, 947-952 (2019). <https://doi.org/10.1002/celec.201900031>
- 7 Lv, Z. *et al.* Controllable Design Coupled with Finite Element Analysis of Low-Tortuosity Electrode Architecture for Advanced Sodium-Ion Batteries with Ultra-High Mass Loading. *Advanced Energy Materials* **11**, 2003725 (2021). <https://doi.org/10.1002/aenm.202003725>
- 8 Hu, L. *et al.* Lithium-Ion Textile Batteries with Large Areal Mass Loading. *Advanced Energy Materials* **1**, 1012-1017 (2011). <https://doi.org/10.1002/aenm.201100261>
- 9 Park, S.-H. *et al.* High areal capacity battery electrodes enabled by segregated nanotube networks. *Nature Energy* **4**, 560-567 (2019). <https://doi.org/10.1038/s41560-019-0398-y>
- 10 Kuang, Y., Chen, C., Kirsch, D. & Hu, L. Thick Electrode Batteries: Principles, Opportunities, and Challenges. *Advanced Energy Materials* **9**, 1901457 (2019). <https://doi.org/10.1002/aenm.201901457>
- 11 Zhang, T. & Ran, F. Design Strategies of 3D Carbon-Based Electrodes for Charge/Ion Transport in Lithium Ion Battery and Sodium Ion Battery. *Adv. Funct. Mater.* **31**, 2010041 (2021). <https://doi.org/10.1002/adfm.202010041>
- 12 Zhang, Y. *et al.* Polymer Molecular Engineering Enables Rapid Electron/Ion Transport in Ultra-Thick Electrode for High-Energy-Density Flexible Lithium-Ion Battery. *Adv. Funct. Mater.* **31**, 2100434 (2021). <https://doi.org/10.1002/adfm.202100434>
- 13 Ryu, M., Hong, Y.-K., Lee, S.-Y. & Park, J. H. Ultrahigh loading dry-process for solvent-free lithium-ion battery electrode fabrication. *Nat. Commun.* **14**, 1316 (2023). <https://doi.org/10.1038/s41467-023-37009-7>
- 14 Hippauf, F. *et al.* Overcoming binder limitations of sheet-type solid-state cathodes using a solvent-free dry-film approach. *Energy Storage Materials* **21**, 390-398 (2019). <https://doi.org/10.1016/j.ensm.2019.05.033>
- 15 Lu, X. *et al.* 3D microstructure design of lithium-ion battery electrodes assisted by X-ray nano-computed tomography and modelling. *Nat. Commun.* **11**, 2079 (2020). <https://doi.org/10.1038/s41467-020-15811-x>
- 16 Sun, H. *et al.* Three-dimensional holey-graphene/niobia composite architectures for ultrahigh-rate energy storage. *Science* **356**, 599-604 (2017).
- 17 Lu, L.-L. *et al.* Wood-Inspired High-Performance Ultrathick Bulk Battery Electrodes. *Adv. Mater.* **30**, 1706745 (2018). <https://doi.org/10.1002/adma.201706745>

- 18 Lee, J. T., Jo, C. & De Volder, M. Bicontinuous phase separation of lithium-ion battery electrodes for ultrahigh areal loading. *Proceedings of the National Academy of Sciences* **117**, 21155-21161 (2020). <https://doi.org/10.1073/pnas.2007250117>
- 19 Li, H. *et al.* Ultrahigh-Capacity and Fire-Resistant LiFePO₄-Based Composite Cathodes for Advanced Lithium-Ion Batteries. *Advanced Energy Materials* **9**, 1802930 (2019). <https://doi.org/10.1002/aenm.201802930>
- 20 Wang, H. *et al.* A Universal Aqueous Conductive Binder for Flexible Electrodes. *Adv. Funct. Mater.* **31**, 2102284 (2021). <https://doi.org/10.1002/adfm.202102284>
- 21 Tian, R. *et al.* Quantifying the factors limiting rate performance in battery electrodes. *Nat. Commun.* **10**, 1933 (2019). <https://doi.org/10.1038/s41467-019-09792-9>
- 22 Orikasa, Y. *et al.* Ionic Conduction in Lithium Ion Battery Composite Electrode Governs Cross-sectional Reaction Distribution. *Scientific Reports* **6**, 26382 (2016). <https://doi.org/10.1038/srep26382>
- 23 Li, X. *et al.* Electrospinning-Based Strategies for Battery Materials. *Advanced Energy Materials* **11**, 2000845 (2021). <https://doi.org/10.1002/aenm.202000845>
- 24 Cavaliere, S., Subianto, S., Savych, I., Jones, D. J. & Rozière, J. Electrospinning: designed architectures for energy conversion and storage devices. *Energy & Environmental Science* **4**, 4761-4785 (2011). <https://doi.org/10.1039/C1EE02201F>
- 25 Kwon, O. H. *et al.* Porous SnO₂/C Nanofiber Anodes and LiFePO₄/C Nanofiber Cathodes with a Wrinkle Structure for Stretchable Lithium Polymer Batteries with High Electrochemical Performance. *Advanced Science* **7**, 2001358 (2020). <https://doi.org/10.1002/advs.202001358>
- 26 Boyce, A. M., Lu, X., Brett, D. J. L. & Shearing, P. R. Exploring the influence of porosity and thickness on lithium-ion battery electrodes using an image-based model. *J. Power Sources* **542**, 231779 (2022). <https://doi.org/10.1016/j.jpowsour.2022.231779>
- 27 Li, Z., Zhang, J. T., Chen, Y. M., Li, J. & Lou, X. W. Pie-like electrode design for high-energy density lithium-sulfur batteries. *Nat. Commun.* **6**, 8850 (2015). <https://doi.org/10.1038/ncomms9850>
- 28 Zhang, M. *et al.* Coupling of multiscale imaging analysis and computational modeling for understanding thick cathode degradation mechanisms. *Joule* **7**, 201-220 (2023). <https://doi.org/10.1016/j.joule.2022.12.001>
- 29 Kroll, M. *et al.* Three-Phase Reconstruction Reveals How the Microscopic Structure of the Carbon-Binder Domain Affects Ion Transport in Lithium-Ion Batteries. *Batteries & Supercaps* **4**, 1363-1373 (2021). <https://doi.org/10.1002/batt.202100057>
- 30 Wang, J., Xu, H., Huo, Y., Wang, Y. & Dong, M. Progress of electrospray and electrospinning in energy applications. *Nanotechnology* **31**, 132001 (2020).
- 31 Xu, Y., Zhu, Y., Han, F., Luo, C. & Wang, C. 3D Si/C Fiber Paper Electrodes Fabricated Using a Combined Electrospray/Electrospinning Technique for Li-Ion Batteries. *Advanced Energy Materials* **5**, 1400753 (2015). <https://doi.org/10.1002/aenm.201400753>
- 32 Kim, J.-M., Park, C.-H., Wu, Q. & Lee, S.-Y. 1D Building Blocks-Intermingled Heteronanomats as a Platform Architecture For High-Performance Ultrahigh-Capacity Lithium-Ion Battery Cathodes. *Advanced Energy Materials* **6**, 1501594 (2016). <https://doi.org/10.1002/aenm.201501594>
- 33 Zhu, C., Fu, Y. & Yu, Y. Designed Nanoarchitectures by Electrostatic Spray Deposition for Energy Storage. *Adv. Mater.* **31**, 1803408 (2019). <https://doi.org/10.1002/adma.201803408>
- 34 Wang, S., Li, S., Sun, Y., Feng, X. & Chen, C. Three-dimensional porous V₂O₅ cathode with ultra high rate capability. *Energy & Environmental Science* **4**, 2854-2857 (2011). <https://doi.org/10.1039/C1EE01172C>

- 35 Zussman, E. *et al.* Mechanical and structural characterization of electrospun PAN-derived carbon nanofibers. *Carbon* **43**, 2175-2185 (2005). <https://doi.org/10.1016/j.carbon.2005.03.031>
- 36 Fang, R. *et al.* The Regulating Role of Carbon Nanotubes and Graphene in Lithium-Ion and Lithium–Sulfur Batteries. *Adv. Mater.* **31**, 1800863 (2019). <https://doi.org/10.1002/adma.201800863>
- 37 Morimoto, T., Kobashi, K. & Okazaki, T. Carbon Nanotube Length Distribution Estimation by One-Dimensional Plasmon Resonance for Solid-State Samples. *The Journal of Physical Chemistry C* **125**, 19362-19367 (2021). <https://doi.org/10.1021/acs.jpcc.1c04539>
- 38 Simien, D. *et al.* Influence of Nanotube Length on the Optical and Conductivity Properties of Thin Single-Wall Carbon Nanotube Networks. *ACS Nano* **2**, 1879-1884 (2008). <https://doi.org/10.1021/nn800376x>
- 39 Almecija, D., Blond, D., Sader, J. E., Coleman, J. N. & Boland, J. J. Mechanical properties of individual electrospun polymer-nanotube composite nanofibers. *Carbon* **47**, 2253-2258 (2009). <https://doi.org/10.1016/j.carbon.2009.04.022>
- 40 Maitra, T. *et al.* Improved graphitization and electrical conductivity of suspended carbon nanofibers derived from carbon nanotube/polyacrylonitrile composites by directed electrospinning. *Carbon* **50**, 1753-1761 (2012). <https://doi.org/10.1016/j.carbon.2011.12.021>
- 41 Shim, J. & Bang, J. H. Overlooked impact of precursor mixing: Implications in the electrochemical performance of battery electrode materials. *Journal of Energy Chemistry* **82**, 56-65 (2023). <https://doi.org/10.1016/j.jechem.2023.03.031>
- 42 Chowdhury, R. *et al.* Revisiting the promise of Bi-layer graded cathodes for improved Li-ion battery performance. *Sustainable Energy & Fuels* **5**, 5193-5204 (2021). <https://doi.org/10.1039/D1SE01077H>
- 43 Zhang, Z. *et al.* Cathode-Electrolyte Interphase in Lithium Batteries Revealed by Cryogenic Electron Microscopy. *Matter* **4**, 302-312 (2021). <https://doi.org/10.1016/j.matt.2020.10.021>
- 44 Zhu, C., Usiskin, R. E., Yu, Y. & Maier, J. The nanoscale circuitry of battery electrodes. *Science* **358**, ea02808 (2017). <https://doi.org/10.1126/science.aao2808>
- 45 Zheng, J., Garcia-Mendez, R. & Archer, L. A. Engineering Multiscale Coupled Electron/Ion Transport in Battery Electrodes. *ACS Nano* **15**, 19014-19025 (2021). <https://doi.org/10.1021/acsnano.1c08719>
- 46 Almar, L., Joos, J., Weber, A. & Ivers-Tiffée, E. Microstructural feature analysis of commercial Li-ion battery cathodes by focused ion beam tomography. *J. Power Sources* **427**, 1-14 (2019). <https://doi.org/10.1016/j.jpowsour.2019.04.019>
- 47 Yang, K. *et al.* Constructing a Highly Efficient Aligned Conductive Network to Facilitate Depolarized High-Areal-Capacity Electrodes in Li-Ion Batteries. *Advanced Energy Materials* **11**, 2100601 (2021). <https://doi.org/10.1002/aenm.202100601>
- 48 Jervis, R. *et al.* X-ray Nano Computed Tomography of Electrospun Fibrous Mats as Flow Battery Electrodes. *Energy Technology* **6**, 2488-2500 (2018). <https://doi.org/10.1002/ente.201800338>
- 49 Hutzenlaub, T. *et al.* FIB/SEM-based calculation of tortuosity in a porous LiCoO₂ cathode for a Li-ion battery. *Electrochem. Commun.* **27**, 77-80 (2013). <https://doi.org/10.1016/j.elecom.2012.11.006>
- 50 Mistry, A. *et al.* Quantifying Negative Effects of Carbon-Binder Networks from Electrochemical Performance of Porous Li-Ion Electrodes. *J. Electrochem. Soc.* **168**, 070536 (2021). <https://doi.org/10.1149/1945-7111/ac1033>
- 51 Ludwig, B., Zheng, Z., Shou, W., Wang, Y. & Pan, H. Solvent-Free Manufacturing of Electrodes for Lithium-ion Batteries. *Scientific Reports* **6**, 23150 (2016). <https://doi.org/10.1038/srep23150>

- 52 Chen, S. *et al.* Nanoscale Iron Fluoride Supported by Three-Dimensional Porous Graphene as Long-Life Cathodes for Lithium-Ion Batteries. *J. Electrochem. Soc.* **167**, 080506 (2020). <https://doi.org:10.1149/1945-7111/ab88be>
- 53 Obradović, M. D. *et al.* A comparative study of the electrochemical properties of carbon nanotubes and carbon black. *Journal of Electroanalytical Chemistry* **634**, 22-30 (2009). <https://doi.org:https://doi.org/10.1016/j.jelechem.2009.07.001>
- 54 Jiang, Z. Y., Qu, Z. G., Zhou, L. & Tao, W. Q. A microscopic investigation of ion and electron transport in lithium-ion battery porous electrodes using the lattice Boltzmann method. *Appl. Energy* **194**, 530-539 (2017). <https://doi.org:https://doi.org/10.1016/j.apenergy.2016.10.125>
- 55 Chauhan, A., Asylbekov, E., Kespe, S. & Nirschl, H. Influence of carbon binder domain on the performance of lithium-ion batteries: Impact of size and fractal dimension. *Electrochemical Science Advances* **3**, e2100151 (2023). <https://doi.org:https://doi.org/10.1002/elsa.202100151>
- 56 Chen, S. *et al.* Challenges and Perspectives for NASICON-Type Electrode Materials for Advanced Sodium-Ion Batteries. *Adv. Mater.* **29**, 1700431 (2017). <https://doi.org:https://doi.org/10.1002/adma.201700431>
- 57 Ponrouch, A. *et al.* Towards high energy density sodium ion batteries through electrolyte optimization. *Energy & Environmental Science* **6**, 2361-2369 (2013). <https://doi.org:10.1039/C3EE41379A>
- 58 Entwistle, J., Ge, R., Pardikar, K., Smith, R. & Cumming, D. Carbon binder domain networks and electrical conductivity in lithium-ion battery electrodes: A critical review. *Renewable and Sustainable Energy Reviews* **166**, 112624 (2022). <https://doi.org:https://doi.org/10.1016/j.rser.2022.112624>
- 59 Qie, L., Zu, C. & Manthiram, A. A High Energy Lithium-Sulfur Battery with Ultrahigh-Loading Lithium Polysulfide Cathode and its Failure Mechanism. *Advanced Energy Materials* **6**, 1502459 (2016). <https://doi.org:https://doi.org/10.1002/aenm.201502459>
- 60 Rodriguez, R. *et al.* In Situ Optical Imaging of Sodium Electrodeposition: Effects of Fluoroethylene Carbonate. *ACS Energy Letters* **2**, 2051-2057 (2017). <https://doi.org:10.1021/acsenergylett.7b00500>
- 61 Lee, J. *et al.* Ultraconcentrated Sodium Bis(fluorosulfonyl)imide-Based Electrolytes for High-Performance Sodium Metal Batteries. *ACS Appl. Mater. Interfaces* **9**, 3723-3732 (2017). <https://doi.org:10.1021/acsami.6b14878>
- 62 Shi, B. *et al.* Low Tortuous, Highly Conductive, and High-Areal-Capacity Battery Electrodes Enabled by Through-thickness Aligned Carbon Fiber Framework. *Nano Lett.* **20**, 5504-5512 (2020). <https://doi.org:10.1021/acs.nanolett.0c02053>
- 63 Geng, Y. *et al.* Homogeneous hybridization of NASICON-type cathode for enhanced sodium-ion storage. *Energy Storage Materials* **49**, 67-76 (2022). <https://doi.org:https://doi.org/10.1016/j.ensm.2022.03.044>
- 64 Yu, C.-Y. *et al.* NaCrO₂ cathode for high-rate sodium-ion batteries. *Energy & Environmental Science* **8**, 2019-2026 (2015). <https://doi.org:10.1039/C5EE00695C>
- 65 Ren, W. *et al.* Self-sacrificed synthesis of three-dimensional Na₃V₂(PO₄)₃ nanofiber network for high-rate sodium-ion full batteries. *Nano Energy* **25**, 145-153 (2016). <https://doi.org:https://doi.org/10.1016/j.nanoen.2016.03.018>
- 66 Fan, Q. *et al.* Coral-shaped porous LiFePO₄/graphene hybrids for high rate and all-temperature battery applications. *Energy Storage Materials* **21**, 457-463 (2019). <https://doi.org:https://doi.org/10.1016/j.ensm.2019.06.020>
- 67 Ogihara, N., Itou, Y., Sasaki, T. & Takeuchi, Y. Impedance Spectroscopy Characterization of Porous Electrodes under Different Electrode Thickness Using a Symmetric Cell for High-Performance Lithium-Ion Batteries. *The Journal of Physical Chemistry C* **119**, 4612-4619 (2015). <https://doi.org:10.1021/jp512564f>

- 68 Hwang, J., Matsumoto, K. & Hagiwara, R. Na₃V₂(PO₄)₃@Carbon Nanofibers: High Mass Loading Electrode Approaching Practical Sodium Secondary Batteries Utilizing Ionic Liquid Electrolytes. *ACS Applied Energy Materials* **2**, 2818-2827 (2019). <https://doi.org/10.1021/acsaem.9b00176>
- 69 Song, H. & Eom, K. Overcoming the Unfavorable Kinetics of Na₃V₂(PO₄)₂F₃//SnP_x Full-Cell Sodium-Ion Batteries for High Specific Energy and Energy Efficiency. *Adv. Funct. Mater.* **30**, 2003086 (2020). <https://doi.org/10.1002/adfm.202003086>
- 70 Lv, Z. *et al.* Electrode Design for High-Performance Sodium-Ion Batteries: Coupling Nanorod-Assembled Na₃V₂(PO₄)₃@C Microspheres with a 3D Conductive Charge Transport Network. *ACS Appl. Mater. Interfaces* **12**, 13869-13877 (2020). <https://doi.org/10.1021/acsaem.9b22746>
- 71 Yu, S., Liu, Z., Tempel, H., Kungl, H. & Eichel, R.-A. Self-standing NASICON-type electrodes with high mass loading for fast-cycling all-phosphate sodium-ion batteries. *J. Mat. Chem. A* **6**, 18304-18317 (2018). <https://doi.org/10.1039/C8TA07313A>
- 72 Guo, Z. *et al.* Investigating the Superior Performance of Hard Carbon Anodes in Sodium-Ion Compared With Lithium- and Potassium-Ion Batteries. *Adv. Mater.* **n/a**, 2304091 (2023). <https://doi.org/10.1002/adma.202304091>
- 73 Zhu, J. *et al.* Nitrogen-doped carbon nanofibers derived from polyacrylonitrile for use as anode material in sodium-ion batteries. *Carbon* **94**, 189-195 (2015). <https://doi.org/10.1016/j.carbon.2015.06.076>
- 74 Bai, P. *et al.* Solid electrolyte interphase manipulation towards highly stable hard carbon anodes for sodium ion batteries. *Energy Storage Materials* **25**, 324-333 (2020). <https://doi.org/10.1016/j.ensm.2019.10.006>
- 75 Vijaya Kumar Saroja, A. P., Muruganathan, M., Muthusamy, K., Mizuta, H. & Sundara, R. Enhanced Sodium Ion Storage in Interlayer Expanded Multiwall Carbon Nanotubes. *Nano Lett.* **18**, 5688-5696 (2018). <https://doi.org/10.1021/acs.nanolett.8b02275>
- 76 Wan, Y., Liu, Y., Chao, D., Li, W. & Zhao, D. Recent advances in hard carbon anodes with high initial Coulombic efficiency for sodium-ion batteries. *Nano Materials Science* **5**, 189-201 (2023). <https://doi.org/10.1016/j.nanoms.2022.02.001>
- 77 Dahbi, M. *et al.* Effect of Hexafluorophosphate and Fluoroethylene Carbonate on Electrochemical Performance and the Surface Layer of Hard Carbon for Sodium-Ion Batteries. *ChemElectroChem* **3**, 1856-1867 (2016). <https://doi.org/10.1002/celec.201600365>
- 78 Singh, M., Kaiser, J. & Hahn, H. Thick Electrodes for High Energy Lithium Ion Batteries. *J. Electrochem. Soc.* **162**, A1196 (2015). <https://doi.org/10.1149/2.0401507jes>
- 79 Omer, S., Forgách, L., Zekó, R. & Sebe, I. Scale-up of electrospinning: Market overview of products and devices for pharmaceutical and biomedical purposes. *Pharmaceutics* **13**, 286 (2021).
- 80 Wang, X.-X. *et al.* Conductive polymer ultrafine fibers via electrospinning: Preparation, physical properties and applications. *Progress in Materials Science* **115**, 100704 (2021). <https://doi.org/10.1016/j.pmatsci.2020.100704>
- 81 Salinas-Farran, L., Batchelor, A. & Neethling, S. J. Multimodal assessment of the curing of agglomerated ores in the presence of chloride ions. *Hydrometallurgy* **207**, 105776 (2022). <https://doi.org/10.1016/j.hydromet.2021.105776>
- 82 Salinas-Farran, L. *et al.* The impact of chloride ions on chalcopyrite leaching: A multiscale and multimodal assessment. *Miner. Eng.* **213**, 108762 (2024). <https://doi.org/10.1016/j.mineng.2024.108762>

Figure legends

Figure 1. Fabrication and 2D morphology of the co-esp NVPC/CNTF electrodes. **a.** Schematic diagram of co-electrospinning-electrospraying fabrication set-up. **b.** Photographic pictures of 600 cm² as-spun NVPC/PAN electrode (above) and calcined 20 cm² co-esp NVPC/CNF electrode (below, containing weight ratio of CNT: CNF: NVPC of 1:1.5:97.5). SEM images of co-esp electrodes with **c.** pristine micron-sized NVPC particles and **d.** ball-milled nano-sized NVPC particles. The schematic diagrams of the NVPC/CNTF co-ESP electrode **e.** composed of pristine micron-sized NVPC particles; **f.** composed of ball-milled NVPC particles.

Figure 2. The performance of co-ESP NVPC cathodes with different particle sizes and active content: **a.** Schematic diagram of a sodium-ion battery half cell; Half cell performance of co-ESP NVPC cathode consist of pristine and ball-milled NVPC: **b.** Rate performance and **c.** 0.2C cycling stability; The schematic diagrams of the morphology and electron transportation path of NVPC/CNTF co-ESP electrode with **d.** pristine NVPC particles and **e.** ball-milled NVPC particles; Half cell performance of co-ESP NVPC with different active contents: **f.** The third discharge curve and **g.** rate performance and **h.** 0.2 C cycling stability; **i.** Electric conductivity of co-ESP NVPC electrode with different CNTF content component's; **j.** composition of co-ESP and conventional slurry-casted NVPC cathode with 25 mg cm⁻² areal loading

Figure 3. Physical properties and 3D morphology of co-ESP NVPC electrodes: The schematics and 3D reconstruction of NVPC/CNTF electrodes, reconstructed from micro-CT scans: **a.** Uncompressed; **b.** compressed; **c.** fine structure of a single NVPC particle (cross-section indicated in yellow); **d.** summary of structural parameters acquired from XCT; **e.** the volume ratio of different components in a compressed NVPC/CNTF electrode; **f.** the thickness of compressed and uncompressed NVPC/CNTF electrodes with different areal loadings and conventional electrodes (current collector included); The schematics of sodium ion transportation in the pores of **g.** conventional electrodes and **h.** co-ESP electrodes

Figure 4. The performance of co-ESP NVPC cathodes with different areal loading: 4.3 mg cm⁻² cathode's **a.** rate performance and **b.** voltage profile; 49.6 mg cm⁻² cathode's **c.** rate performance and **d.** voltage profile; **e.** Cycling stability of different areal loading half cells; **f.** the change of specific discharge capacity with areal loading and cycling rate; **g.** The change of areal capacity with areal

current; Ragone plots of **h.** gravimetric energy density versus power density and **i.** areal energy density versus areal power density, including the data acquired from previous sodium-ion battery half cells for comparison.

Figure 5 The performance of sodium ion batteries full cells and pouch cells made of co-ESP NVPC cathodes and co-ESP HC anodes: a. Schematic diagram of a sodium-ion battery full cell; **b.** the change of specific discharge capacity with areal loading and cycling rate; **c.** The change of areal capacity with areal current; **d.** Cycling stability of different areal loading full cells; Ragone plots of **e.** gravimetric energy density versus power density and **f.** areal energy density versus areal power density, including the data acquired from previous sodium-ion battery full cells for comparison; pouch cell performance with 100 mg cm^{-2} cathode loading: **g.** Schematic diagram of a sodium-ion battery pouch cell; **h.** Rate performance and **i.** Cycling performance of 0.2 Ah, 100 mg cm^{-2} cathode loading pouch cell.

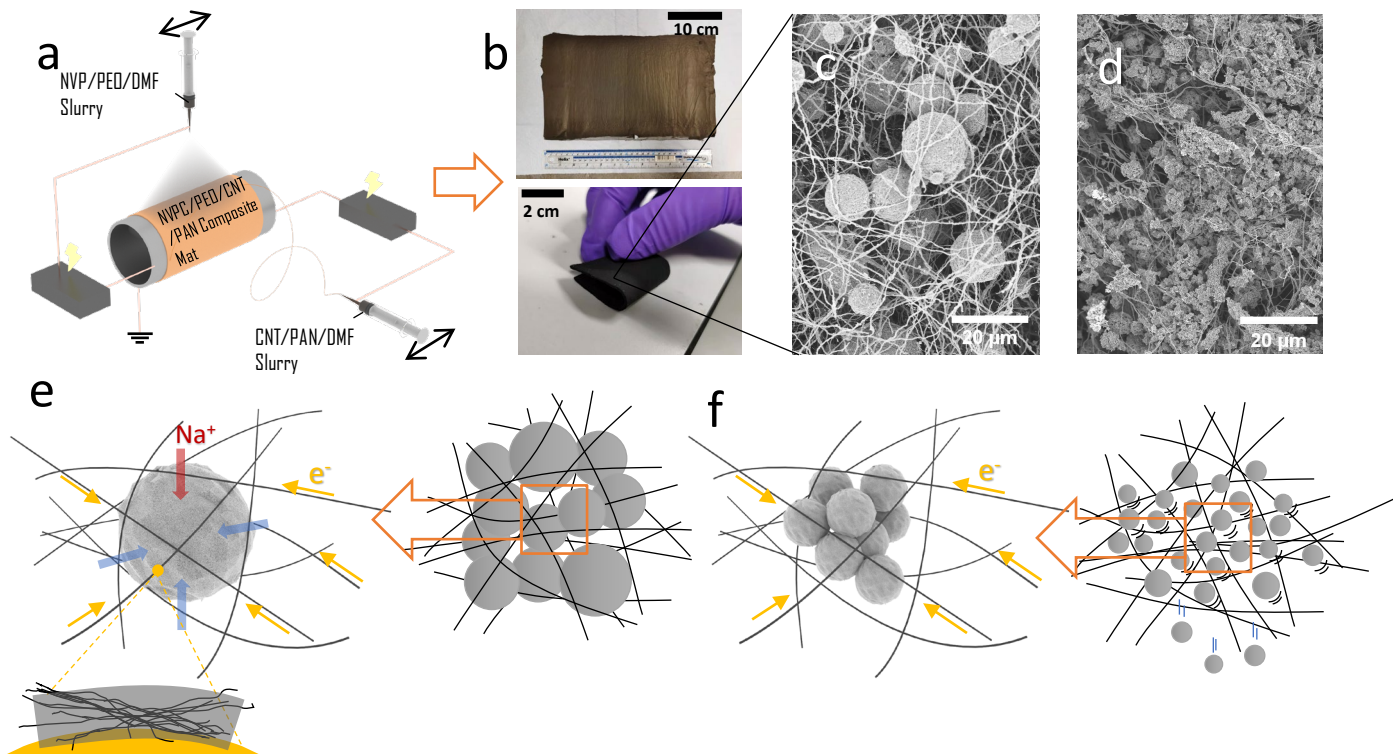


Figure 1. Fabrication and 2D morphology of the co-esp NVPC/CNTF electrodes. **a.** Schematic diagram of co-electrospinning-electrospraying fabrication set-up. **b.** Photographic pictures of 600 cm² as-spun NVPC/PAN electrode (above) and calcined 20 cm² co-esp NVPC/CNF electrode (below, containing weight ratio of CNT: CNF: NVPC of 1:1.5:97.5). SEM images of co-esp electrodes with **c.** pristine micron-sized NVPC particles and **d.** ball-milled nano-sized NVPC particles. The schematic diagrams of the NVPC/CNTF co-ESP electrode **e.** composed of pristine micron-sized NVPC particles; **f.** composed of ball-milled NVPC particles.

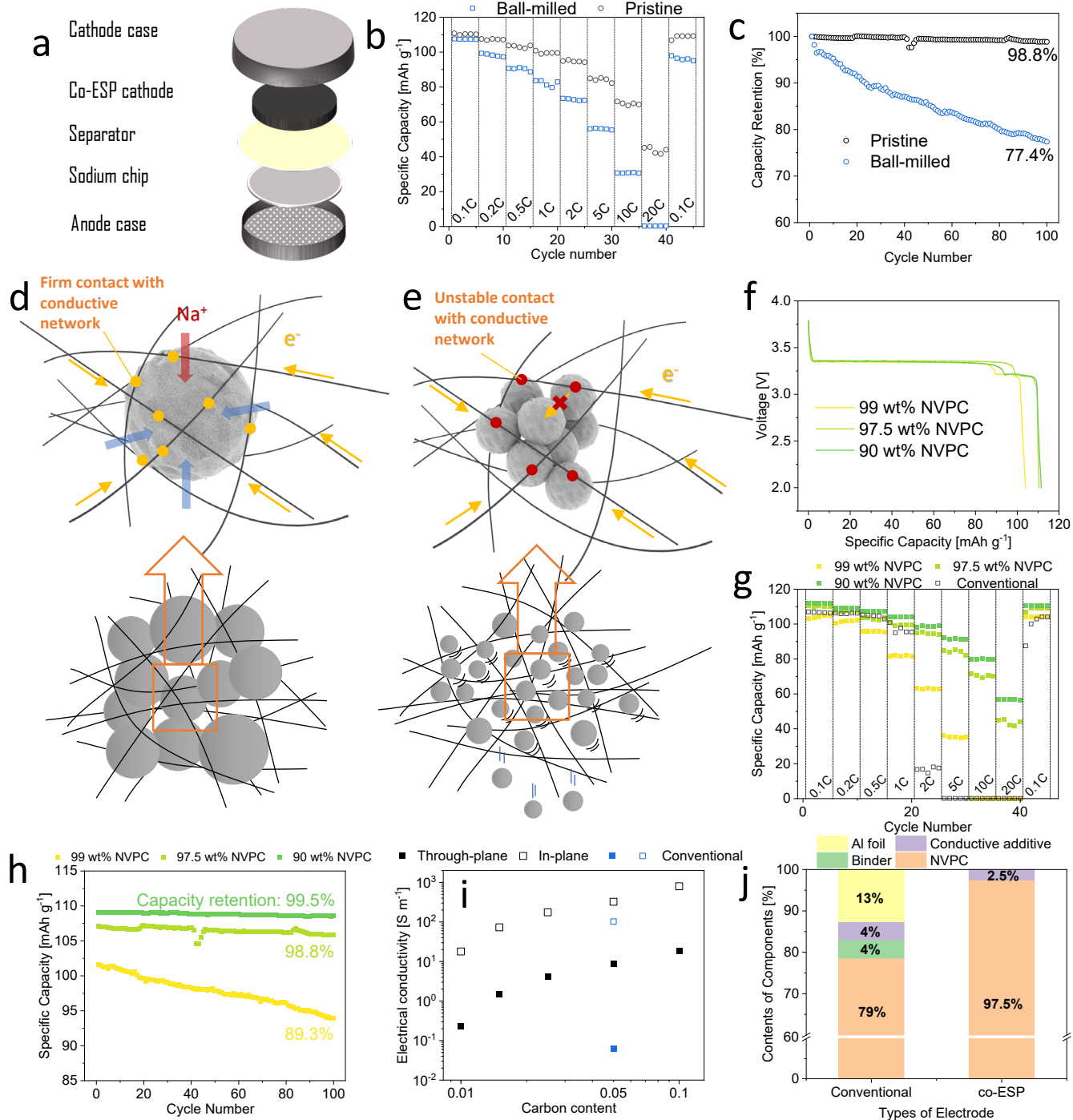


Figure 2. The performance of co-ESP NVPC cathodes with different particle sizes and active content: **a.** Schematic diagram of a sodium-ion battery half cell; Half cell performance of co-ESP NVPC cathode consist of pristine and ball-milled NVPC: **b.** Rate performance and **c.** 0.2C cycling stability; The schematic diagrams of the morphology and electron transportation path of NVPC/CNTF co-ESP electrode with **d.** pristine NVPC particles and **e.** ball-milled NVPC particles; Half cell performance of co-ESP NVPC with different active contents: **f.** The third discharge curve and **g.** rate performance and **h.** 0.2 C cycling stability; **i.** Electric conductivity of co-ESP NVPC electrode with different CNTF content component's; **j.** composition of co-ESP and conventional slurry-casted NVPC cathode with 25 mg cm^{-2} areal loading

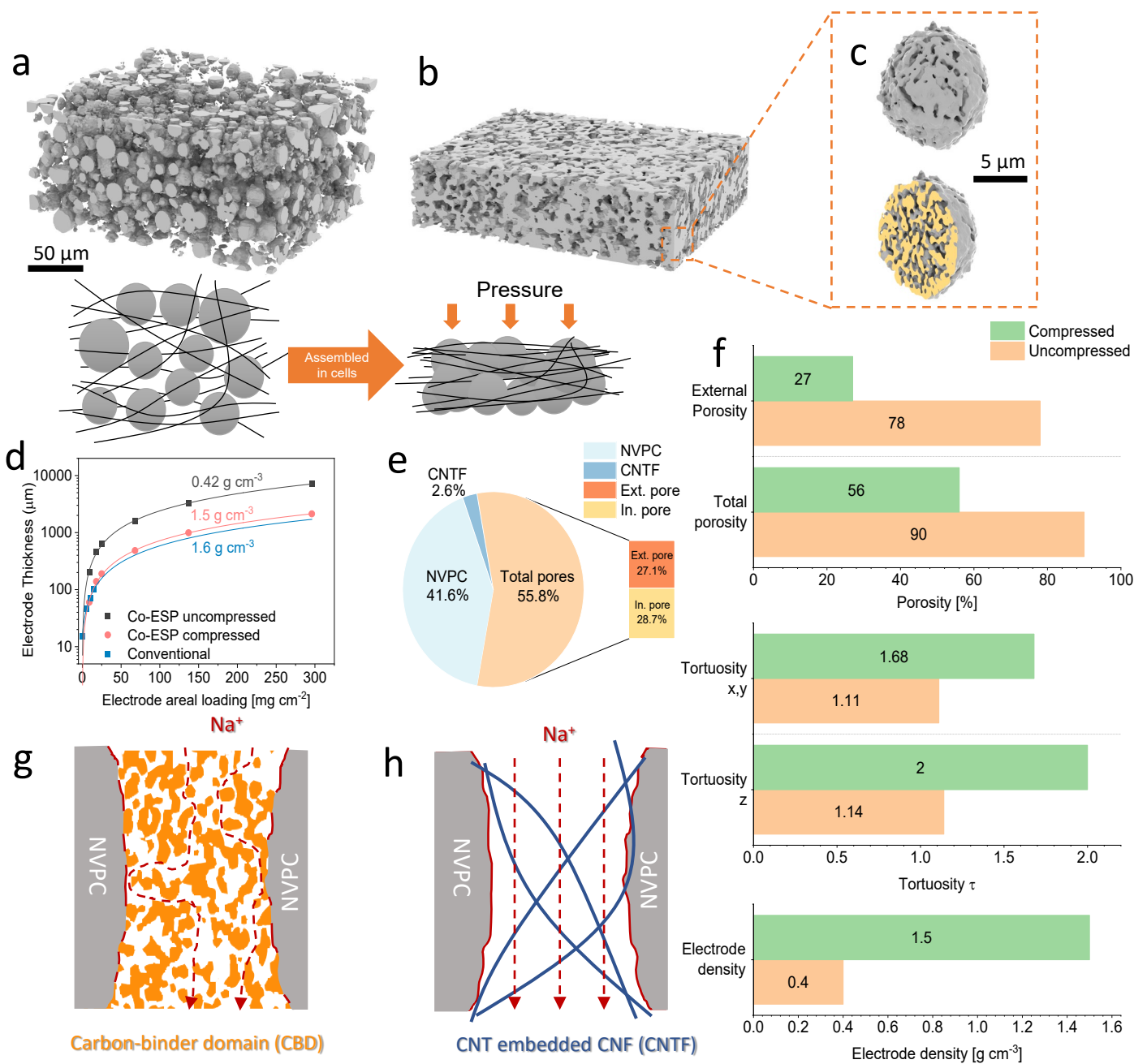


Figure 3. Physical properties and 3D morphology of co-ESP NVPC electrodes: The schematics and 3D reconstruction of NVPC/CNTF electrodes, reconstructed from micro-CT scans: **a**. Uncompressed; **b**. compressed; **c**. fine structure of a single NVPC particle (cross-section indicated in yellow); **d**. summary of structural parameters acquired from XCT; **e**. the volume ratio of different components in a compressed NVPC/CNTF electrode; **f**. the thickness of compressed and uncompressed NVPC/CNTF electrodes with different areal loadings and conventional electrodes (current collector included); The schematics of sodium ion transportation in the pores of **g**. conventional electrodes and **h**. co-ESP electrodes;

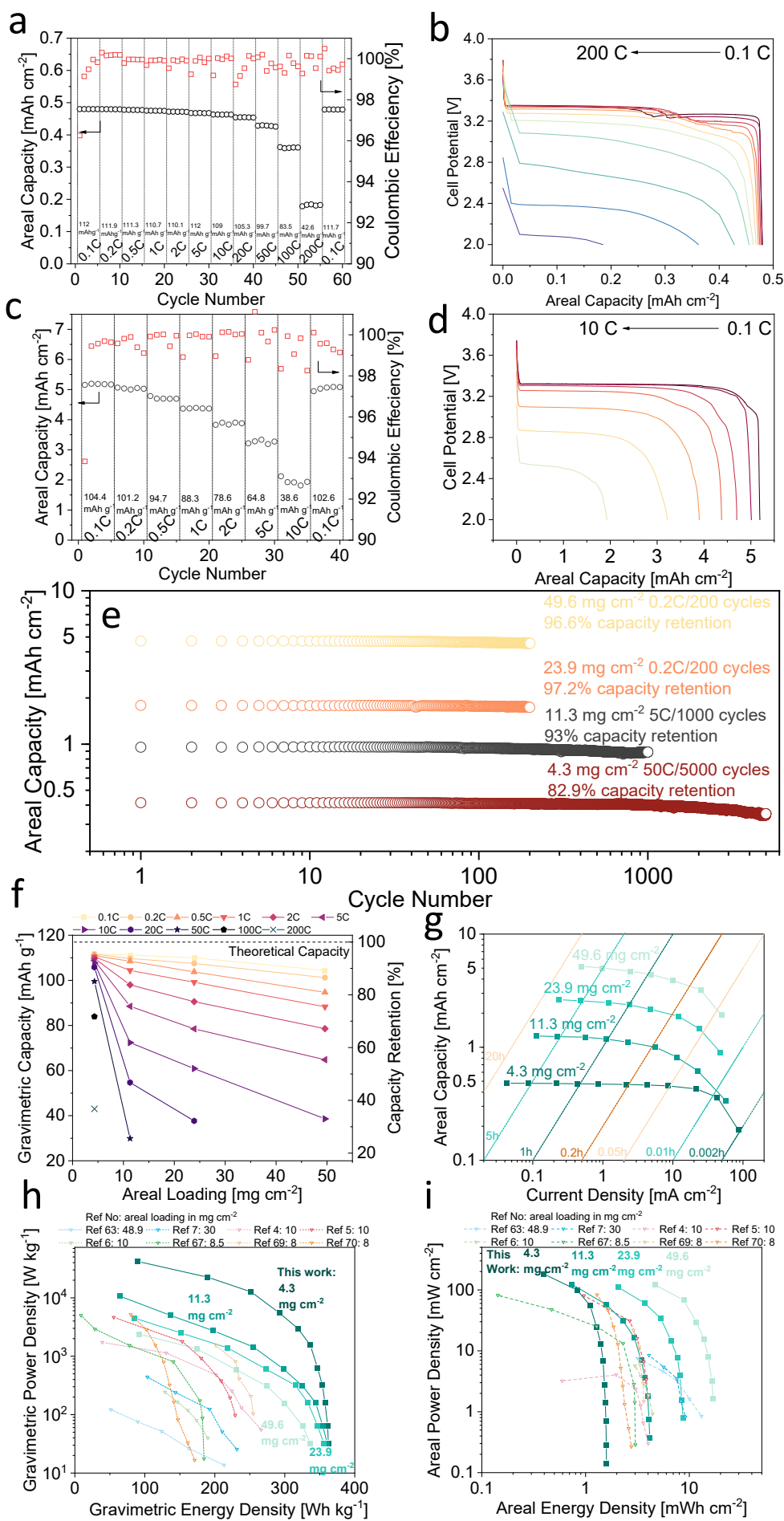


Figure 4. The performance of co-ESP NVPC cathodes with different areal loading: 4.3 mg cm⁻² cathode's **a.** rate performance and **b.** voltage profile; 49.6 mg cm⁻² cathode's **c.** rate performance and **d.** voltage profile; **e.** Cycling stability of different areal loading half cells; **f.** the change of specific discharge capacity with areal loading and cycling rate; **g.** The change of areal capacity with areal current; Ragone plots of **h.** gravimetric energy density versus power density and **i.** areal energy density versus areal power density, including the data acquired from previous sodium-ion battery half cells for comparison.

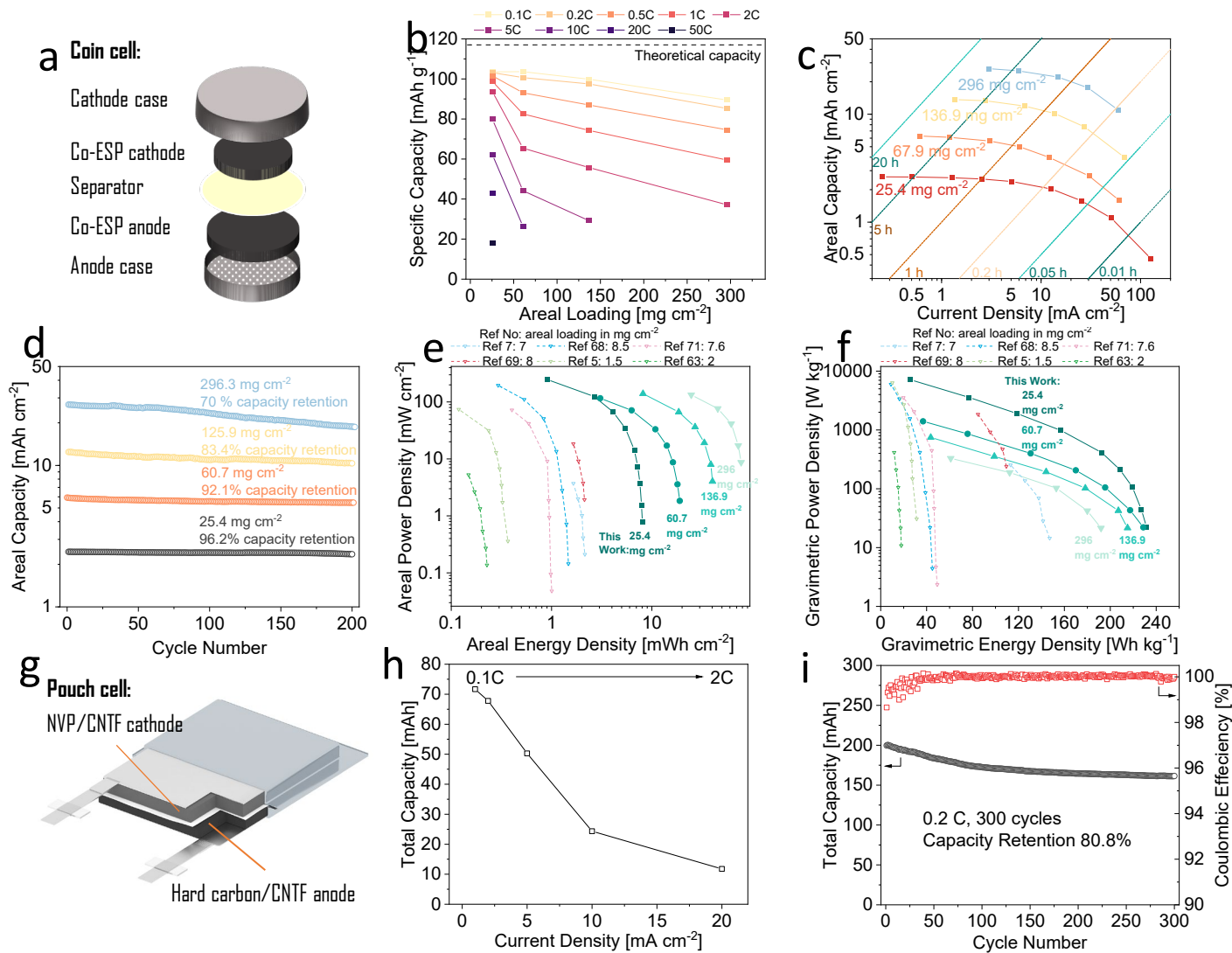


Figure 5 The performance of sodium ion batteries full cells and pouch cells made of co-ESP NVPC cathodes and co-ESP HC anodes: a. Schematic diagram of a sodium-ion battery full cell; **b.** the change of specific discharge capacity with areal loading and cycling rate; **c.** The change of areal capacity with areal current; **d.** Cycling stability of different areal loading full cells; Ragone plots of **e.** gravimetric energy density versus power density and **f.** areal energy density versus areal power density, including the data acquired from previous sodium-ion battery full cells for comparison; pouch cell performance with 100 mg cm^{-2} cathode loading: **g.** Schematic diagram of a sodium-ion battery pouch cell; **h.** Rate performance and **i.** Cycling performance of 0.2 Ah, 100 mg cm^{-2} cathode loading pouch cell.

Supplementary Appendix 1: Figures

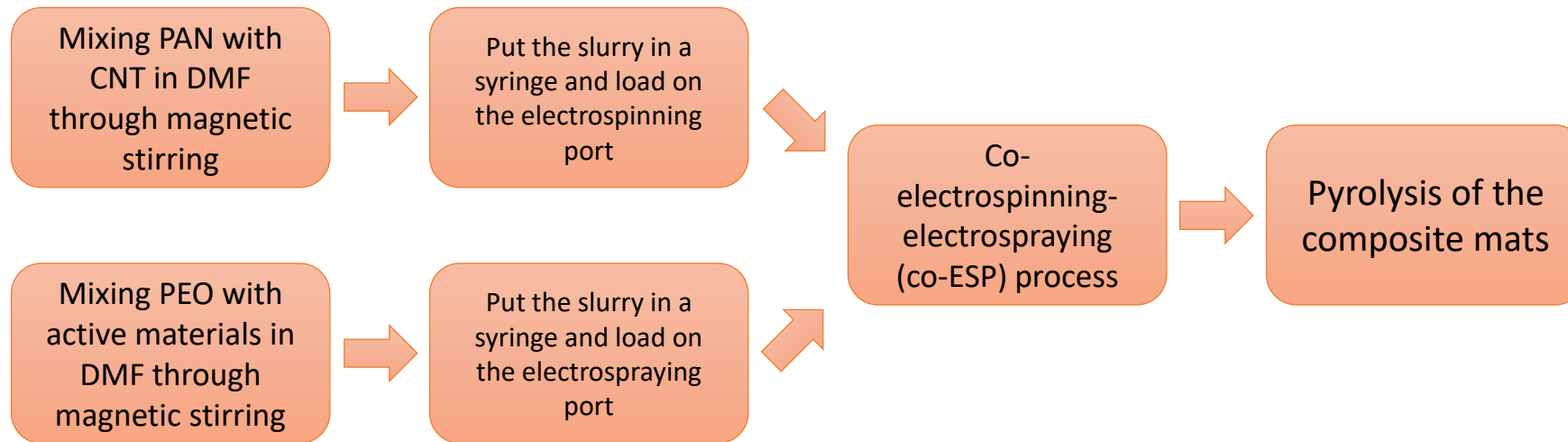


Figure S1 Flow chart showing the process of fabricating co-ESP electrode

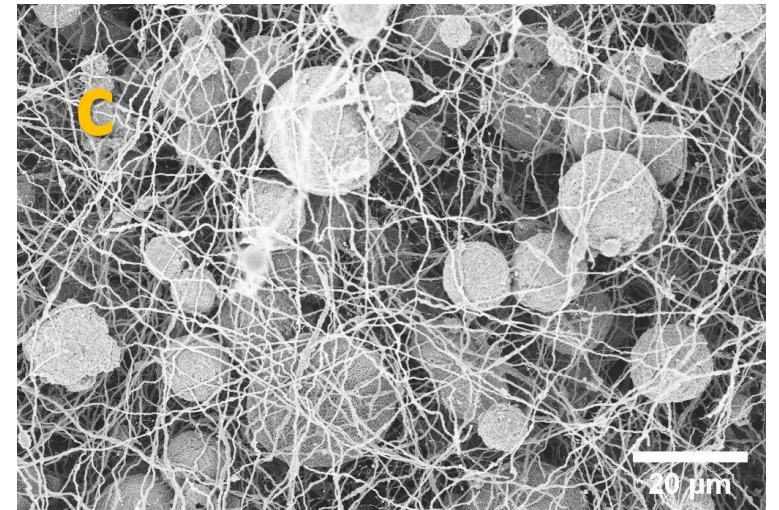
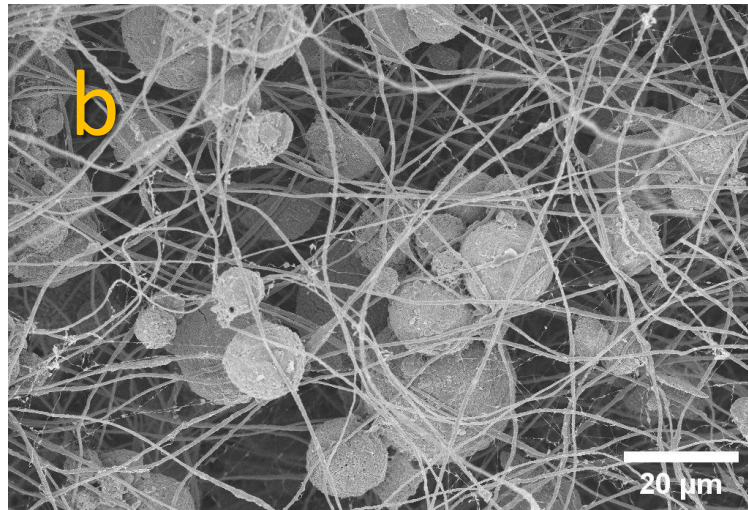
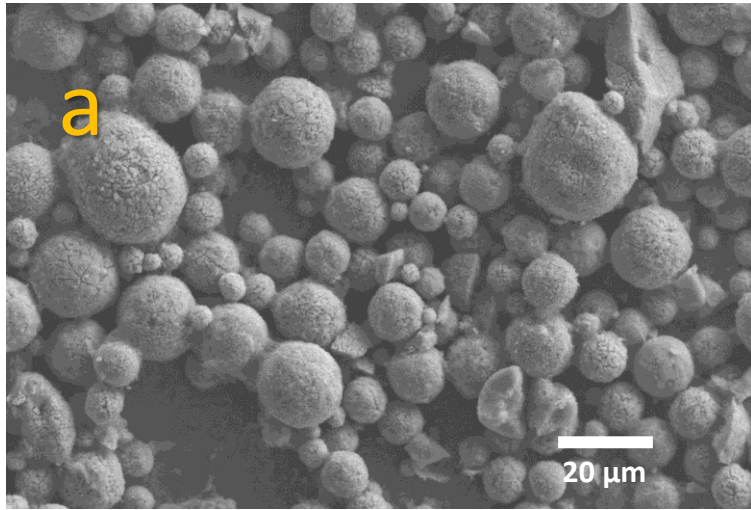


Figure S2 Morphology of a. Pristine NVPC particles; b. NVPC-PEO/PAN-CNT composite mat, right after the co-ESP fabrication; c. NVPC/CNT-CNF electrode, after pyrolysis.

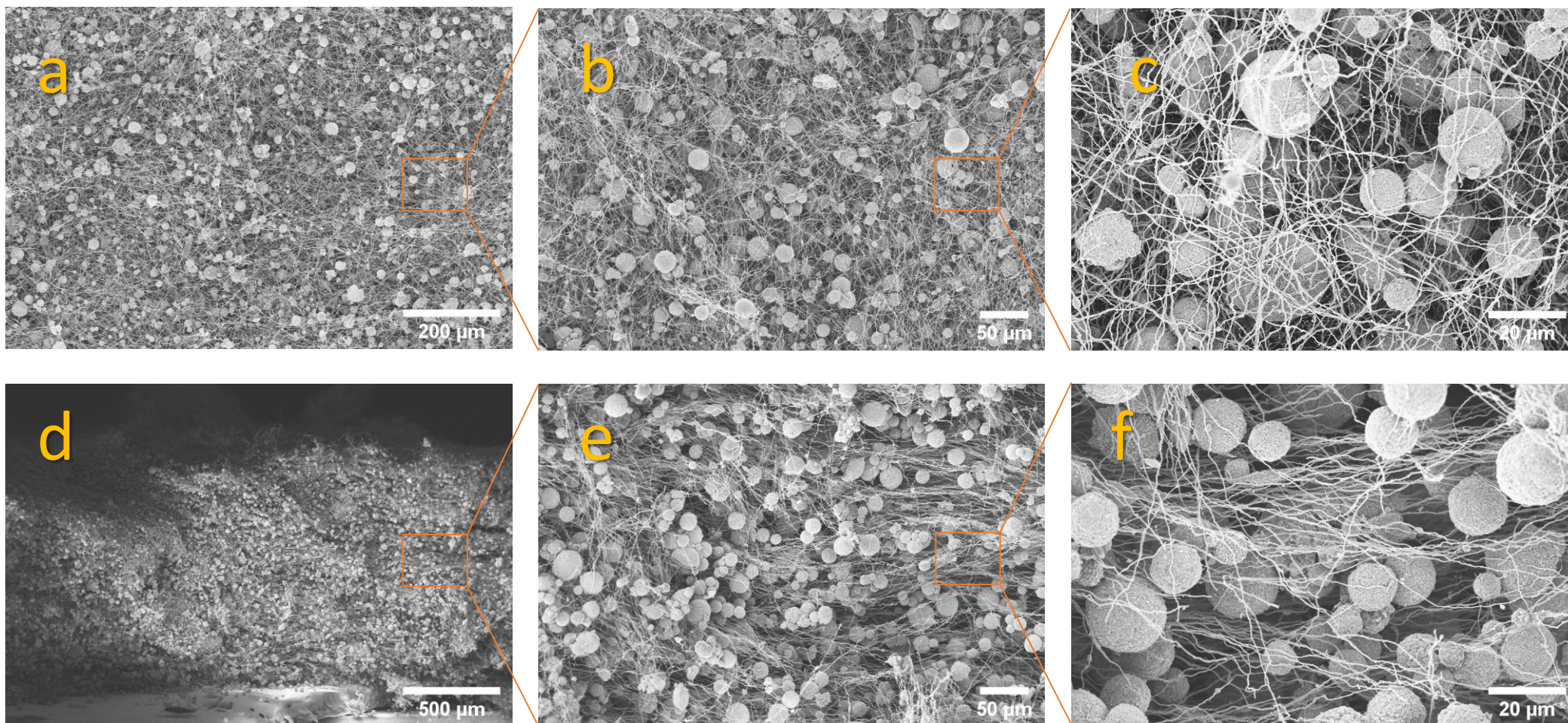


Figure S3 Morphology of 97.5% NVPC/CNTF from **a-c.** top view and **d-f.** cross view of different magnifications

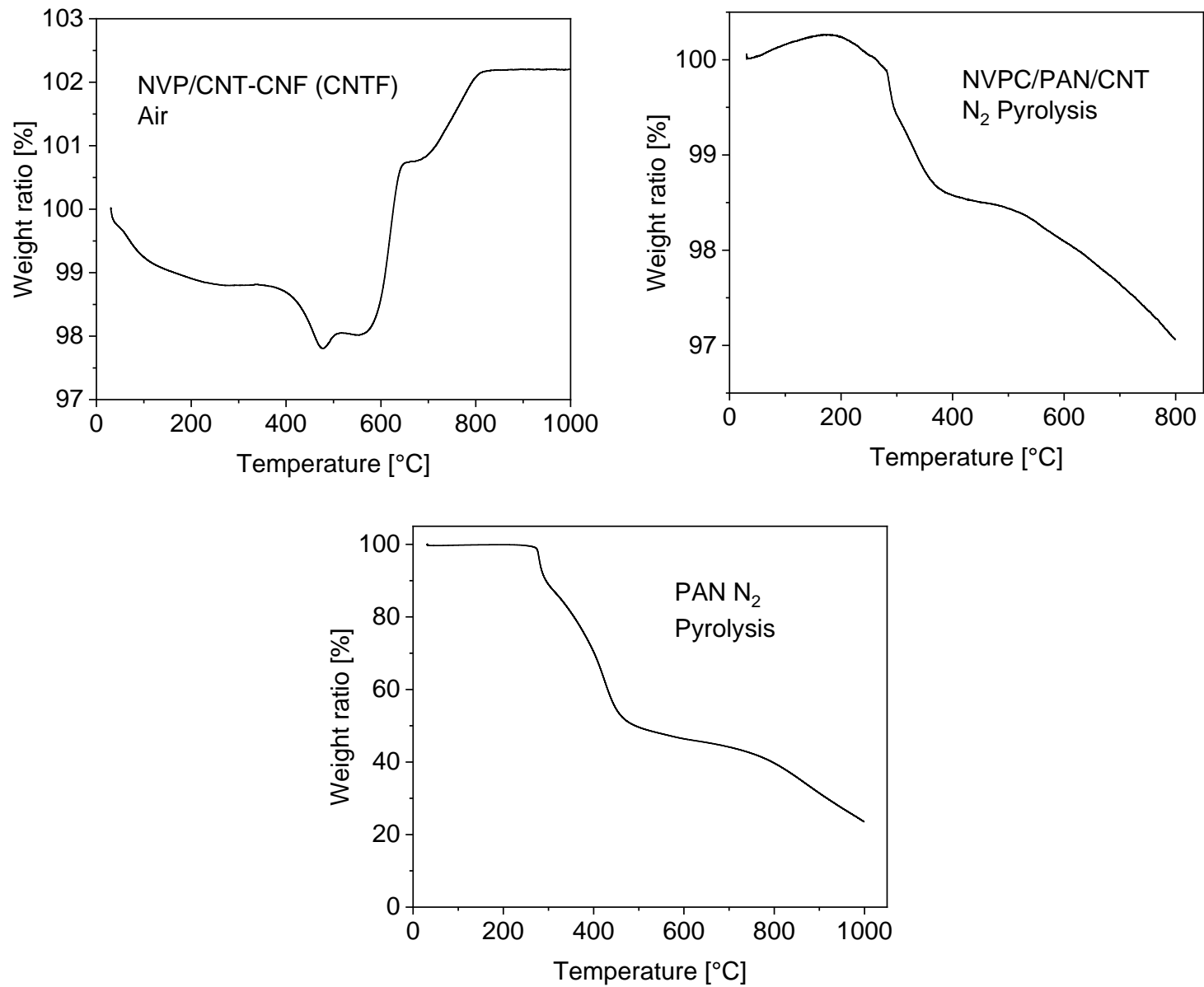


Figure S4 TGA of NVPC/CNTF in air, NVPC/PAN-CNT right after co-ESP fabrication in N₂ and pure PAN fibres in N₂

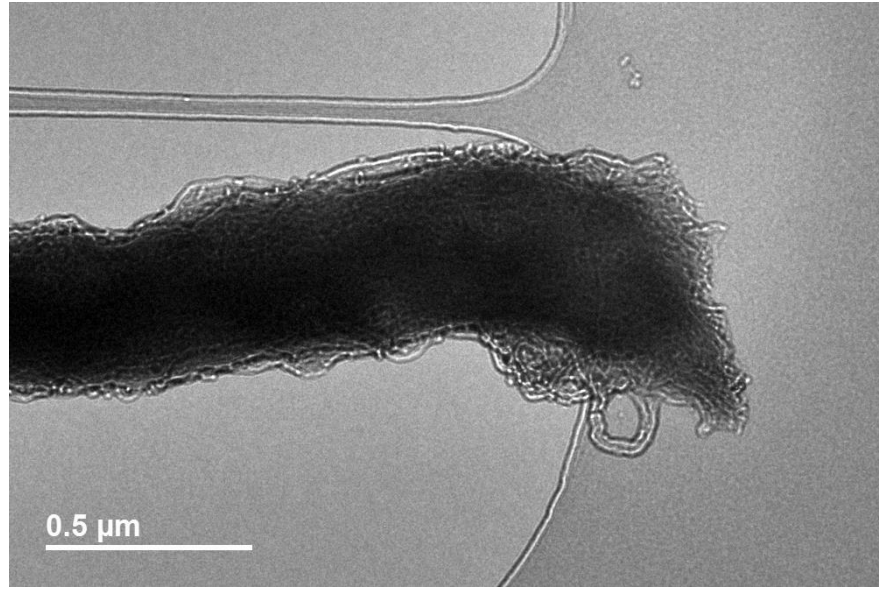
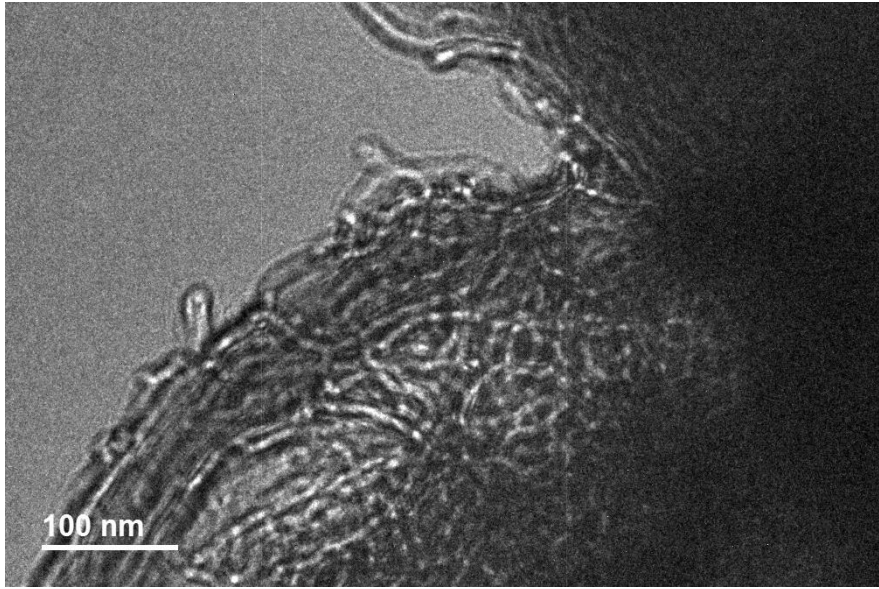


Figure S5 TEM of carbon nanotube embedded carbon fibre (CNTF)

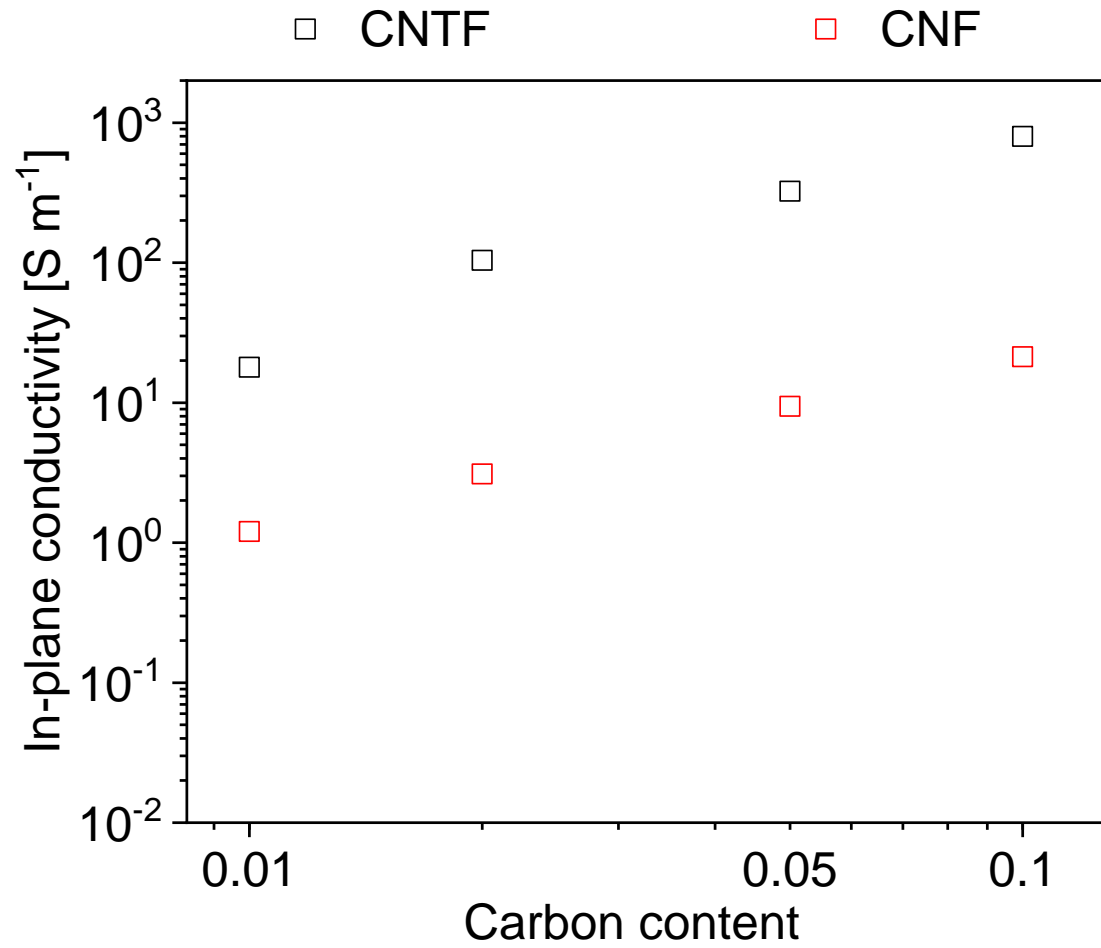


Figure S6 In-plane conductivity of PAN-derived CNF network and CNT embedded CNF (CNTF) network

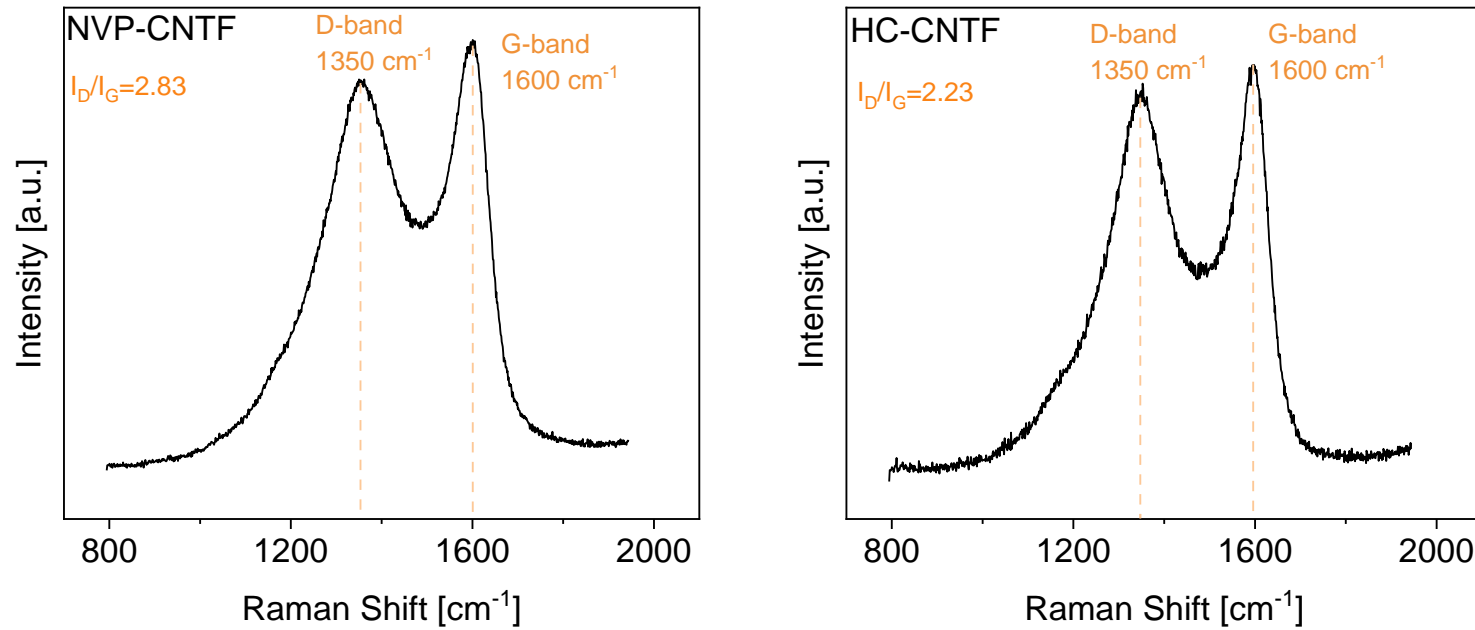


Figure S7 Raman spectrum of co-ESP NVPC/CNTF electrodes and HC/CNTF electrodes

The I_D/I_G value is inversely related to the degree of graphitisation of the carbon sample (Ferrari and Robertson 2000). The I_D/I_G values of NVPC-CNTF and HC-CNTF are 2.83 and 2.23, respectively. The lower I_D/I_G of the HC-CNTF is caused by its higher pyrolysis temperature (1100 vs. 850 °C). Both samples have lower I_D/I_G than previously reported PAN-derived carbon fibres pyrolyzed at same temperatures (Wang, Serrano et al. 2003). This is mainly due to the presence of CNT in the CNTF fibres (Bokobza and Zhang 2012).

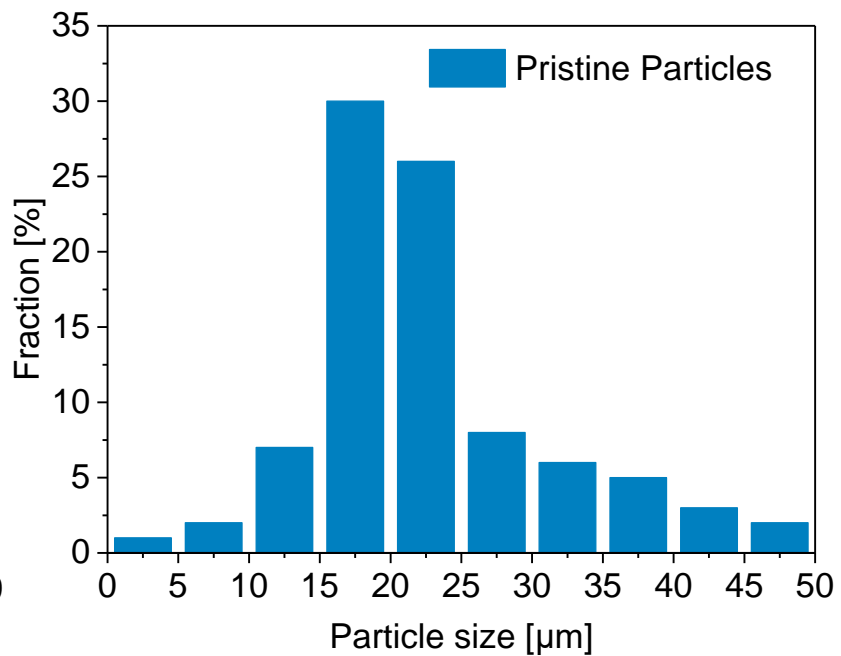
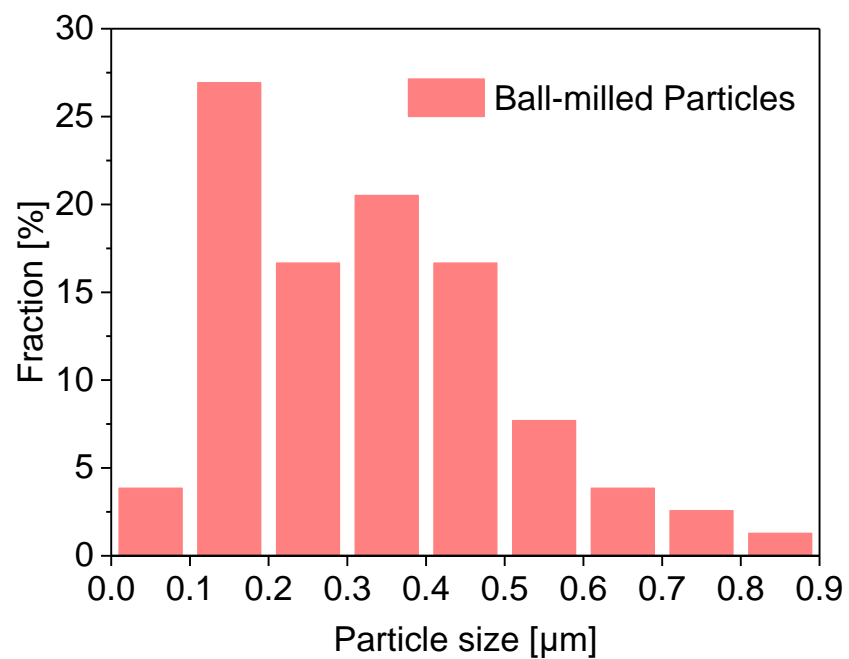


Figure S8 Particle size distribution of NVPC and ball-milled NVPC particles

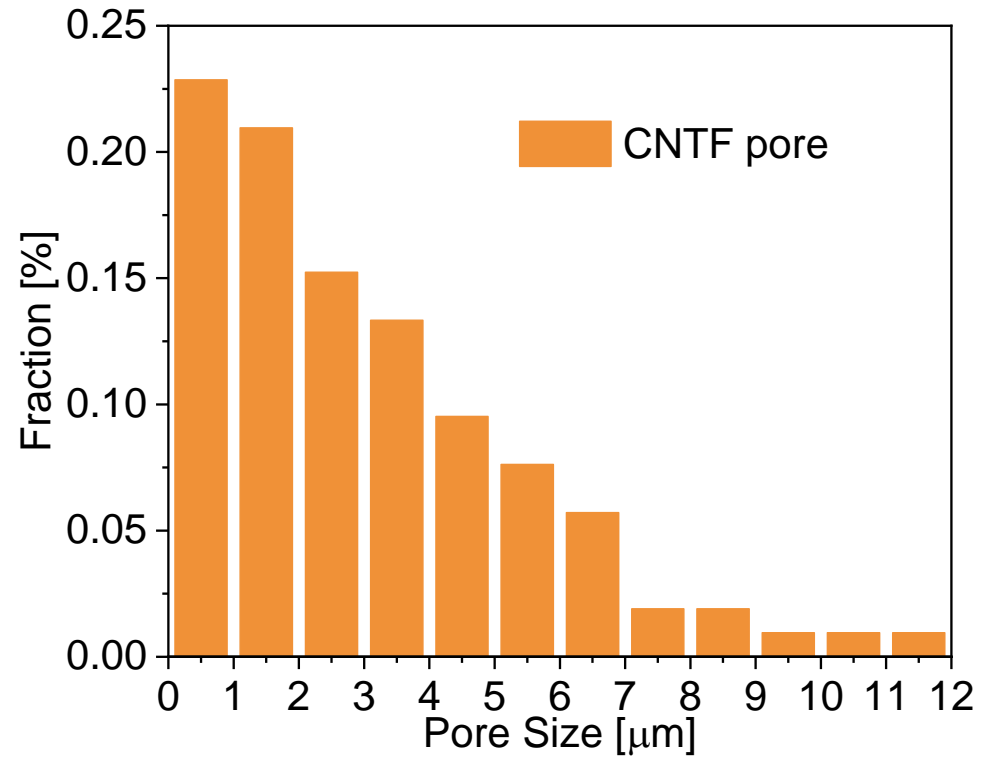


Figure S9 Pore size distribution of CNTF network

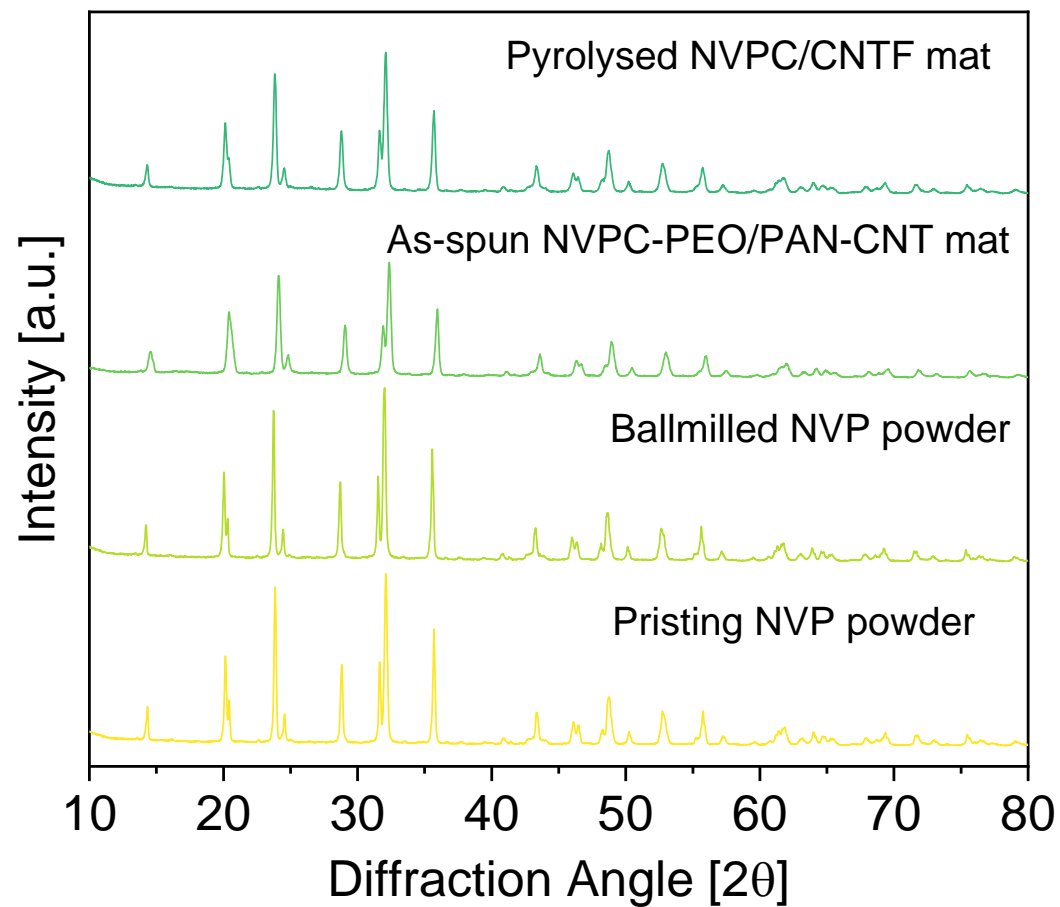


Figure S10 The X-ray diffraction (XRD) pattern of pristine and ball-milled NVPC particles and NVPC/CNTF electrode at different stages of preparation

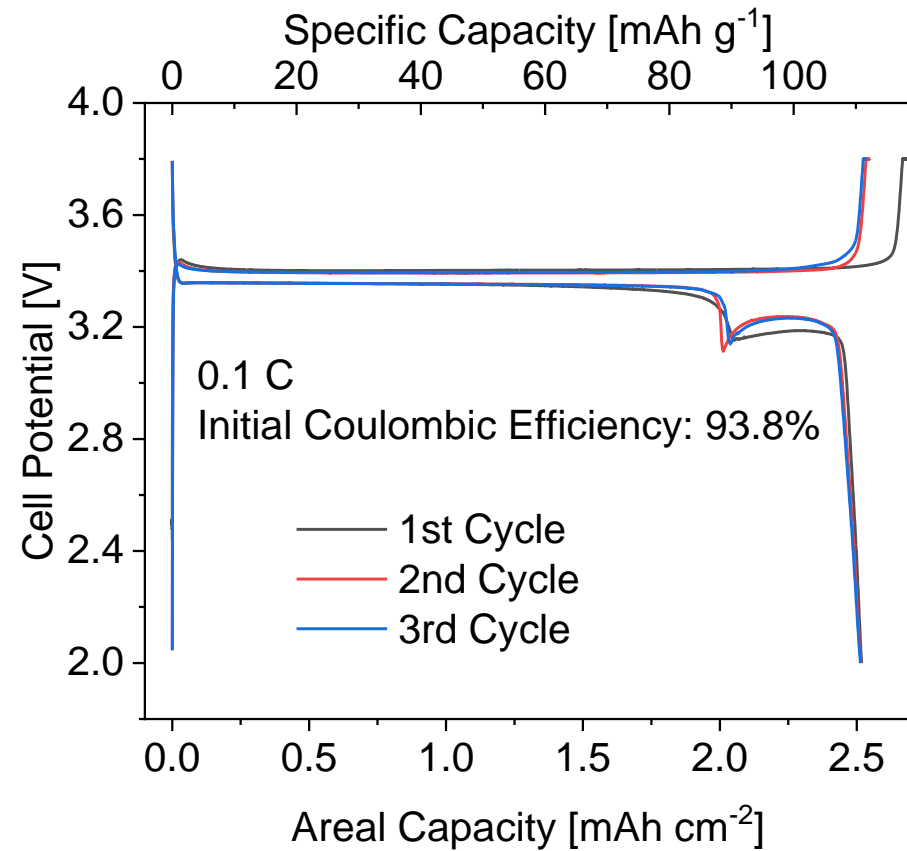
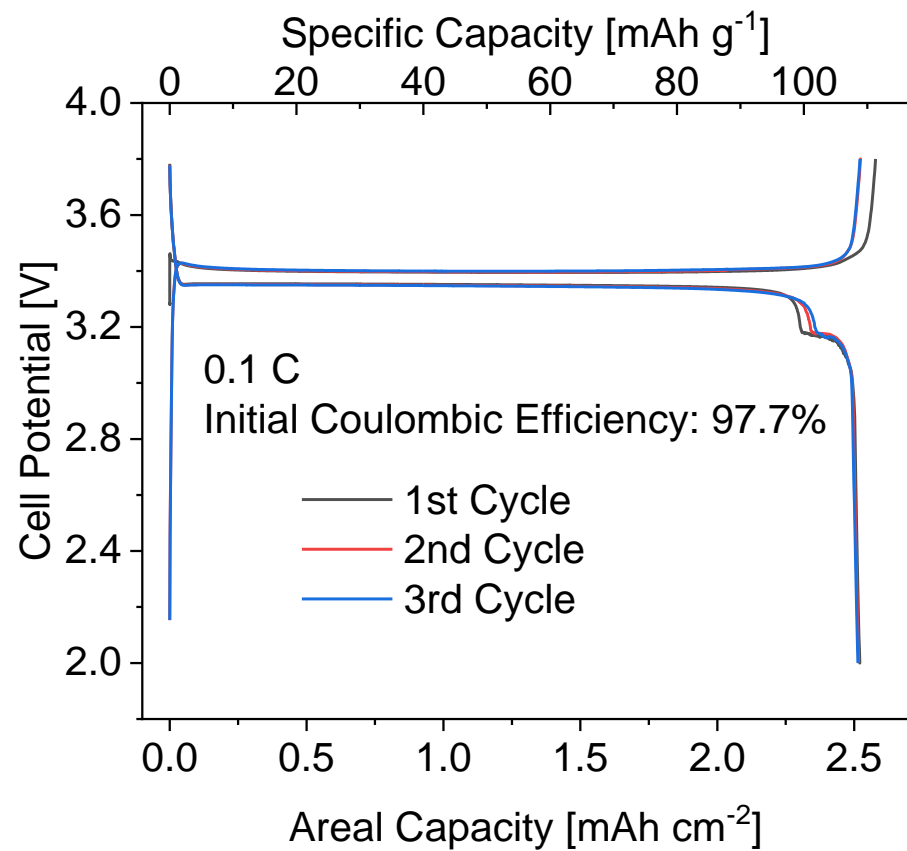


Figure S11 First three cycles of **a)** pristine and **b)** ball-milled NVPC/CNTF half cells

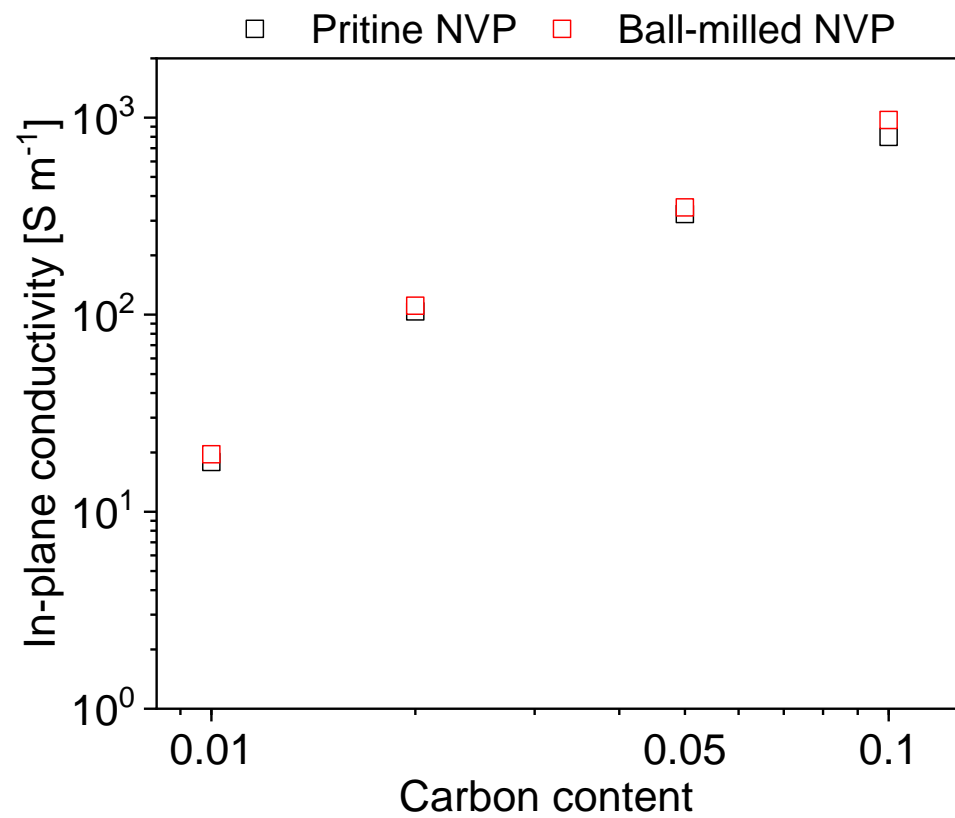


Figure S12 In-plane conductivity of co-ESP electrodes made by pristine NVPC and ball-milled NVPC

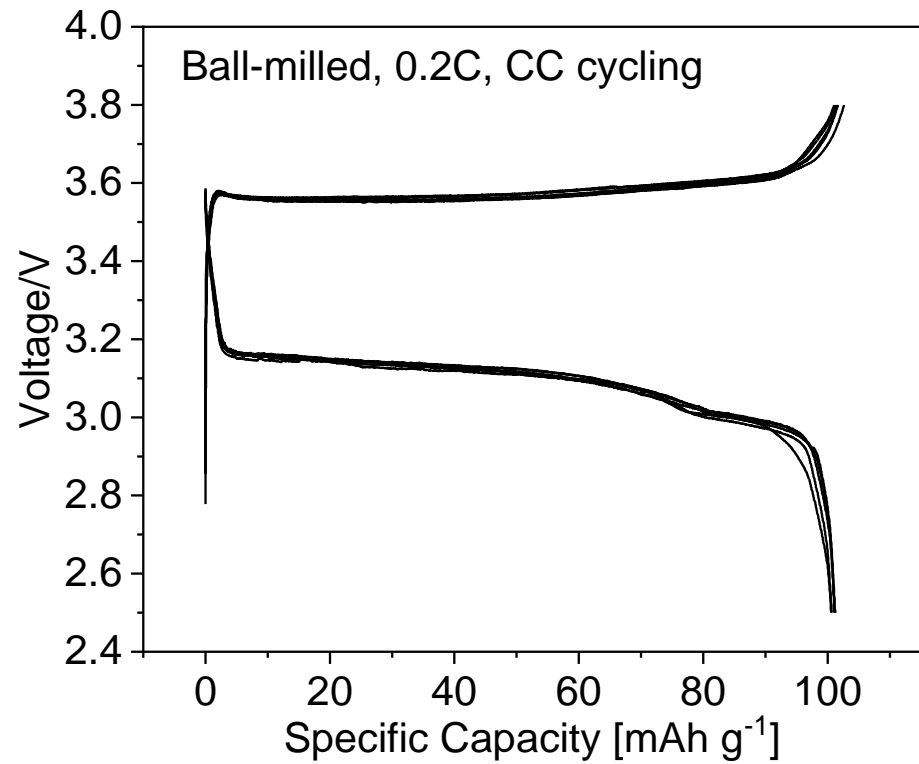
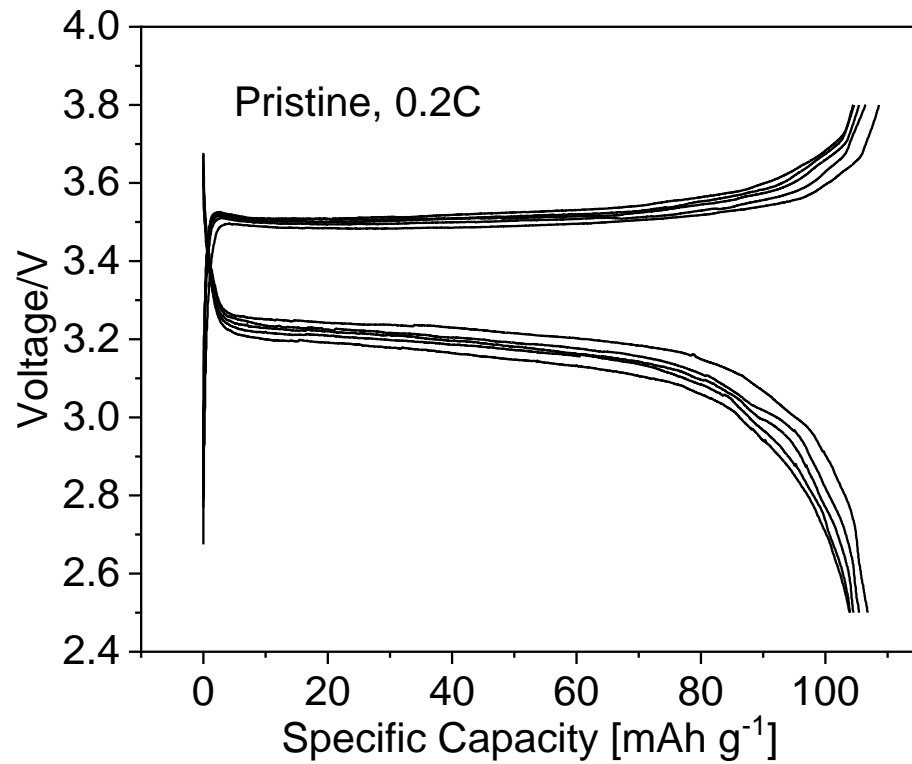


Figure S13 0.2C voltage profile of conventional slurry-casted electrode with pristine and ball-milled NVPC particles, CC cycling

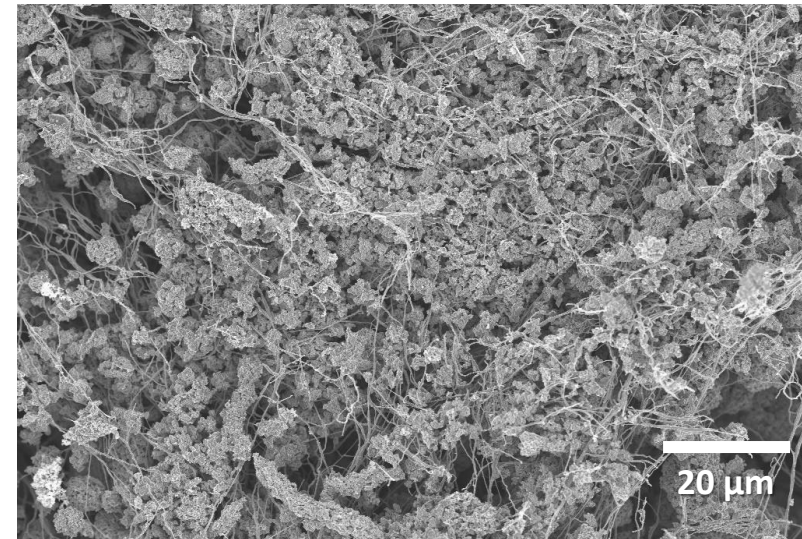
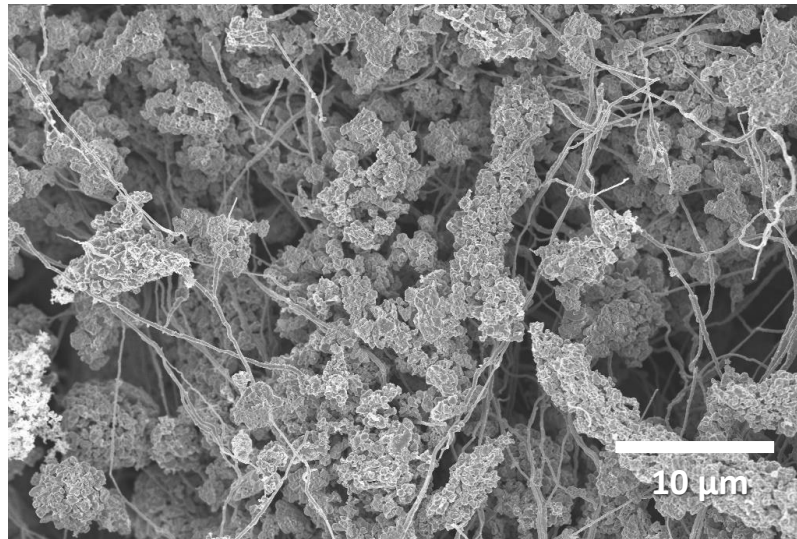
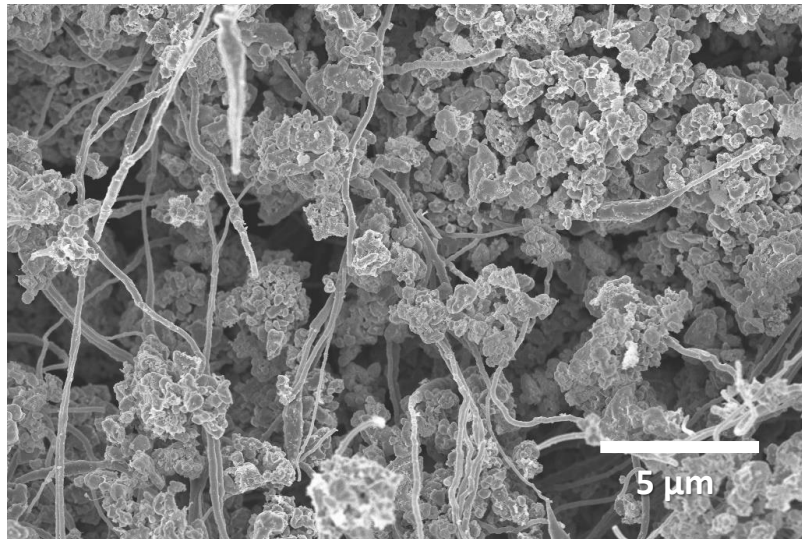
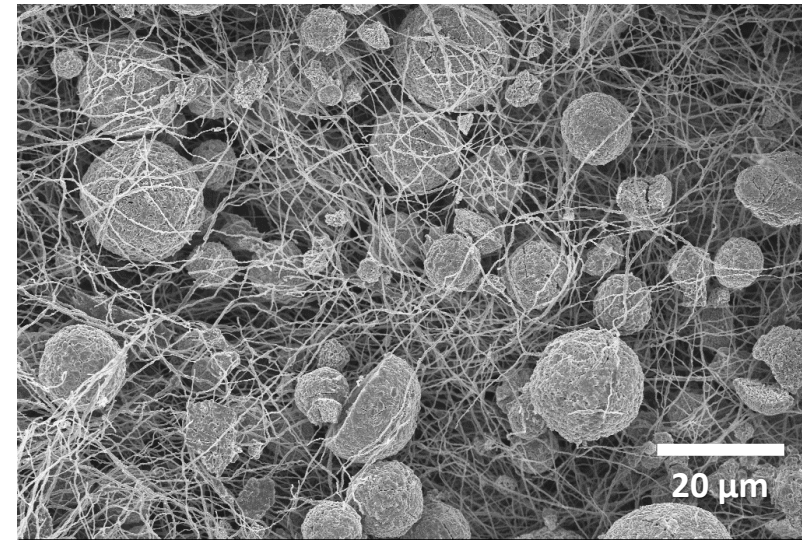
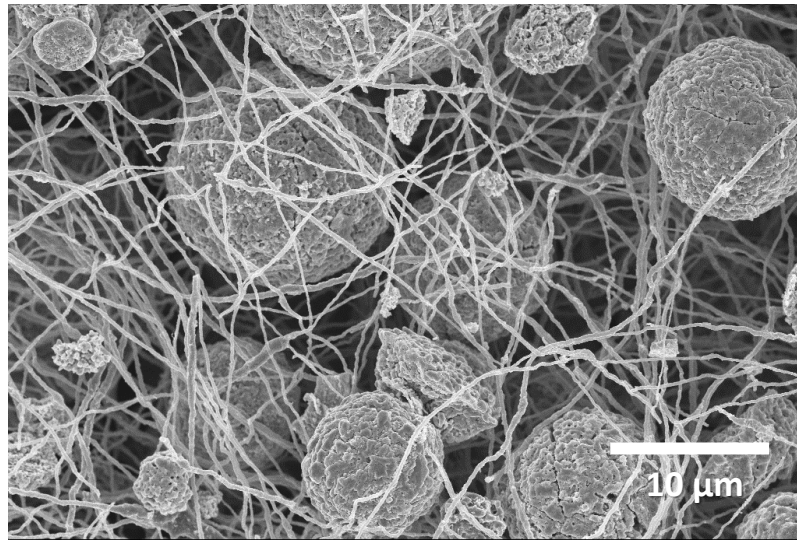
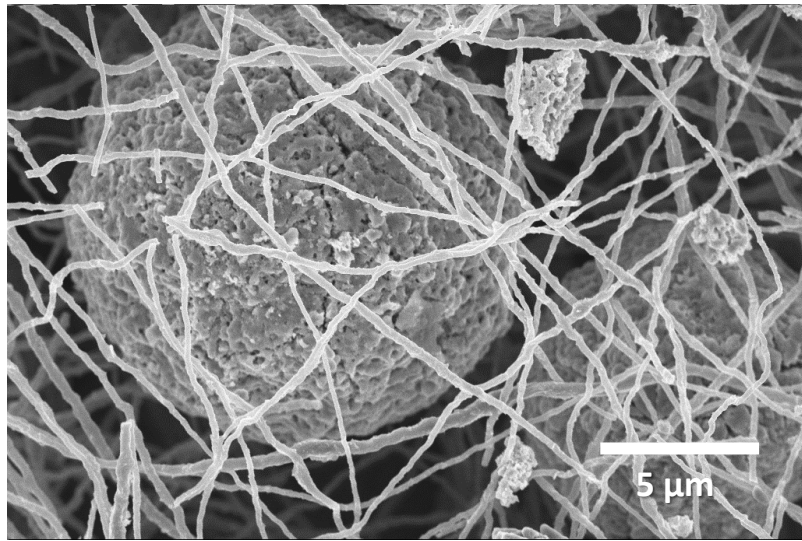


Figure S14 Photo/SEM images of co-ESP NVPC electrodes from **top**: pristine and **bottom**: ball-milled after 100 cycles (97.5wt% active content)

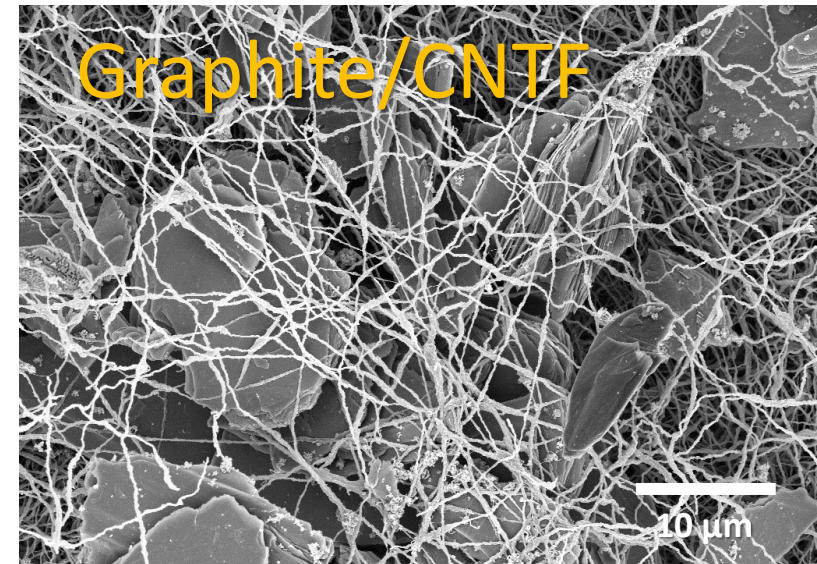
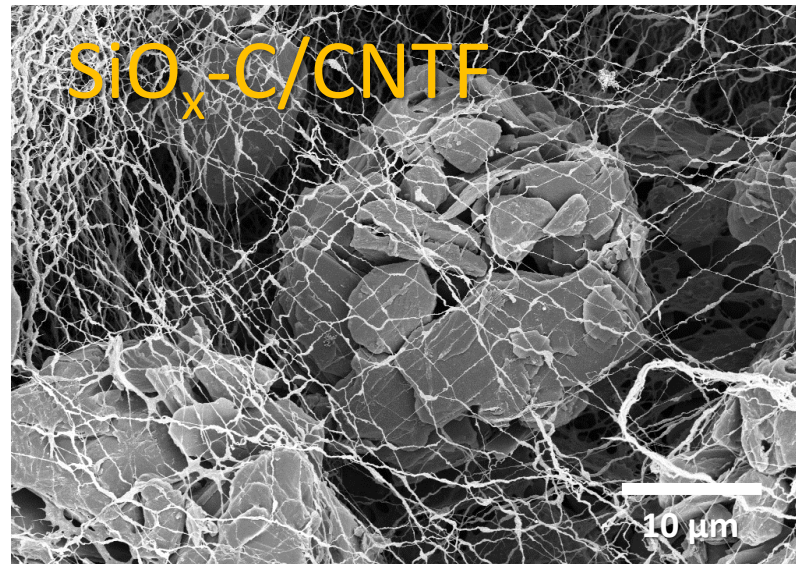
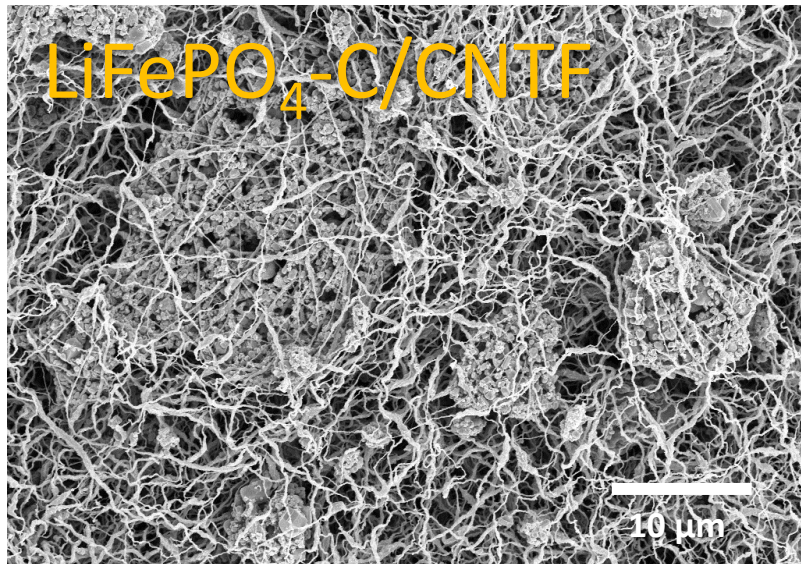
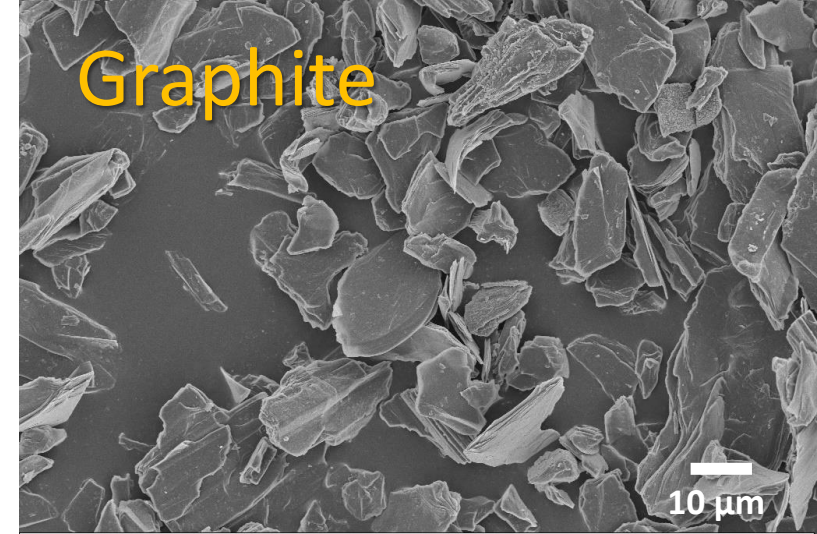
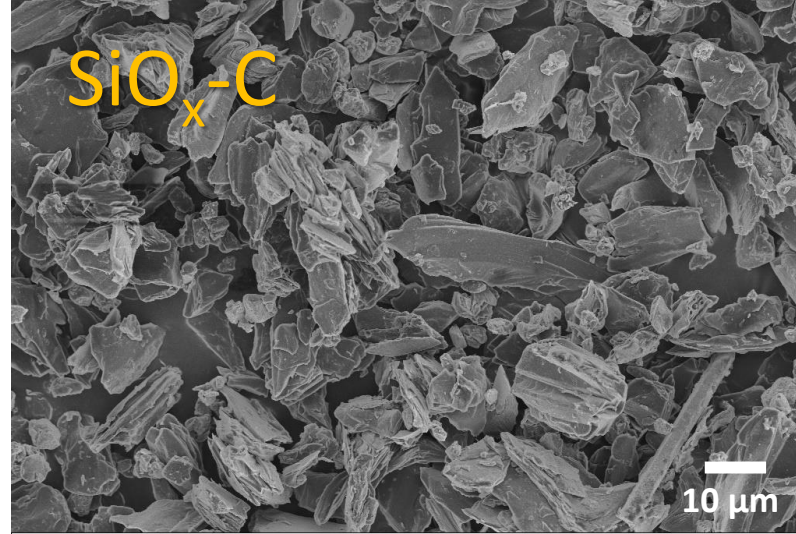
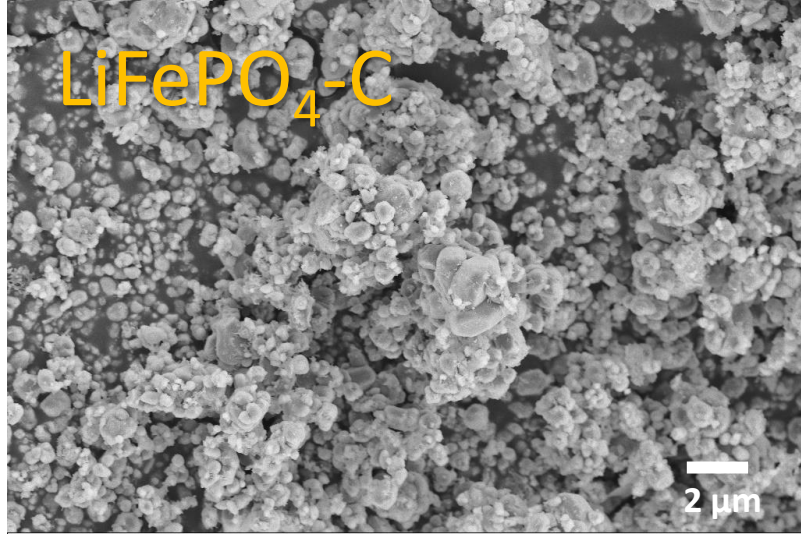


Figure S15 Morphologies of $\text{LiFePO}_4\text{-C}$, $\text{SiO}_x\text{-C}$ and graphite electrode produced by co-ESP method

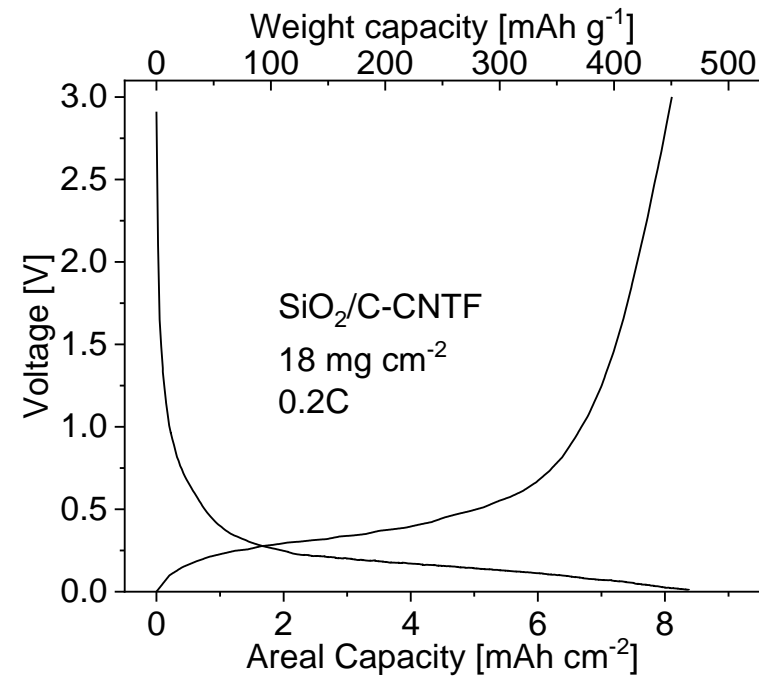
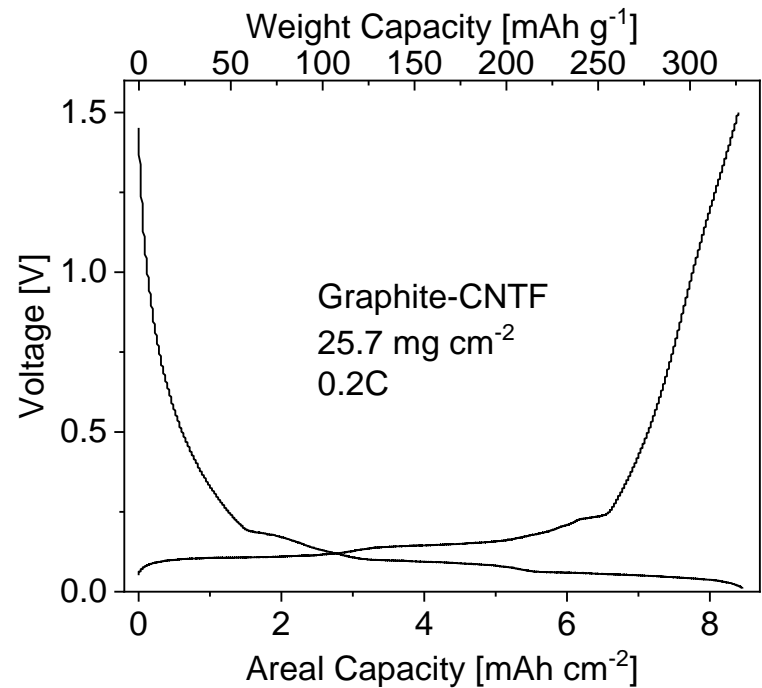
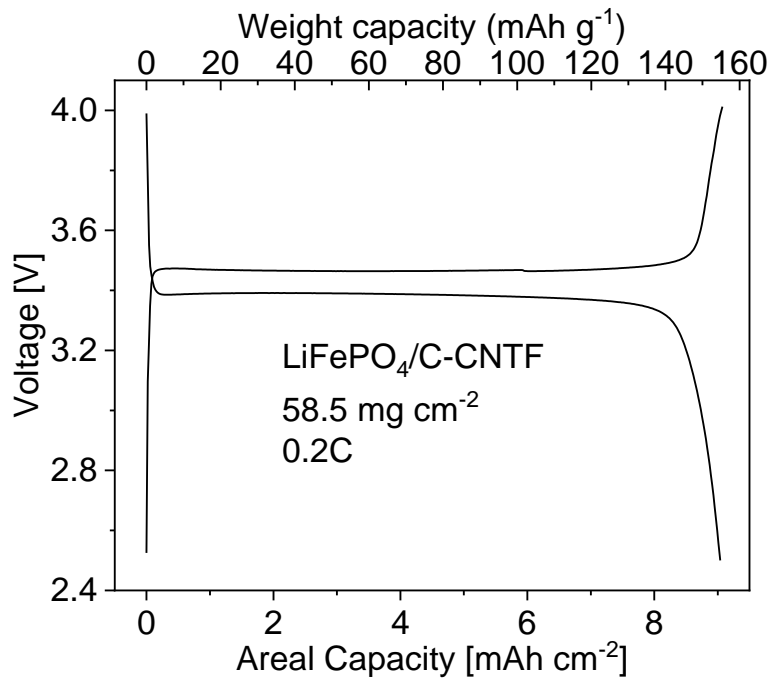


Figure S16 Voltage profiles of high areal loading LiFePO₄-C, graphite, and SiO_x-C electrode produced by co-ESP method

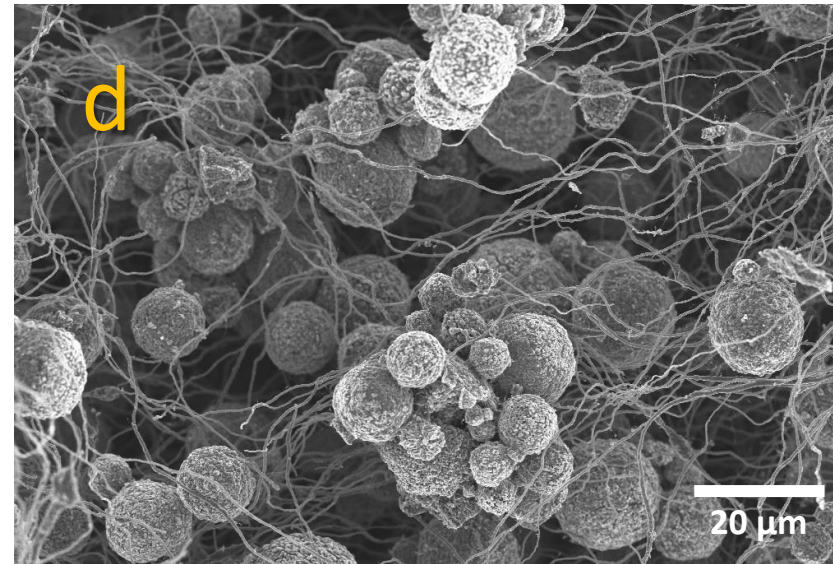
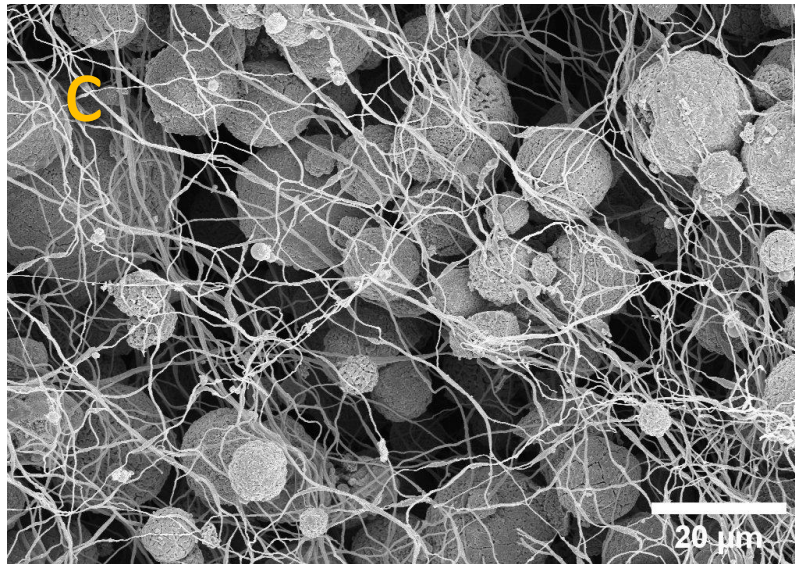
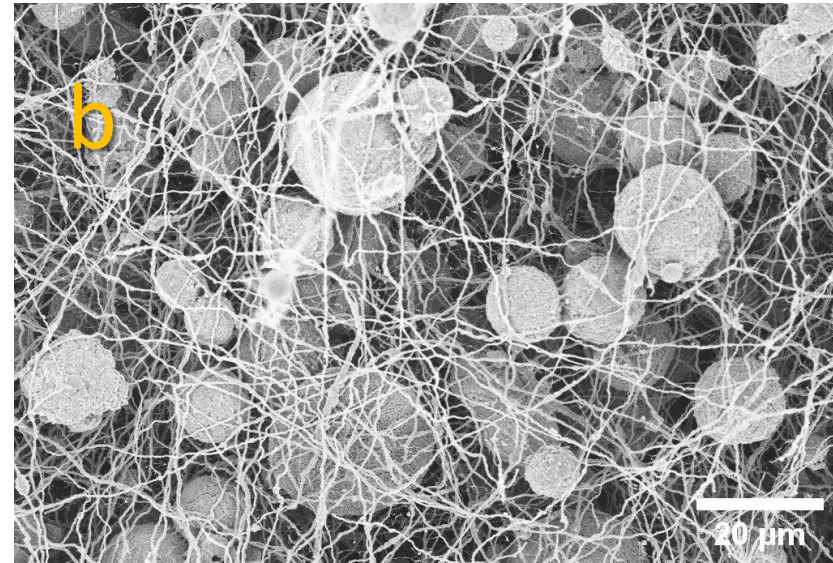
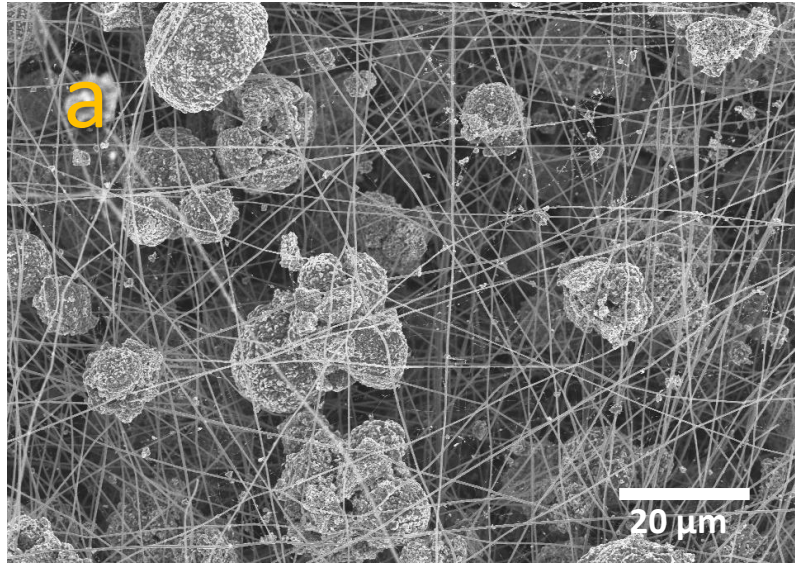


Figure S17 Morphology of NVPC/CNTF with a. 90 wt%; b. 97.5 wt%; c. 98 wt%; d. 99 wt% NVPC content

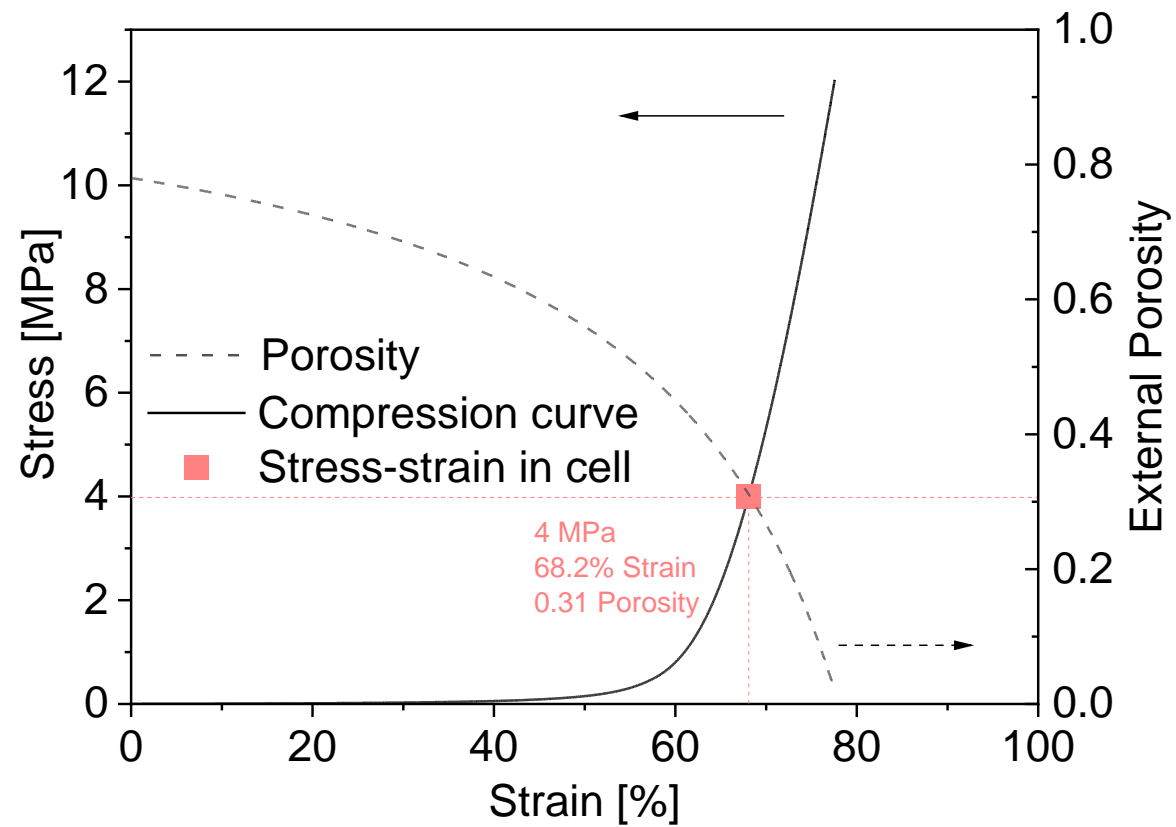


Figure S18 The relation of stress, strain and external porosity of the NVPC/CNTF electrodes

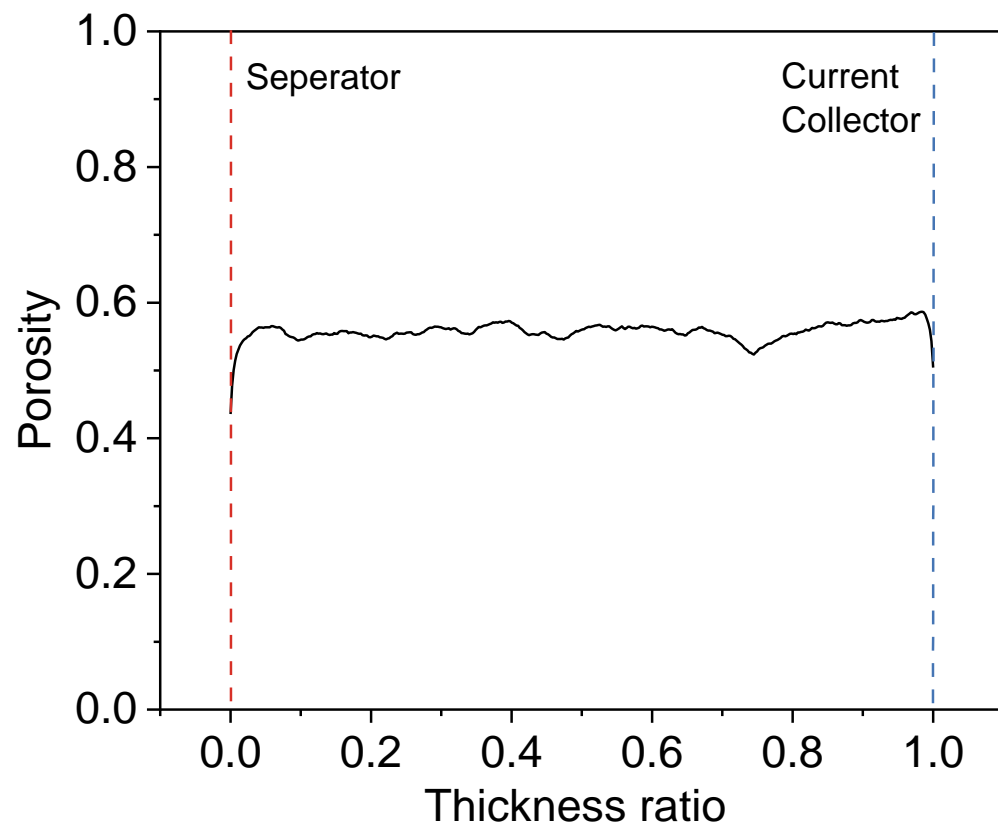


Figure S19 Uniformity of porosity across thickness

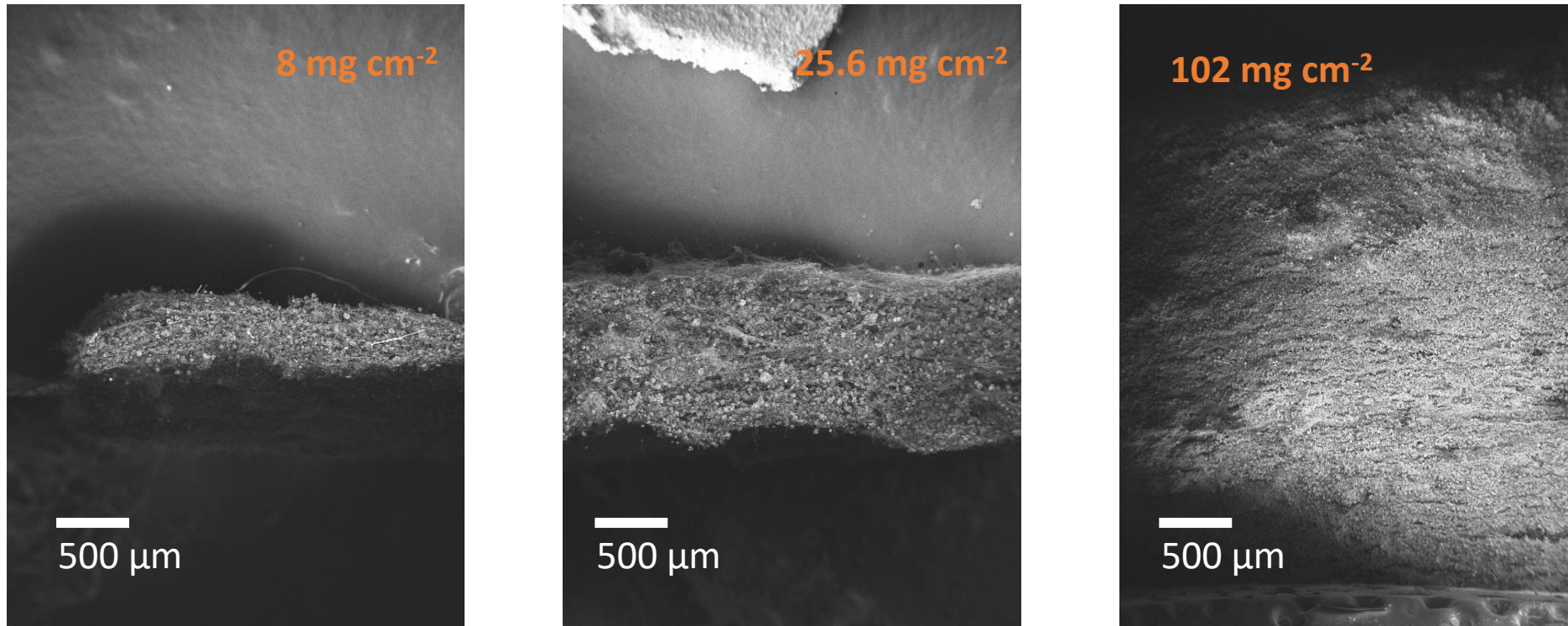


Figure S20 Cross-section morphologies of co-ESP NVPC/CNTF electrodes of different areal loadings, uncompressed. Left to right: 8 mg cm⁻², 25.6 mg cm⁻², 102 mg cm⁻²

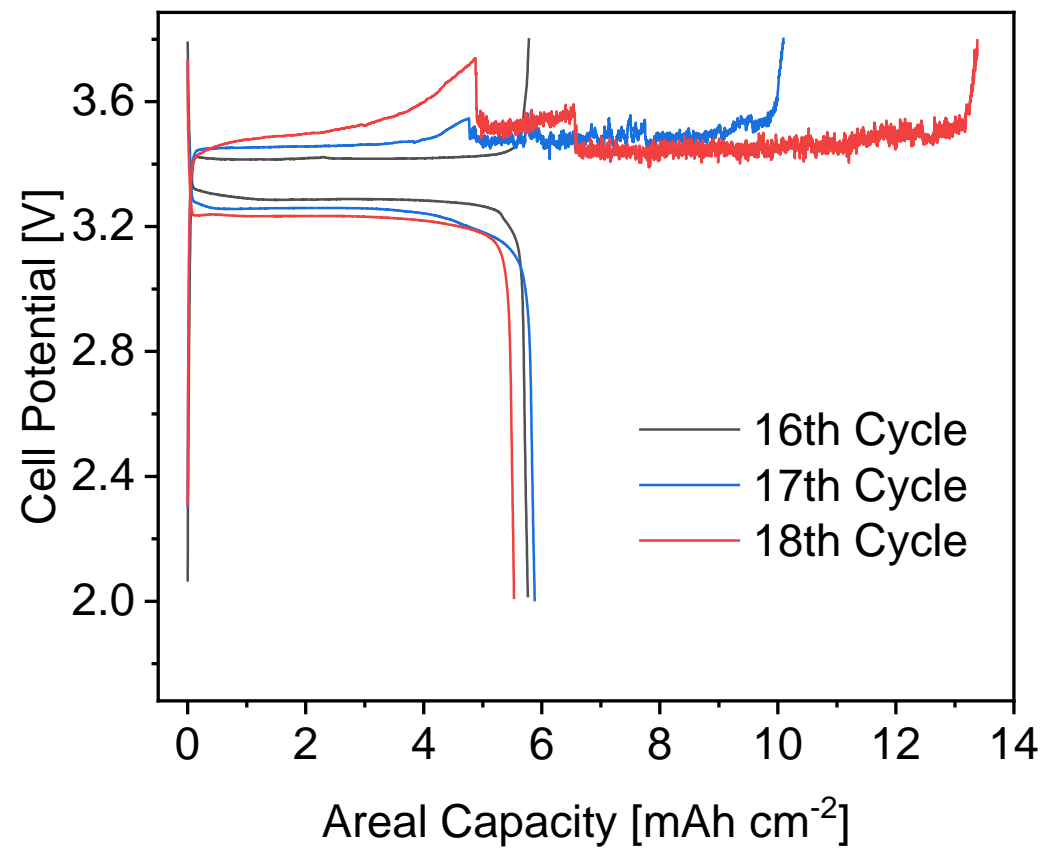


Figure S21 16-18th cycles of NVPC/CNTF half cells with FEC 56.7 mg cm⁻², the overcharging started from the 17th cycle in this cell even FEC is added in the electrolyte.



Figure S22 Sodium anode after overcharging in a NVPC/CNTF half-cell with 60.7 mg cm^{-2} areal loading, 20 cycles in total.

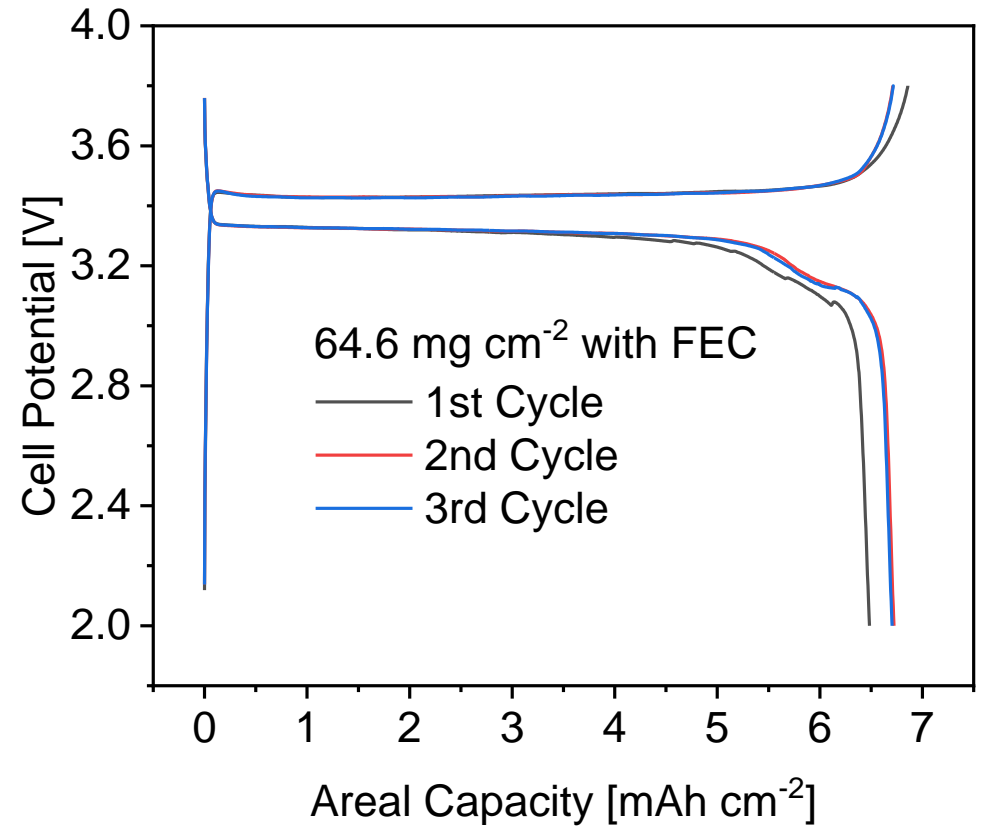
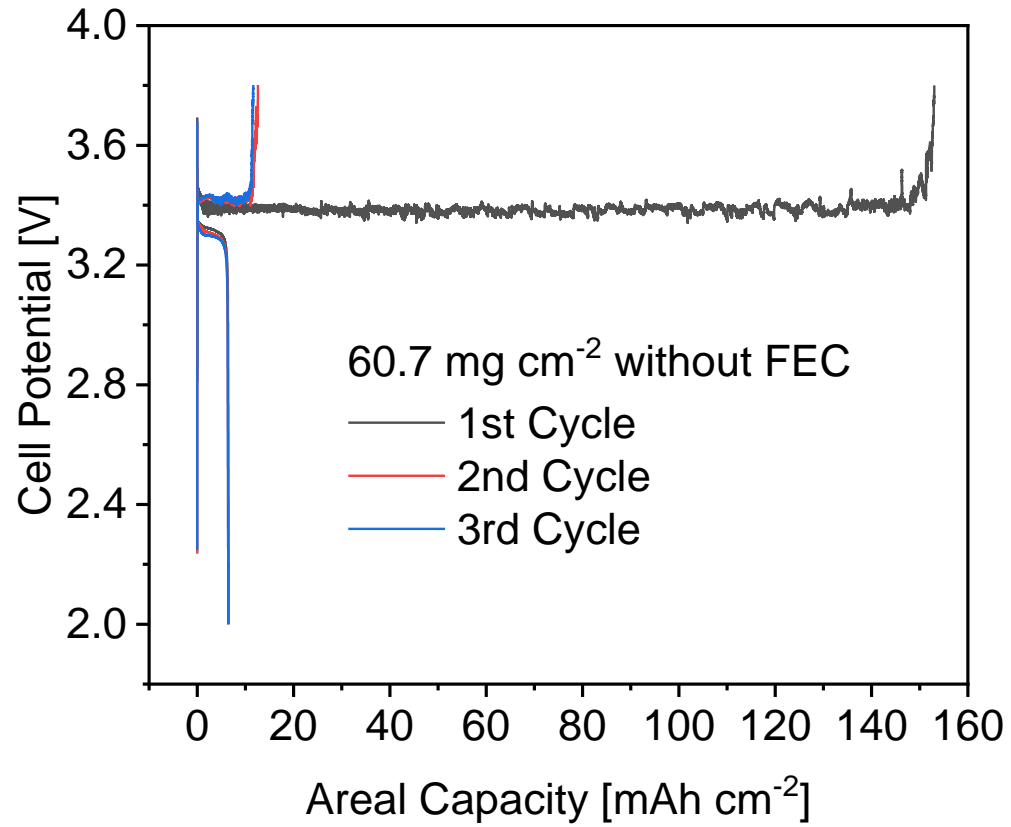
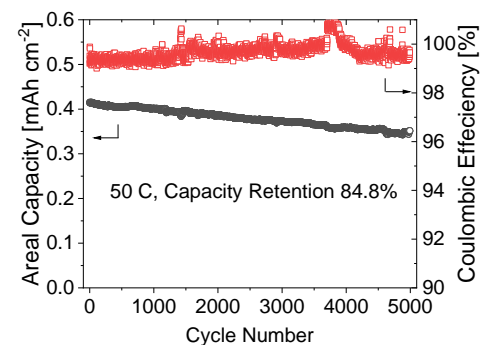
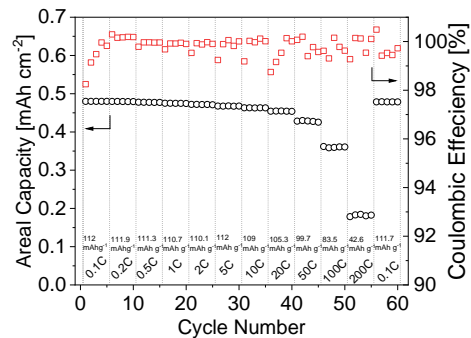
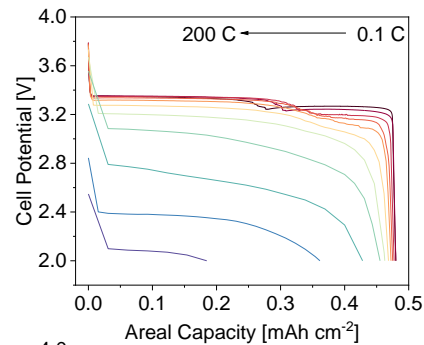
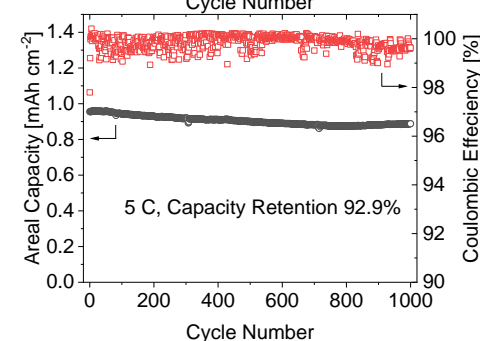
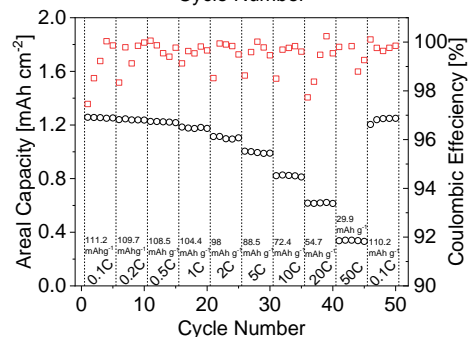
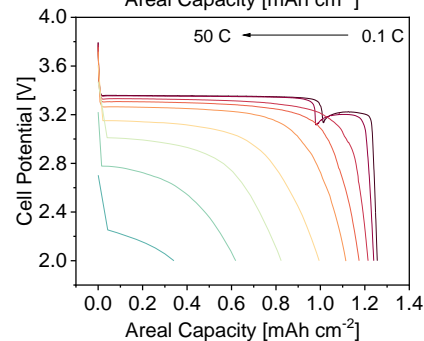


Figure S23 First three cycles of NVP/CNT-CNF half cells without FEC 60.7 mg cm⁻² or with FEC 64.6 mg cm⁻²

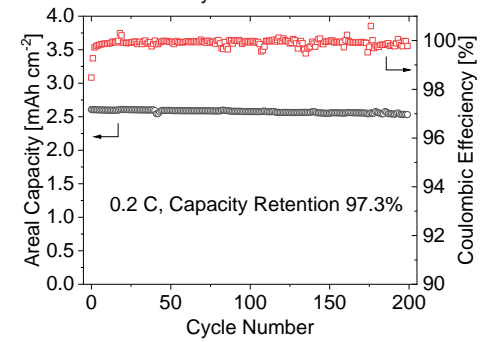
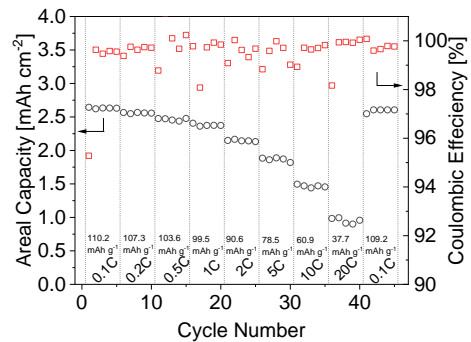
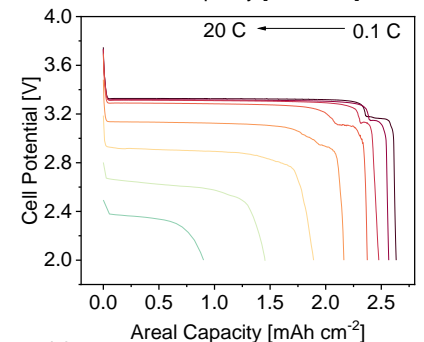
4.3 mg cm⁻²



11.3 mg cm⁻²



23.9 mg cm⁻²



49.6 mg cm⁻²

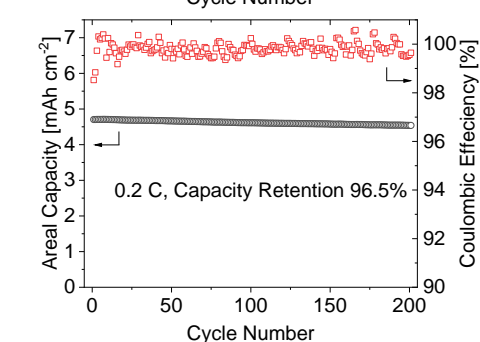
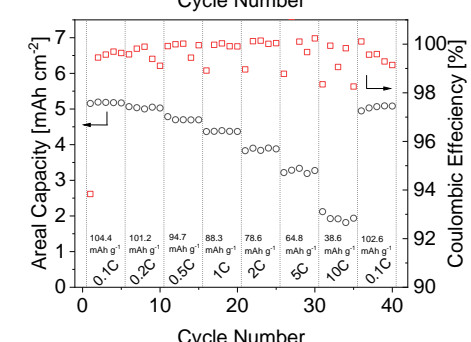
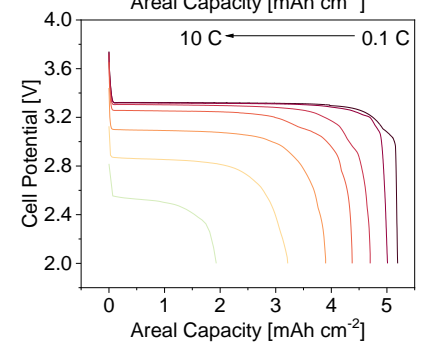


Figure S24 Cycling data of NVP/CNTF half cells of different areal loading

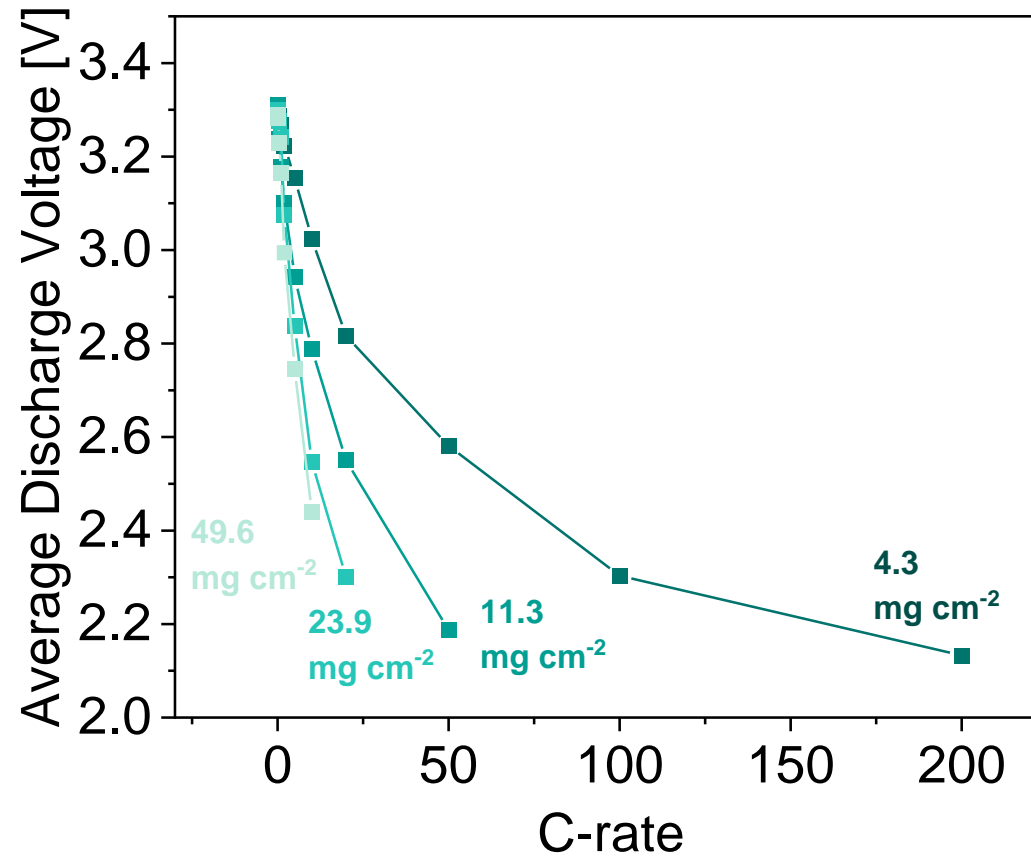


Figure S25 Average discharge voltage of co-ESP NVPC half-cells of different areal loading and C-rate

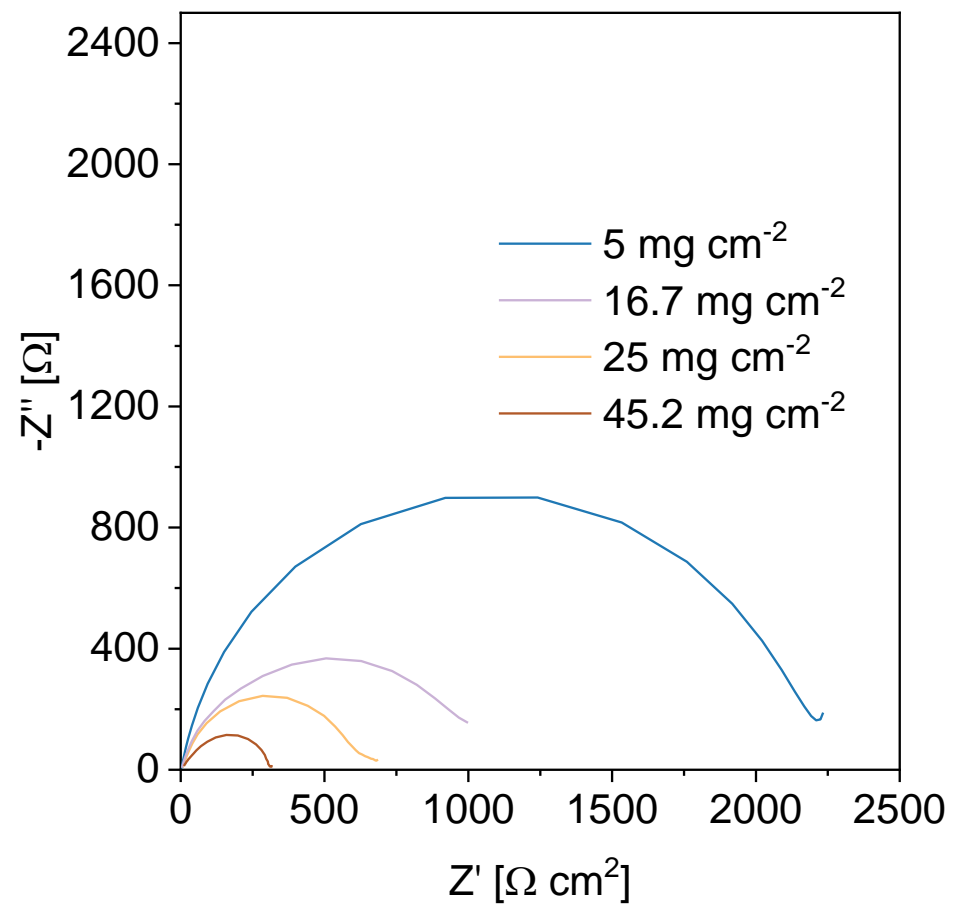


Figure S26 Nyquist of NVP/CNTF half cell of different loading, 0% state of charge

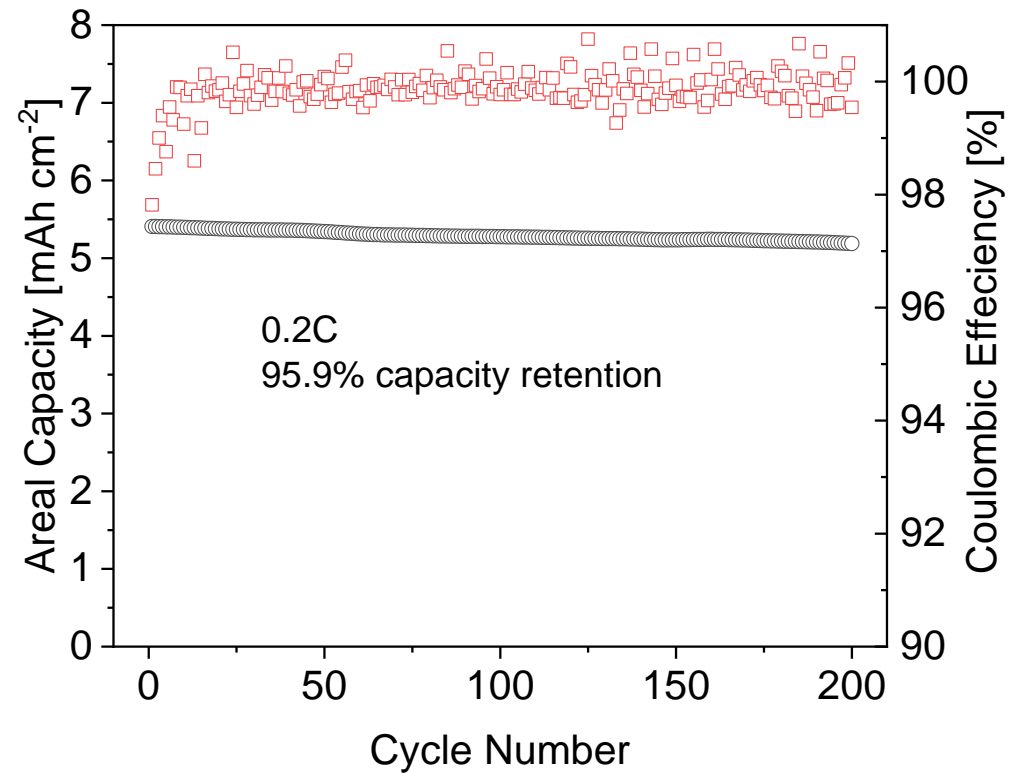
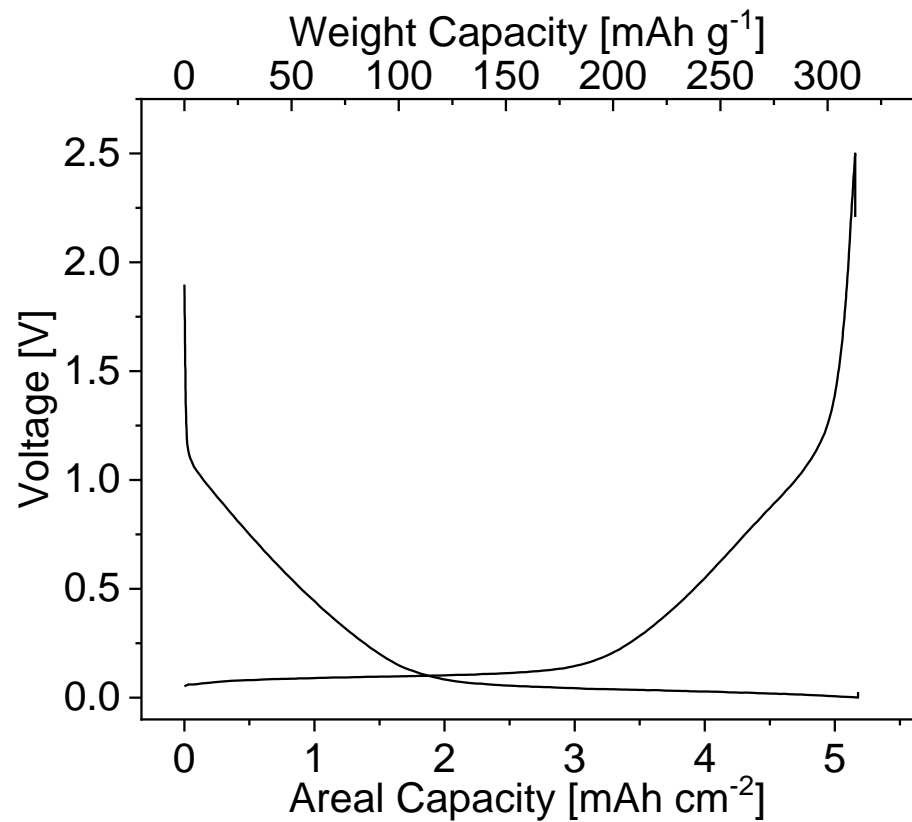


Figure S27 Voltage profile (left) and cycling stability (right) of glucose-derived hard carbon half cells, areal loading 16.5 mg cm⁻², 0.2C

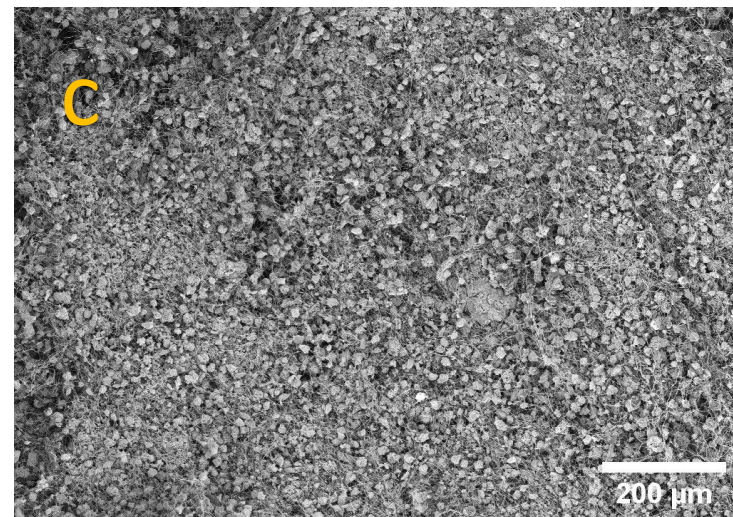
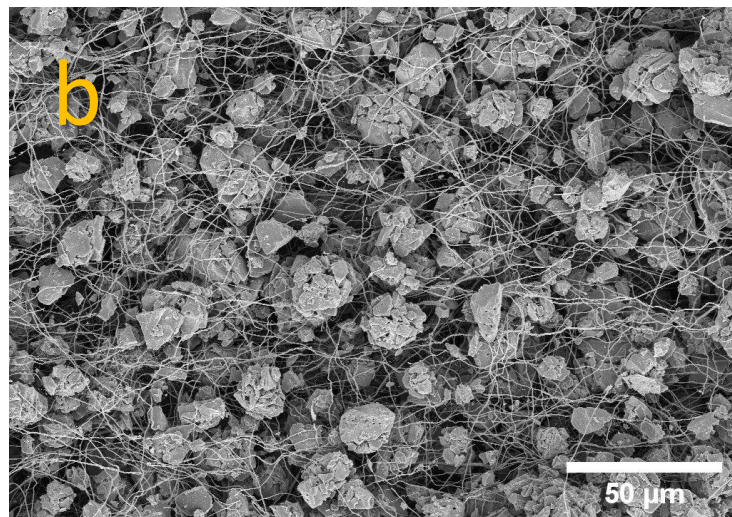
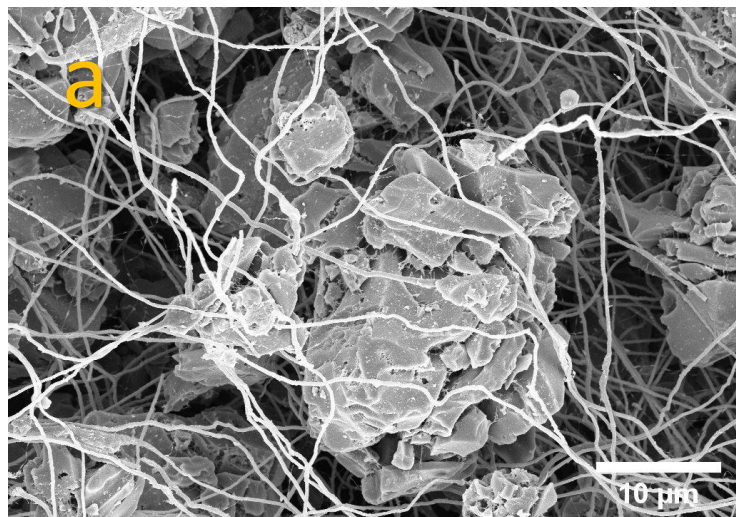


Figure S28 Morphology of co-ESP hard carbon/CNTF electrodes

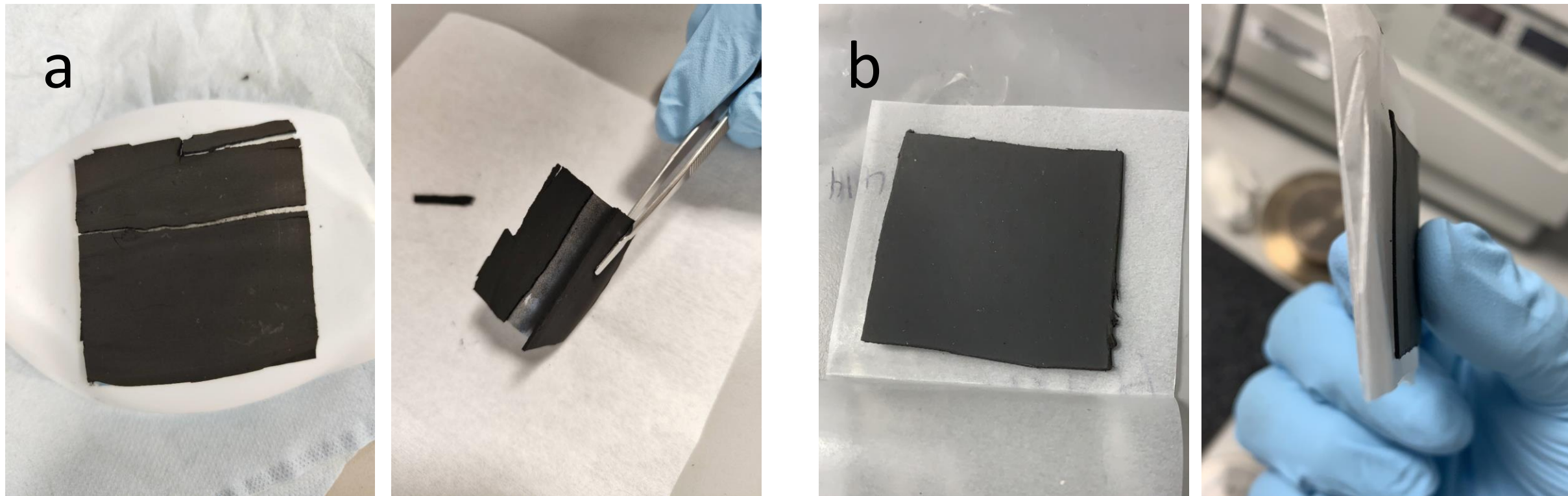


Figure S29 Photos of **a.** cracked and delaminated conventional NVPC electrodes with 80 mg cm^{-2} areal loading; **b.** compressed 100 mg cm^{-2} co-ESP NVPC/CNTF pouch cell electrode

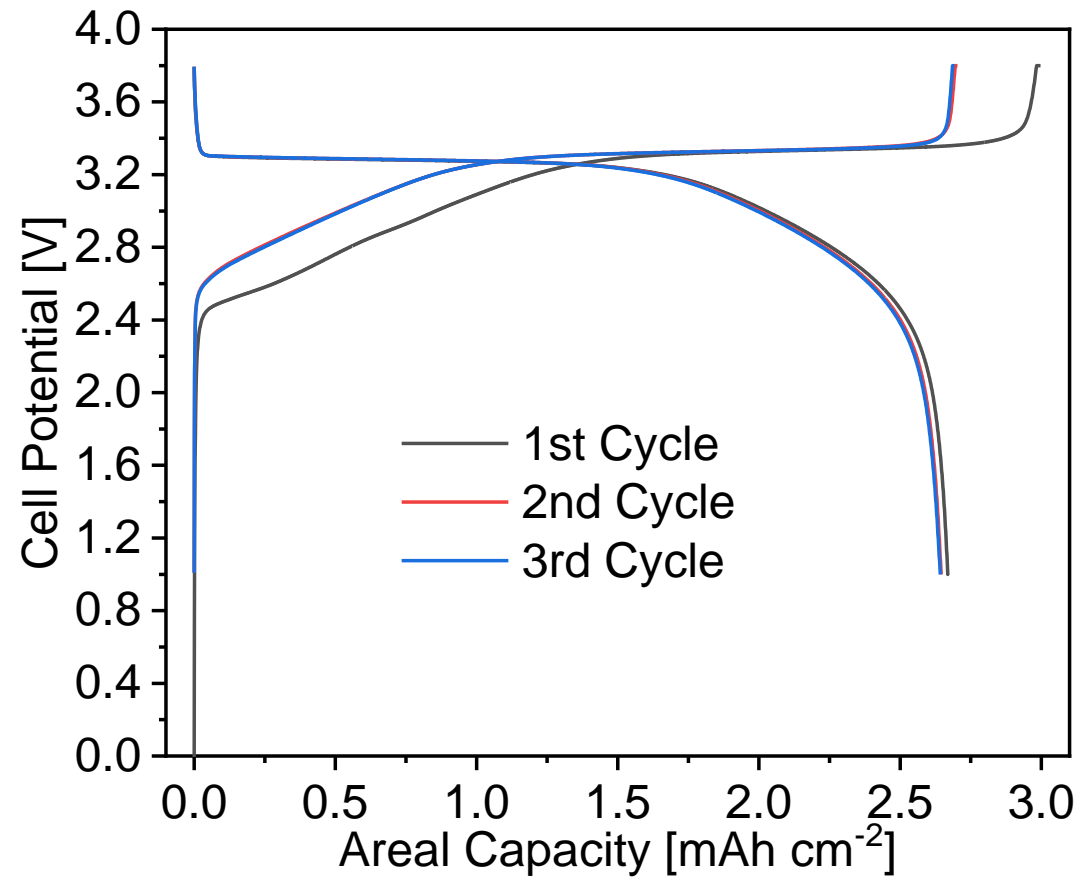
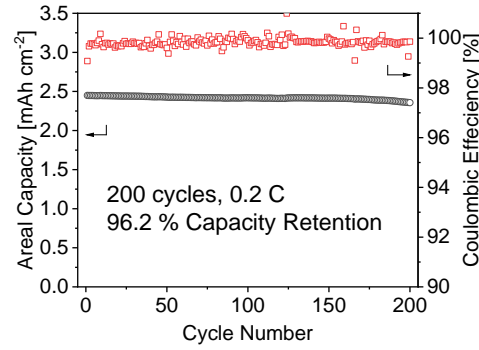
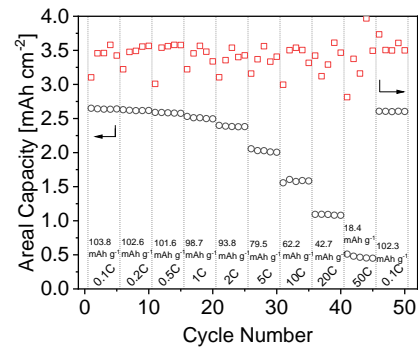
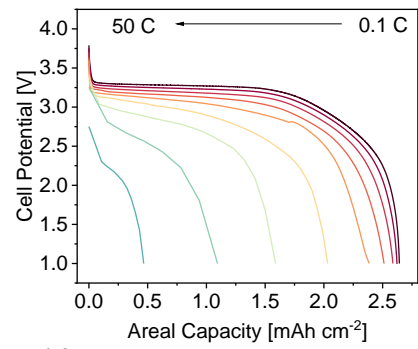
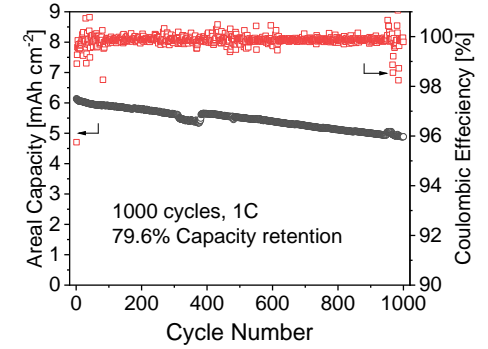
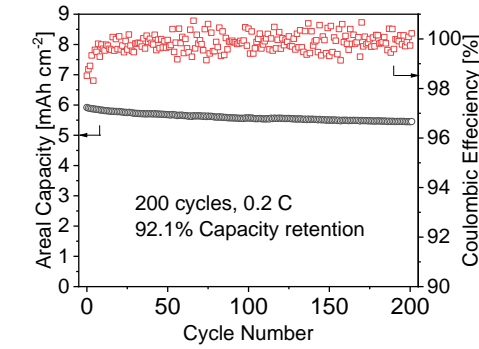
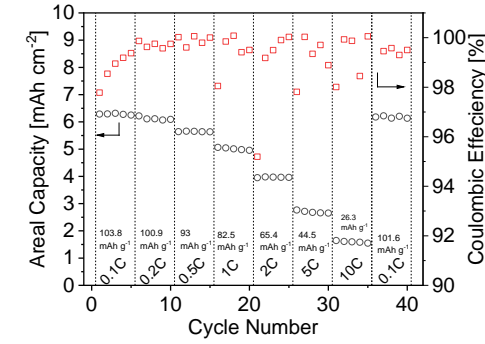
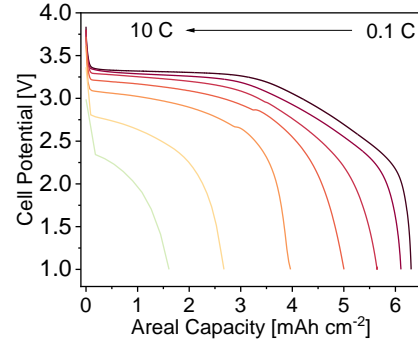


Figure S30 First three cycles of co-ESP NVPC/CNTF full cells with 25.4 mg cm⁻² areal loading

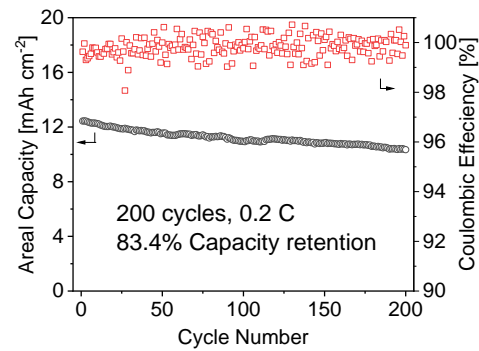
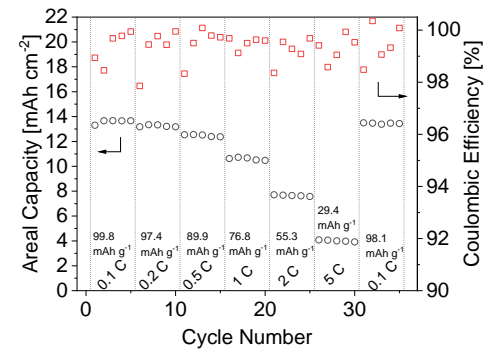
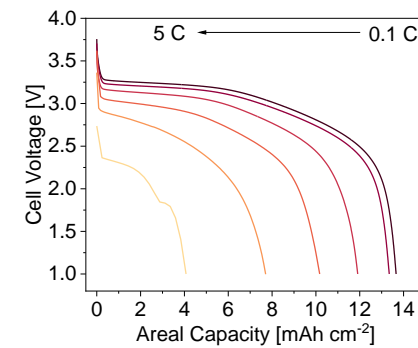
25.4 mg cm⁻²



60.7 mg cm⁻²



136.9 mg cm⁻²



296 mg cm⁻²

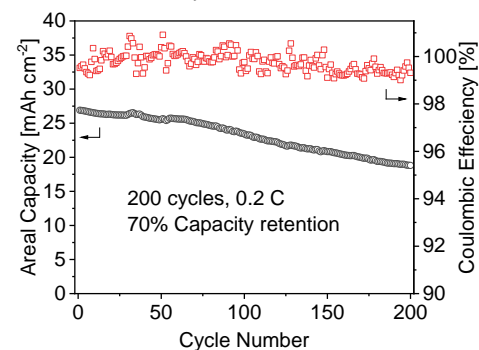
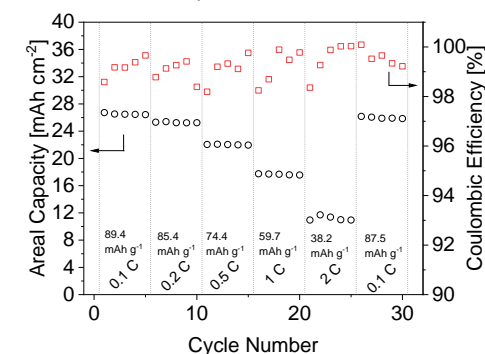
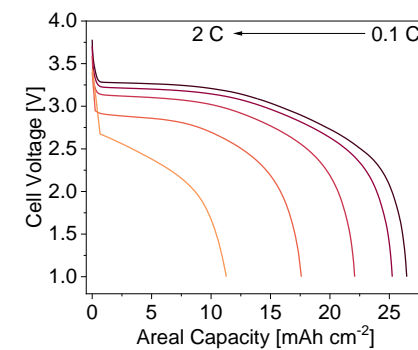


Figure S31 Detailed electrochemical data of full cells made of co-ESP NVPC/CNTF cathodes and HC/CNTF anodes of different areal loading

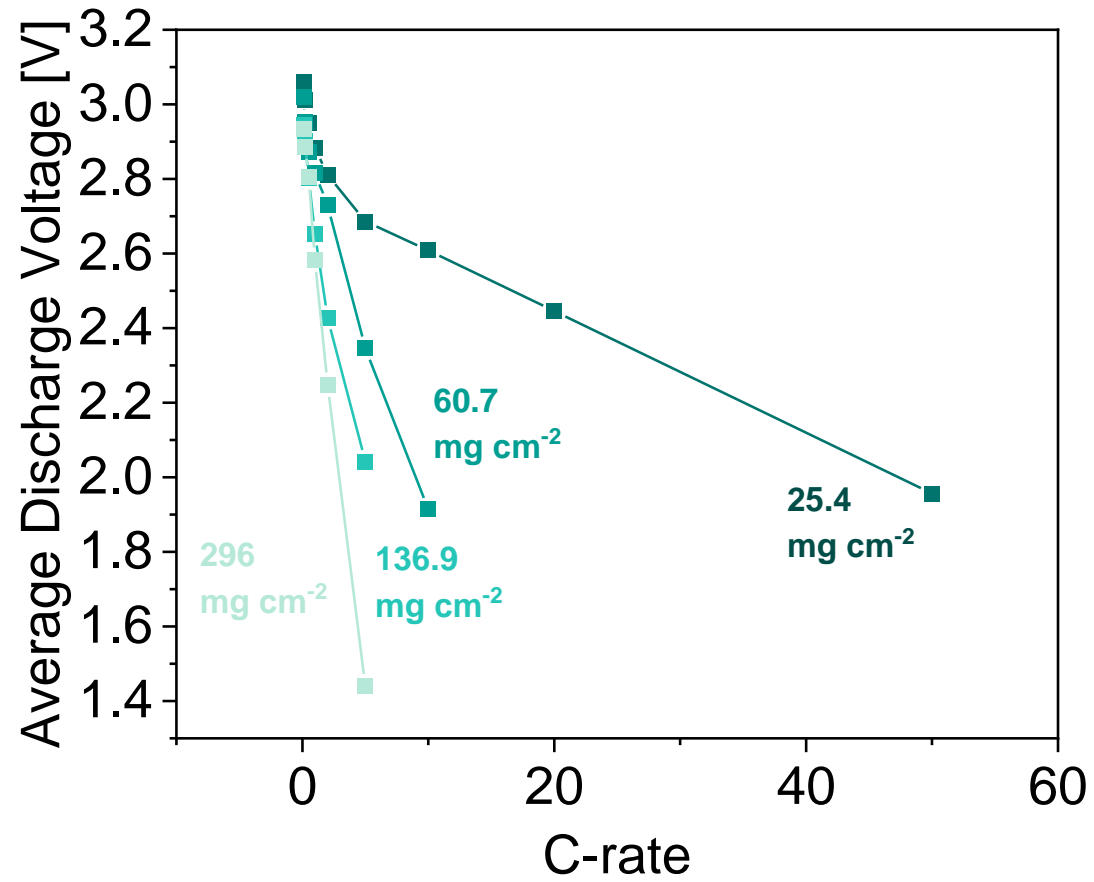


Figure S32 Average discharge voltage of co-ESP full-cells of different areal loading and C-rate

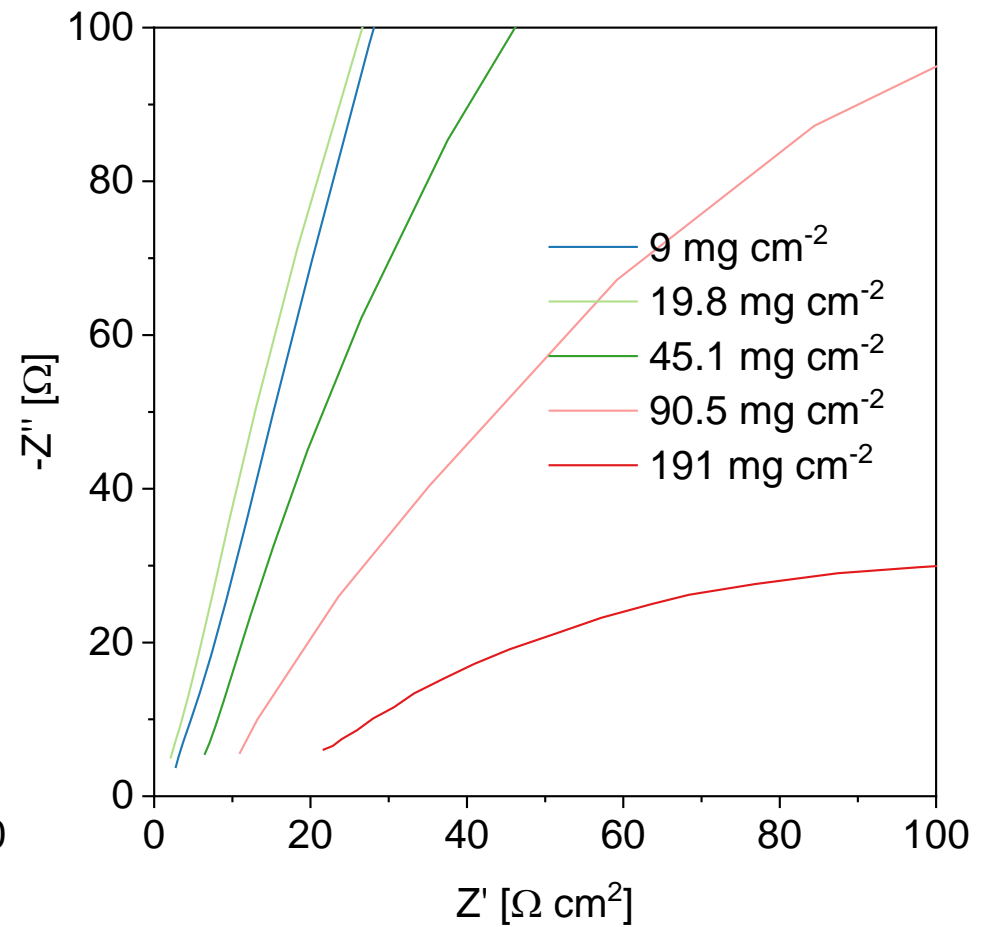
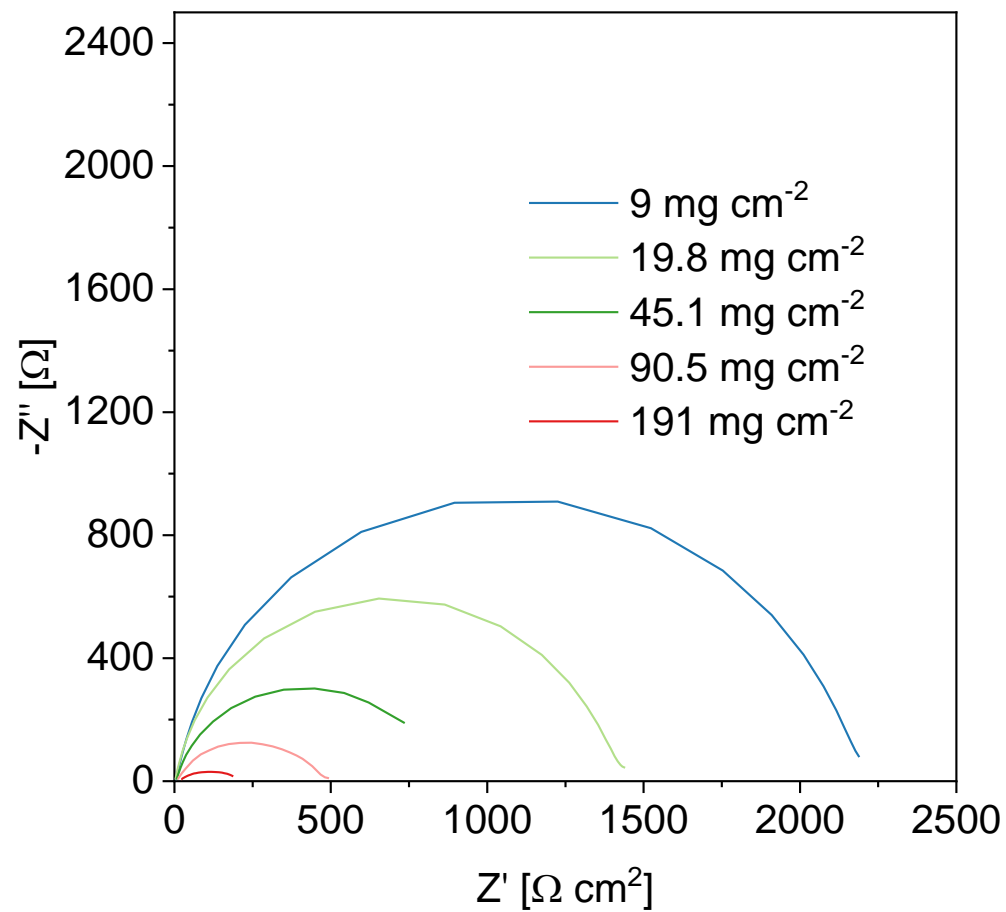


Figure S33 EIS of full cells made of co-ESP NVPC/CNTF cathodes and HC/CNTF anodes, of different cathode loading

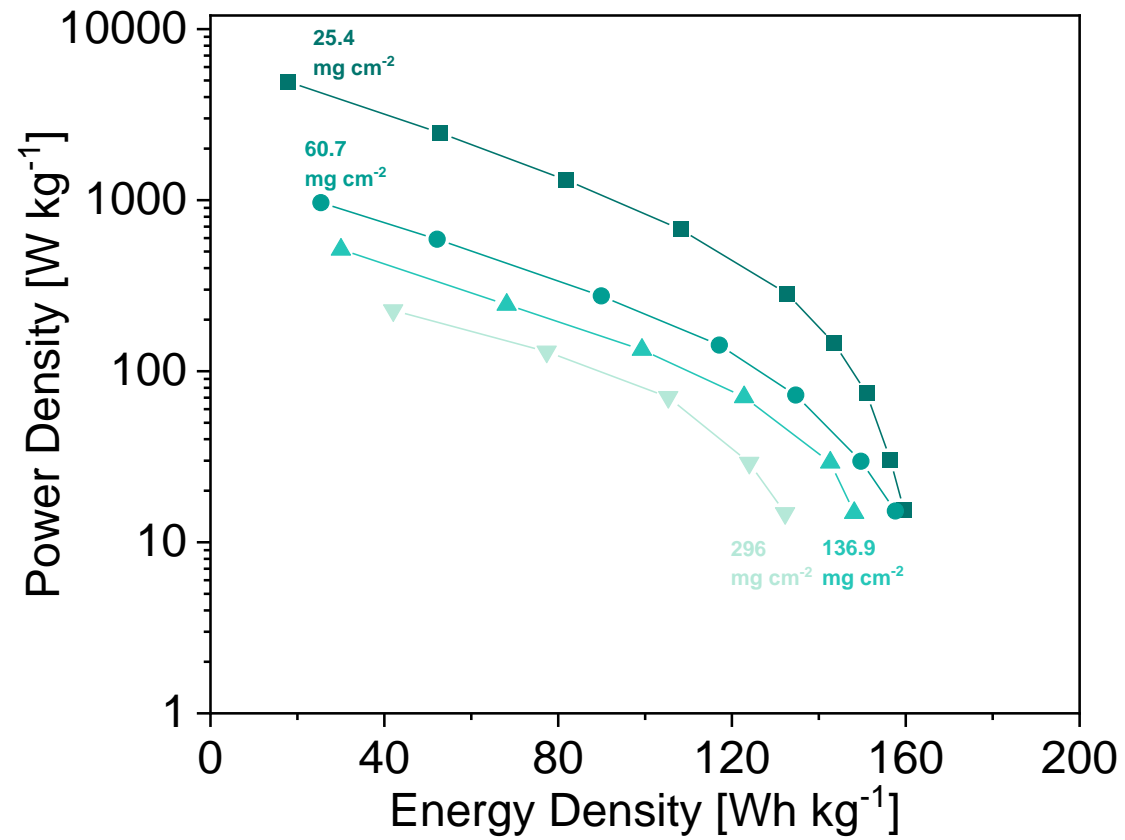


Figure S34 Gravimetric energy/power density of co-ESP full cells considering weight of electrolyte and separator

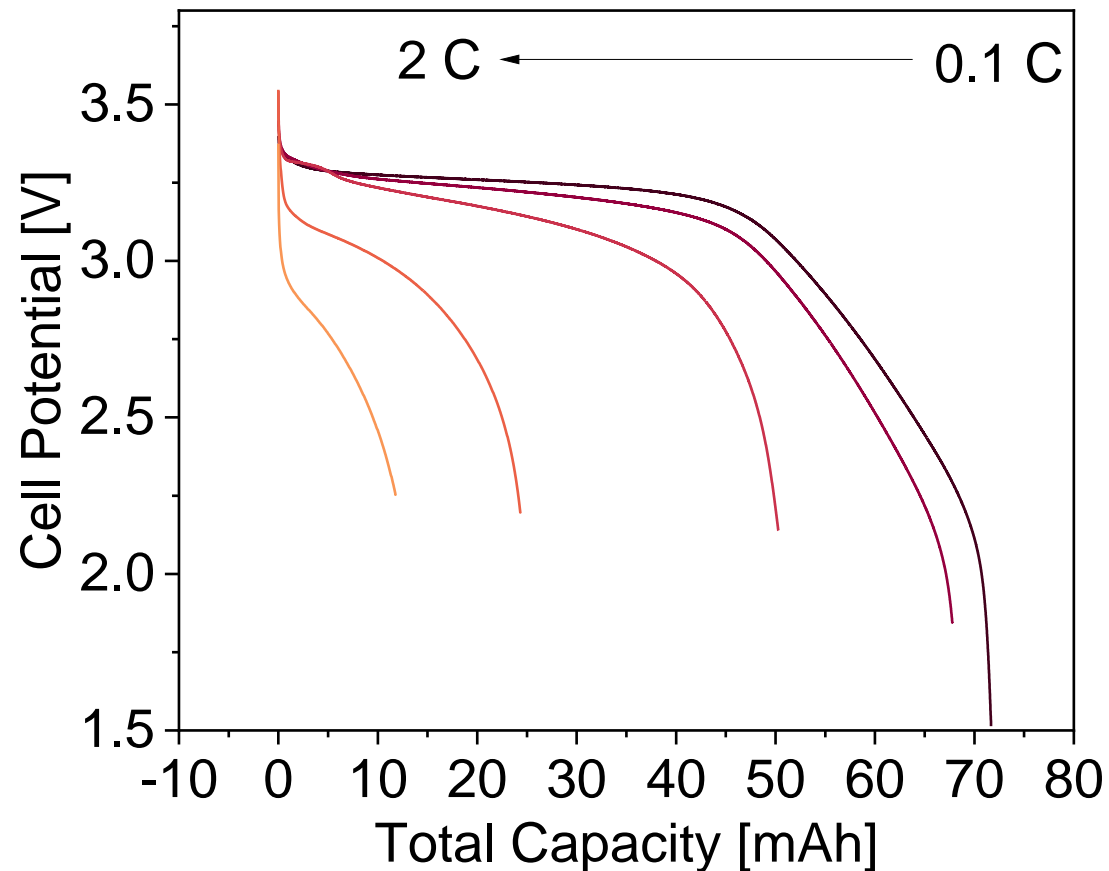
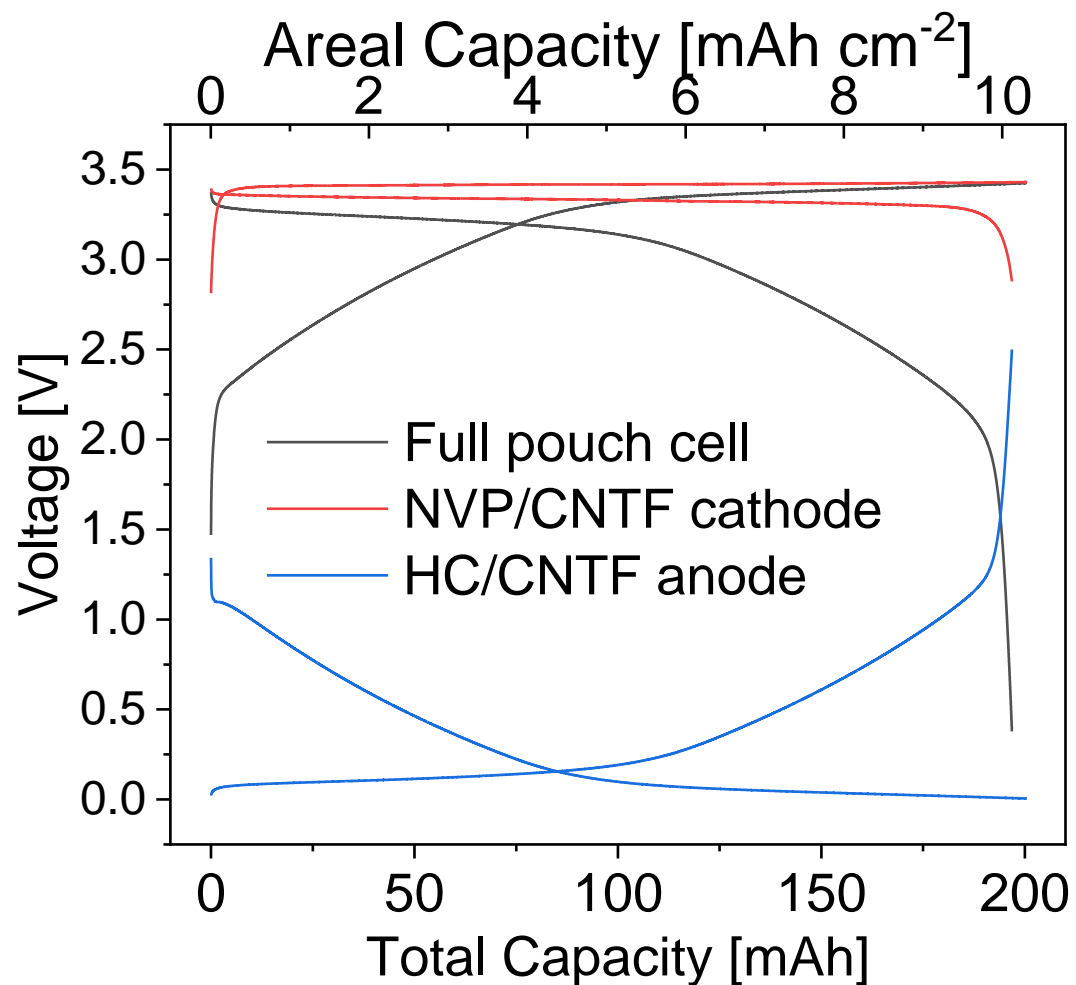


Figure S35 Left: Voltage profiles of a single-layer, 200 mAh pouch cell with 100 mg cm⁻² areal loading, 0.2 C, with a three-electrodes set-up; **Right:** voltage profiles of a 70 mAh pouch cell at different rates. CC-CV cycles. The discharge stopped when the anode's voltage reach 2.5V, or the cathode's voltage reach 2.5V, whichever happened first.

Supplementary Appendix 2: Tables

Table S1 Weight of different components for electrospinning and electrospaying, for electrodes with different active content, per 1000 mg NVP cathode

Active content	Electrospaying recipe			Electrospinning recipe		
	NVPC/mg	PEO/mg	DMF/mL	PAN/mg	CNT/mg	DMF/mL
90 wt%	10 ³	200	1	200	40	4
95 wt%	10 ³	200	1	100	20	2
97.5 wt%	10 ³	200	1	50	10	1
98 wt%	10 ³	200	1	40	8	0.8
99 wt%	10 ³	200	1	20	4	0.4

Table S2 Microstructural parameters extracted from micron and nano-XCT

	Synchrotron Micro-XCT uncompressed ¹	Synchrotron Micro-XCT compressed	Nano-XCT uncompressed	Calculated compressed electrode parameters ²
Total Porosity [vol%]	90	49.3	93.1	55.8
Porosity inside particles [vol%]	N/A	N/A	4.2	28.7
Porosity outside particles [vol%]	90	49.3	88.9	27.1
NVPC volume fraction [vol%]	10	50.7	6.5	41.6
CNTF volume fraction [vol%]	N/A	N/A	0.4	2.6
Pore through-plane tortuosity	1.15	2.00	1.33	2.00
Pore in-plane tortuosity (average x/y direction)	1.09	1.68	1.12	1.68

1. The voxel size of micron-CT was 350 nm, nano-CT 47 nm

2. Because of the large field of view of micro-CT, the following parameters were acquired from micro-CT results: porosity outside particles, NVPC volume fraction, through-plane and in-plane tortuosities. Micro-CT was unable to resolve the CNTF fibres and the intra-particle pores. Therefore, the CNTF volume fraction, porosity inside particles were acquired from nano-CT results.

Table S3 co-ESP composition 97.5 wt% NVP/CNF fabric electrode on a 300 cm² substrate

Aimed areal loading [mg cm ⁻²]	Electrospraying recipe			Electrospinning recipe		
	NVP/mg	PEO/mg	DMF/mL	PAN/mg	CNT/mg	DMF/mL
5	1.5×10 ³	300	1.5	75	15	1.5
20	6×10 ³	1.2×10 ³	6	300	60	6
100	3×10 ⁴	6×10 ³	30	1.5×10 ³	300	30

Table S4 Performance comparison with published sodium-ion half batteries work

Electrode fabrication method	Cathode composition ¹	Max half cell areal loading/capacity ³ (areal loading: rate, areal capacity) ²	Rate Capacity and retention (discharge rate, specific capacity in mAh g ⁻¹ , capacity retention) ³	Half cell cycling (number of cycles, rate, capacity retention)	Max areal Energy Density (mWh cm ⁻²)/Power Density (mW cm ⁻²) ⁴	Max gravimetric energy density (Wh kg ⁻¹)/power density (W kg ⁻¹) ⁴	Ref
Co-ESP	97.5% Commercial NVPC/CNTF	49.6 mg cm ⁻² : 0.1C, 5.2 mAh cm ⁻² ; 10C, 1.9 mAh cm ⁻²	0.1C, 106.7, 91.2%; 10C, 49.1, 42%	200 cycles, 0.2C, 93.1%	20.5/145.4	336.4/2390.7	This work
		4.3 mg cm ⁻² : 0.1C, 0.48 mAh cm ⁻² ; 200C, 0.18 mAh cm ⁻²	0.1C, 111.6, 95.4%; 200C, 41.9, 35.8%	5000 cycles, 50C, 84.5%	1.59/183.4	362.2/41805	
Slurry-casting	79.5% HNVP/CB/PVDF/Al foil	48.9 mg cm ⁻² : 0.01C, 3.8 mAh cm ⁻² ; 0.5C, 1.1 mAh cm ⁻²	0.05C, 77, 70.1%; 0.5C, 23, 20.9%	48.9 mg cm ⁻² no cycling data	13.1/7.52	213.1/122.3	Ref 61
Phase inversion	76% NVP/carbon	30 mg cm ⁻² : 0.1C, 2.8 mAh cm ⁻² ; 2C, 1.4 mAh cm ⁻²	0.1C, 91.7, 78.4%; 2C, 46, 39.3%	30 mg cm ⁻² no cycling data	9.15/8.46	231.7/440.8	Ref 7
Spray-drying#	66.2% NVP/CB/PVDF/Al foil	10 mg cm ⁻² : 0.2C, 1.2 mAh cm ⁻² ; 10C, 0.27 mAh cm ⁻²	0.2C, 120, 102.5%; 10C, 29, 24.8%	100 cycles, 1C, 100%	4.02/3.2	266.1/1725.8	Ref 4
Slurry-casting	57.6% NVP@C@CNT/CB/PVDF/Al foil	10 mg cm ⁻² : 0.5C, 1.2 mAh cm ⁻² ; 30C, 0.36 mAh cm ⁻²	0.5C, 117, 100%; 30C, 36, 30.8%	450 cycles, 15C, 95.2%	3.98/80.4	229.1/4631	Ref 5
Hydrothermal	43% NCO/Ni foam	10 mg cm ⁻² : 0.33C, 1.66 mAh cm ⁻² ; 2.1C, 1 mAh cm ⁻²	0.33C, 166.3, 98.5%; 2.1C, 100.5, 60.4%	100 cycles, 1C, 100%	4.42/5.67	190.2/243.8	Ref 6
Sol-gel	51.9% NVP/CNF/C65/PVDF/Al foil	8.5 mg cm ⁻² : 0.1C, 0.89 mAh cm ⁻² ; 2C, 0.84 mAh cm ⁻²	0.1C, 105, 89.7%; 2C, 99.6, 85.1%	200 cycles, 2C, 100%	3.01/81.6	184.5/4992	Ref 66
Slurry-casting	56% NVPF/GO/CB/PVDF/Al foil	8 mg cm ⁻² : 0.4C, 0.98 mAh cm ⁻² ; 6.3C, 0.85 mAh cm ⁻²	0.4C, 123, 96.9%; 6.3C, 106, 83%	200 cycles, 3 C, 96%	3.64/21.8	254.8/1523.2	Ref 67
Slurry-casting	49.6% NVP/CNF/C	8 mg cm ⁻² : 0.1C, 0.82 mAh cm ⁻² ; 40C, 0.5 mAh cm ⁻²	0.1C, 103, 88%; 40C, 62, 53%	500 cycles, 1C, 95.9%	2.76/83.2	171.1/5158.4	Ref 68
Precipitation&	72.6% NVP/CNF/C	7.6 mg cm ⁻² : 0.05C, 0.87 mAh cm ⁻² ; 100C, 0.5 mAh cm ⁻²	0.05C, 114, 97.4%; 100C, 66, 56.4%	700 cycles, 1C, 89.7%	2.85/ NA	270/ NA	Ref 69

The reported capacity exceeded the theoretical value of the cathode material, the source did not specify the reason.

& The work did not give the voltage profile at higher C-rate.

1. Calculated from the highest areal loading reported in the publication that has rate and cycling data. Estimated 15 μm-thick aluminium current collector weight: 4 mg cm⁻², 10 μm-thick copper current collector: 9 mg cm⁻²

2. Showing the areal capacity from the lowest and highest cycling rate.

3. The specific capacity of the highest areal loading reported in the publication, capacity retention at different rate; NMC811's theoretical capacity is 200 mAh g⁻¹; LCO's theoretical capacity is 170 mAh g⁻¹.

4. The energy/power densities are re-calculated considering the weight and volume of all electrode components, including active material, current collector, binder, conductive additive, based on the data reported in the literature. The method of calculation is shown in Supplementary Appendix 4.

Table S5 Performance comparison with published lithium-ion half-cell work

Fabrication method	Cathode composition ¹	Max half cell areal loading/capacity ³ (areal loading: rate, areal capacity) ²	Rate Capacity and retention (discharge rate, specific capacity in mAh g ⁻¹ , capacity retention) ³	Half cell cycling (number of cycles, rate, capacity retention)	Max areal Energy Density (mWh cm ⁻²)/Power Density (mW cm ⁻²) ⁴	Max gravimetric energy density (Wh kg ⁻¹)/power density (W kg ⁻¹) ⁴	Ref
Co-ESP	97.5% Commercial NVPC/CNTF	49.6 mg cm ⁻² : 0.1C, 5.2 mAh cm ⁻² ; 10C, 1.9 mAh cm ⁻²	0.1C, 106.7, 91.2%; 10C, 49.1, 42%	200 cycles, 0.2C, 93.1%	20.5/145.4	336.4/2390.7	This work
		4.3 mg cm ⁻² : 0.1C, 0.48 mAh cm ⁻² ; 200C, 0.18 mAh cm ⁻²	0.1C, 111.6, 95.4%; 200C, 41.9, 35.8%	5000 cycles, 50C, 84.5%	1.59/183.4	362.2/41805	
Mechanical pressing	79% LCO/KB/Carbon Cloth	71 mg cm ⁻² : 0.08C, 10 mAh cm ⁻² ; 0.8C, 8.7 mAh cm ⁻²	0.08C, 137, 85.6%; 1.6C, 97, 60.6%	40 cycles, 0.15C, 91%	37.7/50.4	419.9/709.9	ref
Slurry-casting&	80% LCO/cellulose/CNT	86 mg cm ⁻² : 0.1C, 12.1 mAh cm ⁻²	0.1 C, 141, 88.1%; no rate	20 cycles, 0.04C, 90%	46/5.23	427.7/48.6	ref
Impregnation	100% LCO	206 mg cm ⁻² : 0.05C, 24.7 mAh cm ⁻² ; 1C, 7.79 mAh cm ⁻²	0.05 C, 120, 75%; 1C, 37.8, 23.6%	27 cycles, 0.5C, 87%	93.9/95.6	455.6/464	ref
Slurry-casting	90.2% NMC811/ biopolymer/CNT/Al foil	47.7 mg cm ⁻² : 0.1C, 8.84 mAh cm ⁻² ; 1C, 3 mAh cm ⁻²	0.05C, 185, 92.5%; 1C, 62.9, 31.4%	50 cycles, 0.2C, 92.5%	29.9/28.9	625.8/604.3	ref
Slurry-casting	75% LFP/kb/CNF/PVDF	108 mg cm ⁻² : 0.05C, 17 mAh cm ⁻² ; 0.5C, 10 mAh cm ⁻²	0.05C, 157.4, 92.6%; 0.5C, 92.6, 54.5%	40 cycles, 0.2C, 94.3%	57.5/26.8	399/190	ref
Slurry-casting	71% LFP/CB/PVDF/Al foil	128 mg cm ⁻² : 0.025C, 19.8 mAh cm ⁻² ; 1C, 0.81 mAh cm ⁻²	0.025C, 155, 91.2%; 1C, 6.34, 3.7%	150 cycles, 0.1C, 73%	65.3/56	358.1/310.6	ref
Slurry-casting&	95.7% NMC811/CNT/Al foil	99 mg cm ⁻² : 0.05C, 17.8 mAh cm ⁻² ; 0.25C, 7.2 mAh cm ⁻²	0.05C, 180, 90%; 0.25C, 72.7, 36.4%	10 cycles, 0.1C, 96%	65.9/ NA	631.2/ NA	ref
Slurry-casting&	80% LFP/CNT/EVA	49 mg cm ⁻² : 0.2C, 7.5 mAh cm ⁻² ; 2C, 3 mAh cm ⁻²	0.2C, 153.1, 90%; 2C, 61.2, 36%	N/A	24.4/NA	416.3/NA	ref
Slurry-casting	67.3% LFP/CB/PVDF	70 mg cm ⁻² : 0.05C, 10.9 mAh cm ⁻² ; 1C, 1.5 mAh cm ⁻²	0.05C, 155.7, 91.6%; 1C, 21.4, 12.6%	200 cycles, 0.1C, 70%	36/16.4	346.1/157.7	ref
Extrusion	93.9 % LFP/carbon/Al foil	90 mg cm ⁻² : 1/24C, 12.8 mAh cm ⁻² ; 1/12C, 11.1 mAh cm ⁻²	1/24C, 142.2, 83.6%; 1/12C, 123.3, 72.5%	7 cycles, 1/12C, 86.6%	42.2/4.2	440.3/43.8	ref
Hot-pressing&	76.5% NMC712/CNT/PVDF/Al foil	70 mg cm ⁻² : 0.1C, 13.2 mAh cm ⁻² ; 0.5C, 6.8 mAh cm ⁻²	0.1C, 188.6, 94.3%; 0.5C, 97.1, 48.6%	30 cycles, 0.1C, 96%	48.8/NA	533.3/NA	ref

& The work did not give the voltage profile at higher C-rate.

1. Calculated from the highest areal loading reported in the publication that has rate and cycling data. Estimated 15 μm-thick aluminium current collector weight: 4 mg cm⁻², 10 μm-thick copper current collector: 9 mg cm⁻²

2. Showing the areal capacity from the lowest and highest cycling rate.

3. The specific capacity of the highest areal loading reported in the publication, capacity retention at different rate; NMC811's theoretical capacity is 200 mAh g⁻¹; LCO's theoretical capacity is 170 mAh g⁻¹.

4. The energy/power densities are re-calculated considering the weight and volume of all electrode components, including active material, current collector, binder, conductive additive, based on the data reported in the literature. The method of calculation is shown in Supplementary Appendix 4.

Table S6 Fabrication composition of co-ESP hard carbon

Aimed areal loading [mg cm ⁻²]	Electrospraying recipe			Electrospinning recipe		
	NVP/mg	PEO/mg	DMF/mL	PAN/mg	CNT/mg	DMF/mL
5	1.5×10 ³	600	3	160	32	3.2
10	3×10 ³	1.2×10 ³	6	320	64	6.4
25	7.5×10 ³	3×10 ³	15	800	160	16
40	1.2×10 ⁴	4.8×10 ³	24	1.28×10 ³	256	25.6

Table S7 Specification of sodium-ion battery coin cell using co-ESP electrodes, 25.4 mg cm⁻² cathode loading

	Separator	Cathode	Anode
Active materials used	Polypropylene	NVPC/CNTF	Hard carbon/CNTF
Active materials loading [wt%]	N/A	97.5 %	98 %
Conductive additive [wt%]		2.5%	2 %
Binder [wt%]			
Current collector [wt%]			
Areal loading [mg cm⁻²]		25.4	3.9
Compressed thickness [μm]	25	136.1	92.1
Area [cm²]	2.3	0.78	1.77
Total Weight [mg]	3	20.3	7
Electrolyte weight [mg]¹	11.6		
Energy density gravimetric [Wh kg⁻¹]²	156.4	Cell areal capacity 0.2 C [mAh cm⁻²]	2.63

1. The electrolyte weight is calculated by: $W_{electrolyte} = V_{cell} \varphi \rho_{electrolyte}$, $V_{electrode}$ is the volume of the electrodes and separator, φ is the porosity of the electrodes and separator, $\rho_{electrolyte}$ is the density of the electrolyte.
2. Including the weight of electrode components, separator, and electrolyte

Table S8 Specification of sodium-ion battery coin cell using co-ESP electrodes, 296 mg cm⁻² cathode loading

	Separator	Cathode	Anode
Active materials used	Polypropylene	NVPC/CNTF	Hard carbon/CNTF
Active materials loading [wt%]	N/A	97.5 %	98 %
Conductive additive [wt%]		2.5%	2 %
Binder [wt%]			
Current collector [wt%]			
Areal loading [mg cm⁻²]		296	46
Compressed thickness [μm]	25	1586	1086
Area [cm²]	2.3	0.78	1.77
Total Weight [mg]	3	236.8	83
Electrolyte weight [mg]¹	135		
Energy density gravimetric [Wh kg⁻¹]²	124	Cell areal capacity 0.2 C [mAh cm⁻²]	26.4

1. The electrolyte weight is calculated by: $W_{electrolyte} = V_{cell}\phi\rho_{electrolyte}$, $V_{electrode}$ is the volume of the electrodes and separator, ϕ is the porosity of the electrodes and separator, $\rho_{electrolyte}$ is the density of the electrolyte.
2. Including the weight of electrode components, separator, and electrolyte

Table S9 Specification of sodium-ion battery coin cell using conventional electrodes

	Separator	Cathode	Anode
Active materials used	Polypropylene	NVPC	Hard carbon
Active materials loading [wt%]	N/A	69.8 %	29.3 %
Conductive additive [wt%]		3.1 %	0 %
Binder [wt%]		4.6 %	3.3 %
Current collector [wt%]¹		22.5 %	67.4 %
Areal loading [mg cm⁻²]		16	3.9
Thickness [μm]	25	110	62
Area [cm²]	2.3	1.1	1.9
Weight [mg]	3	25.2	25.3
Electrolyte weight [mg]²	10.1		
Energy density gravimetric [Wh kg⁻¹]³	89.5	Cell areal capacity 0.2 C [mAh cm⁻²]	1.7

1. Estimated 15 μm-thick aluminium current collector weight: 4 mg cm⁻², 10 μm-thick copper current collector: 9 mg cm⁻².
2. The electrolyte weight is calculated by: $W_{electrolyte} = V_{cell} \phi \rho_{electrolyte}$, $V_{electrode}$ is the volume of the electrodes and separator, ϕ is the porosity of the electrodes and separator, $\rho_{electrolyte}$ is the density of the electrolyte, 1.26 g mL⁻¹.
3. Including the weight of electrode components, separator, and electrolyte

Table S10 Performance comparison with published sodium-ion full batteries work

Fabrication method	Cathode composition ¹	Max cathode areal loading/capacity (areal loading: rate, areal capacity) ²	Rate Capacity and retention (discharge rate, specific capacity in mAh g ⁻¹ , capacity retention) ³	Anode composition ¹	Full cell cycling (number of cycles, rate, capacity retention)	Max areal Energy Density (Wh cm ⁻²)/Power Density (W cm ⁻²) ⁴	Max gravimetric Energy Density (Wh kg ⁻¹)/Power Density (W kg ⁻¹) ⁴	Ref
Co-ESP	97.5% Commercial NVP/CNT/CNF, no binder, no current collector	296 mg cm ⁻² : 0.1C, 26.5 mAh cm ⁻² ; 1C, 11 mAh cm ⁻²	0.1C, 89.4, 76.4%; 2C, 46.5, 39.7%	98% Hard carbon-CNF/CNT, no binder, no current collector	200 cycles, 0.2C, 84.7%	77.7/133.1	191.9/328.8	This work
		25.4 mg cm ⁻² : 0.1C, 2.64 mAh cm ⁻² ; 50C, 0.47 mAh cm ⁻²	0.1C, 103.8, 88.7%; 50C, 42.7, 36.5%		200 cycles, 0.2C, 96.2%	8.05/248.4	231.6/7152.6	
Phase inversion	76% NVP/carbon, no binder, no current collector	7 mg cm ⁻² : 0.1C, 0.7 mAh cm ⁻² ; 2C, 0.6 mAh cm ⁻²	0.1C, 102, 87.2%; 2C, 89, 76.1%	Hard carbon, composition un specified	100 cycles, 1C, 99%	2.14/3.71	147.2/254.1	Ref 7
Sol-gel	51.9% NVP/CNF/C65/PVDF/Al foil	8.5 mg cm ⁻² : 0.1C, 0.85 mAh cm ⁻² ; 2C, 0.76 mAh cm ⁻²	0.1C, 99.7, 85.2%; 2C, 90, 76.9%	51.9% NVP/CNF/C65/PVDF/Al foil	3000 cycles, 2C, 60.1%	1.47/195.5	45/5968.5	Ref 66
Precipitation	72.6% NVP/CNF/C, no binder, no current collector	7.6 mg cm ⁻² : 0.05C, 0.84 mAh cm ⁻² ; 100C, 0.41 mAh cm ⁻²	0.05C, 111, 94.7%; 100C, 54.5, 46.6%	76.5% NTP/CNF/C, no binder, current collector	1000 cycles, 1C, 91% 4000 cycles, 20C, 74.5%	1/72.2	49.3/3538.7	Ref 69
Slurry-casting	56% NVPF/GO/CB/PVDF/Al foil	8 mg cm ⁻² : 0.78C, 0.88 mAh cm ⁻² ; 6.3C, 0.74 mAh cm ⁻²	0.78C, 110, 85.9%; 6.3C, 92.5, 72.3%	18.7% SnP/GO/CB/PA/Al foil	200 cycles, 0.78C, 62%	2.13/18.4	109.5/1840	Ref 67
Slurry-casting	25.6% NVP@C@CNT/CB/PVDF/Al foil	1.5 mg cm ⁻² : 0.05C, 0.77 mAh cm ⁻² ; 25C, 0.45 mAh cm ⁻²	0.05C, 102, 87.2%; 25C, 60, 51.2%	25.7% mesocarbon/CB/CMC-SBR/Al foil	5000 cycles, 5C, 72.7%	0.37/74.2	31.3/6366	Ref 5
Slurry-casting	31.5% HNVP/CB/PVDF/Al foil	2 mg cm ⁻² : 0.5C, 0.18 mAh cm ⁻² ; 20C, 0.12 mAh cm ⁻²	0.5C, 90.8, 82.7%; 20C, 61.8, 56.3%	31.5% NTP/CB/PVDF/Al foil	700 cycles, 2C, 88.8%	0.23/5.27	17.9/414.9	Ref 61

1. Calculated from the highest areal loading reported in the publication that has rate and cycling data. Estimated 15 μm-thick aluminium current collector weight: 4 mg cm⁻², 10 μm-thick copper current collector: 9 mg cm⁻²
2. Showing the areal capacity from the lowest and highest cycling rate.
3. The specific capacity of the highest areal loading reported in the publication, capacity retention at different rate; NMC811's theoretical capacity is 200 mAh g⁻¹; LCO's theoretical capacity is 170 mAh g⁻¹.
4. The energy/power densities are re-calculated considering the weight and volume of all electrode components, including active material, current collector, binder, conductive additive, based on the data reported in the literature. The method of calculation is shown in Supplementary Appendix 4.

Table S11 Performance comparison with published lithium-ion full batteries work

Fabrication method	Cathode composition ¹	Max cathode areal loading/capacity (areal loading: rate, areal capacity) ²	Rate Capacity and retention (discharge rate, specific capacity in mAh g ⁻¹ , capacity retention) ³	Anode composition ¹	Full cell cycling (number of cycles, rate, capacity retention)	Max areal Energy Density (Wh cm ⁻²)/Power Density (W cm ⁻²) ⁴	Max gravimetric Energy Density (Wh kg ⁻¹)/Power Density (W kg ⁻¹) ⁴	Ref
Co-ESP	97.5% Commercial NVPC/CNTF, no binder, no current collector	296 mg cm ⁻² : 0.1C, 26.5 mAh cm ⁻² ; 11 mAh cm ⁻² , 2C	0.1C, 89.4, 76.4%; 2C, 46.5, 39.7%	98% Hard carbon/CNTF, no binder, no current collector	200 cycles, 0.2C, 84.7%	77.7/133.1	191.9/328.8	This work
		25.4 mg cm ⁻² : 0.1C, 2.64 mAh cm ⁻² ; 50C, 0.47 mAh cm ⁻²	0.1C, 103.8, 88.7%; 50C, 42.7, 36.5%		200 cycles, 0.2C, 96.2%	8.05/248.4	231.6/7152.6	
Slurry-casting	80% LCO/cellulose/CNT, no current collector	30 mg cm ⁻² : 0.1C, 4.6 mAh cm ⁻² ; 1C, 2.8 mAh cm ⁻²	0.1C, 152, 89.4%; 1C, 93.3, 54.9%	80% LTO/cellulose/CNT	N/A	10.6/10.5	141.3/140	ref
Slurry-casting	94.5% NMC811/biopolymer/CNT/Al foil	54.4 mg cm ⁻² : 0.1C, 9.24 mAh cm ⁻² No rate data	0.1C, 169.9, 85% No rate data	Graphite/biopolymer/CNT/Cu foil, unknown active content, max 76.9%	40 cycles, 0.1C, 92.8%	33.3/3.6	367.9/66.2	ref
Slurry-casting	96.4% NMC811/CNT/Al foil	156 mg cm ⁻² : 1/15C, 29 mAh cm ⁻² ; 1C, 15 mAh cm ⁻²	0.05C, 185.9, 93%; 1C, 96.2, 48.1%	52.1% Si/CNT/Cu foil	47 cycles, 1/15C, 83%	98.3/105.8	569.3/586.6	ref
Impregnation	62.2% LFP/Super P/PVDF/CNT-polyester current collector	168 mg cm ⁻² : 1/15C, 26 mAh cm ⁻² ; No rate data	1/15C, 155, 91.2% No rate data	61.1% LTO/Super P/PVDF/CNT-polyester current collector	33 cycles, 0.1C, 86%	46.8/3.4	85.7/6.2	ref
Extrusion	93.9 % LFP/carbon/Al foil	90 mg cm ⁻² : 1/24C, 13.5 mAh cm ⁻² ; 1/12C, 11.1 mAh cm ⁻²	1/24C, 150, 88.2%; 1/12C, 123, 72.4%	92.2% LTO/carbon/Cu foil	100 cycles, 1/12C, 67%	23.6/14.2	121.9/73.3	ref
Slurry-casting	80% LFP/carbon/EVA, no current collector	29.4 mg cm ⁻² : 0.1C, 4.6 mAh cm ⁻² ; 1C, 3.5 mAh cm ⁻²	0.1C, 156.5, 92%; 1C, 120, 70.5%	80% LTO/carbon/EVA	60 cycles, 0.5C, 76.9%	8/8.5	108.8/115.6	ref
Slurry-casting	65% LFP/CB/PVDF, no current collector	36 mg cm ⁻² : 0.05C, 5.5 mAh cm ⁻² ; 0.1C, 5 mAh cm ⁻²	0.05C, 152.8, 89.9%; 0.1C, 138.9, 81.7%	59% LTO/CB/PVDF	500 cycles, 0.1C, 87%	9.9/1.1	85.3/9.5	ref

1. Calculated from the highest areal loading reported in the publication that has rate and cycling data. Estimated 15 μm-thick aluminium current collector weight: 4 mg cm⁻², 10 μm-thick copper current collector: 9 mg cm⁻²
2. Showing the areal capacity from the lowest and highest cycling rate.
3. The specific capacity of the highest areal loading reported in the publication, capacity retention at different rate; NMC811's theoretical capacity is 200 mAh g⁻¹; LCO's theoretical capacity is 170 mAh g⁻¹.
4. The energy/power densities are re-calculated considering the weight and volume of all electrode components, including active material, current collector, binder, conductive additive, based on the data reported in the literature. The method of calculation is shown in Supplementary Appendix 4.

Supplementary Appendix 3: Calculating Energy Density

- The gravimetric energy densities were calculated by: $E_g = \bar{V}C_g c_{active}$. \bar{V} is the average voltage in the discharge process; C_g is the gravimetric specific capacity, considering only the weight of active materials; c_{active} is the active content, calculated by :

$$c_{active} = \frac{m_{active}}{m_{active} + m_{binder} + m_{current\ collector} + m_{conductive\ additive}}$$
 Estimated 15 μm -thick aluminium current collector weight: 4 mg cm^{-2} , 10 μm -thick copper current collector: 9 mg cm^{-2}
- The gravimetric power densities were calculated by: $P_g = I_g \bar{V} c_{active}$. I_g is the discharge gravimetric current density, calculated by : $I_g = \frac{I}{m_{active}}$. I is the discharge current.
- The areal energy densities were calculated by: $E_a = \bar{V}C_a$. C_a is the areal capacity.
- The areal power densities were calculated by: $E_a = \bar{V}I_a$. I_a is the areal current, calculated by $I_a = \frac{I}{A_{electrode}}$, $A_{electrode}$ is the geometric area of the electrode.
- The energy densities in all referenced literatures in **Figure 4h, i, Figure 5e, f, Table S4, S5, S10, S11** were recalculated with the above formula, to make consistent comparisons.
- To calculate the gravimetric energy/power density considering the electrolyte and separator in **Figure S34**, we substitute the c_{active} in the equation with $c'_{active} = \frac{m_{active}}{m_{active} + m_{binder} + m_{current\ collector} + m_{conductive\ additive} + m_{electrolyte} + m_{separator}}$. $m_{separator}$ is 3.1 mg for a 2.5 cm^2 Celgard 2400 separator.
 $m_{electrolyte} = \rho_{electrolyte} v_{composite} P$, P is the porosity of the electrodes/separator composite, $v_{composite}$ is the volume of the composite, $\rho_{electrolyte}$ is the electrolyte's density, 1.26 g cm^{-3} .
- To calculate the gravimetric energy density of pouch cells, the $c_{active}^{pouch} = \frac{m_{active}}{m_{pouch}}$. The volumetric energy density of the pouch cells were calculated by:

$$E_g = \frac{\bar{V}C}{A_{pouch} L_{pouch}}$$
 A_{pouch} is the geometric area of the pouch cell, L_{pouch} is the thickness.